Title
Pseudosolid Electrolytes and their Application in Next-Generation Sodium-ion Storage Devices

Author
DeBlock, Ryan

Publication Date
2020

Peer reviewed|Thesis/dissertation

UNIVERSITY OF CALIFORNIA

Los Angeles

Pseudosolid Electrolytes and their Application in Next-Generation Sodium-ion Storage Devices

A dissertation submitted in partial satisfaction

of the requirements for the degree

Doctor of Philosophy in Materials Science and Engineering

by

Ryan Henry DeBlock

2020

ABSTRACT OF THE DISSERTATION

Pseudosolid Electrolytes and their Application in Next-Generation Sodium-ion Storage Devices

by

Ryan Henry DeBlock

Doctor of Philosophy in Materials Science and Engineering

University of California, Los Angeles, 2020

Professor Bruce Dunn, Chair

Sodium-ion batteries are quickly becoming a promising, earth-abundant alternative to lithium-ion technology. To address ongoing safety issues associated with both lithium- and sodium-ion batteries, we apply sol-gel processing to create nonflammable, pseudosolid electrolytes. An interconnected, porous silica scaffold encapsulates an ionic liquid creating an "ionogel" electrolyte with high liquid content. These electrolytes retain the conductivity the ionic liquid (~1 mS cm^{-1}), but are macroscopically solid. In Chapter 2, we demonstrate the synthesis of compliant, organically-modified ionogel electrolytes for sodium-ion batteries and demonstrate their use in energy storage devices. When tested with common electrode materials (such as activated carbon, sodium vanadium phosphate, sodium titanium phosphate) these ionogel electrolytes enable at least 100 cycles with minimal capacity fade and high Coulombic efficiency.

To enable the use of sodium metal as a high-capacity electrode, we modify the pseudosolid electrolyte synthesis to incorporate tetraglyme as a low vapor pressure alternative

to ionic liquid. In Chapter 3, we demonstrate that these pseudosolid electrolytes have both wide electrochemical stability windows (up to 4.5 V vs $Na|Na^+$) and ionic conductivity values near 1 mS cm^{-1}. We observe extremely low overpotentials (~50 mV) to sodium metal plating/stripping onto carbon-coated aluminum over hundreds of cycles. When paired with sodium vanadium fluorophosphate (NVOPF) cathode, devices with glyme electrolyte deliver theoretical capacity of 125 mAh g^{-1} at a rate of 0.5C and are among the most energy-dense solid-state, sodium-ion storage devices to date.

Typical battery electrodes are crystalline compounds with layered or tunnel structures which allow facile ion transport. In contrast, amorphous materials are explored seldomly and have widely varying properties due to their variable nature. In Chapter 4 we explore the synthesis amorphous vanadium dioxide (a–VO_2) and its capability as a sodium-ion storage material. Pristine a–VO_2 powder delivers nearly 300 mAh g^{-1} and, when grown on graphite foam (presented in Appendix A), sustains 160 mAh g^{-1} at an extremely fast rate of 60C.

The dissertation of Ryan Henry DeBlock is approved.

Yongjie Hu

Aaswath Raman

Yang Yang

Bruce Dunn, Committee Chair

University of California, Los Angeles

2020

To Sarah

“Do you have any idea how many lives we must have gone through before we even got the first idea that there is more to life than eating, or fighting, or power in the Flock? A thousand lives, Jon, ten thousand!”

~Richard Bach, Jonathan Livingston Seagull

Table of Contents

List of Figures

Figure 2.7. a. Nitrogen adsorption isotherm and b. the pore-size distribution for an ionogel with no m–PDMS (replaced with equimolar MTMS).

Figure 2.8. a. Electrochemical impedance spectroscopy as a function of temperature for the ionogel electrolyte b. Ionic conductivity–inverse temperature plot and extracted activation energy c. Linear sweep voltammetry to assess the electrochemical stability window of the ionogel electrolyte. Two separate samples were used for the forward and reverse scan.

Figure 2.9. a. Cyclic voltammetry (0.1 mV s^{-1}) for an NVP cathode against sodium metal demonstrates severe polarization for the ionogel electrolyte. A control test in 1M $NaPF_6$ diglyme is included as a comparison. Current is normalized to peak current for proper comparison. b. EIS spectrum for 3 cells: Na|IG|Na, NVP|IG|Na, and NVP|IG|NVP. Inset shows the low resistance of the NVP|IG|NVP cell (green) c. EIS spectra for the traditional half-cell, NVP|IG|Na, and the modified half-cell, NVP|IG|AC, immediately after and 72 hours after construction. Inset shows the low resistance of the NVP|IG|AC cell (blue).

Figure 2.10. XPS for a,c,e,g. the NVP|IG|Na sample and b,d,f,h. the NVP|IG|AC sample after 72 hours exposure to electrolyte. a,b. Survey scans, c,d. C 1s e,f. O 1s and g,h. F 1s scans.

Figure 2.11. XPS (N 1s, Na 1s, P 2p) spectra for a,c,e. the NVP|IG|Na cell and b,d,f. the NVP|IG|AC cell.

Figure 2.12. XPS (S 2p, V 2p, Si 2p) spectra for a,c,e. the NVP|IG|Na0 cell and b,d,f. the NVP|IG|AC cell.

Figure 2.13. Schematic representation of the a. NVP|IG|AC half-cell and b. the NVP|IG|NTP full-cell devices.

Figure 2.14. a. Galvanostatic charge/discharge curves for a rate of 0.25C and b. corresponding capacity and Coulombic efficiency for the NVP|IG|AC cell. c. Discharge capacity of the NVP|IG|AC cell as a function of C-rate.

Figure 2.15. a. Galvanostatic charge/discharge curves at a rate of 0.25C and b. the corresponding capacity and Coulombic efficiency for the NVP|IG|NTP full-cell device.

Figure 3.1. Comparison of the theoretical specific capacity and desodiation potential of various anode materials for sodium-ion batteries.

Figure 3.2. Plating/stripping data for symmetric lithium metal and sodium metal cells at a) 0.1 mA cm^{-2} b) 1 mA cm^{-2} and c) 5 mA cm^{-2}. The electrolyte for Li|Li cells is 1M $LiPF_6$ in ethylene carbonate:dimethyl carbonate (1:1, w:w). The electrolyte for Na|Na cells is 1M $NaPF_6$ in either ethylene carbonate:dimethyl carbonate (1:1, w:w) or ethylene carbonate:propylene carbonate:dimethyl carbonate (0.45:0.45:0.1, w:w).

Figure 3.3. a) Schematic representation of the plating/stripping process and b) the corresponding response of a constant-current experiment. Step 1: reversible surface reactions with the carbon coating on aluminum foil. Step 2: Nucleation of sodium metal. Step 3: initial growth of sodium metal. Step 4: steady-state growth of sodium metal. Step 5: current reversal and stripping of sodium metal. Step 6: steady-state stripping of sodium-metal. Step 7: stripping of remaining sodium metal and reactions with carbon. A capacity of 1 mAh was plated on each cycle at a current density of 1 mA cm^{-2}.

Figure 3.4. a) Selected cycles of plating and stripping experiments with carbon-coated aluminum working and sodium metal counter/reference electrodes at a current of 1 mA cm^{-2} for a capacity of 1 mAh cm^{-2} for a,c) 1:4 $NaBF_4$:G4 and b,d) 1:2 $NaBF_4$:G4. Coulombic efficiency and mid-voltage overpotential as a function of cycling for e) 1:4 $NaBF_4$:G4 and f) 1:2 $NaBF_4$:G4. All tests were one hour plating and one hour stripping with a 1V cutoff.

Figure 3.5. First cycle of galvanostatic discharge for NVOPF electrode in 1:4 $NaBF_4$:G4 electrolyte and standard 1M $NaPF_6$ G2 as comparison. The charge/discharge rate is 1C. Testing was performed in half-cell, two-electrode format with NVOPF working electrode and sodium metal counter/reference electrode.

Figure 3.6. Thermogravimetric analysis (TGA) of the glyme-based gel electrolyte. Heating rate: 10 °C min^{-1}.

Figure 3.7. a) Ionic conductivity as a function of temperature for the glyme-based gel electrolyte. The liquid electrolyte was included for comparison at room temperature. b) Electrochemical stability window tests for the pseudosolid electrolytes. This test was performed with a carbon-coated aluminum working electrode and a sodium metal counter/reference electrode at a sweep rate of 1 mV s^{-1}. Tests for measuring the transference number of the glyme-based pseudosolid electrolyte including the c) polarization step and d) impedance before/after polarization to extract resistance values.

Figure 3.8. Plating/stripping experiments for a cell with a carbon-coated aluminum working electrode, sodium metal counter/reference electrode, and the glyme-based gel electrolyte a) Increasing plating capacity from 0.5 mAh cm^{-2} to 5 mAh cm^{-2} at a current density of 0.5 mA cm^{-2}. b) Midcycle overpotential taken on the plating cycle as a function of current density with a plating capacity of 1 mAh cm^{-2}. c) Coulombic efficiency and d) midcycle overpotential for long-term cycling at a current density of 0.5 mAh cm^{-2}.

Figure 3.9. Galvanostatic sodium plating curves for various current densities. Carbon-coated aluminum working electrode, sodium metal counter/reference electrode, and glyme-based gel electrolyte.

Figure 3.10. Electrochemical impedance spectroscopy (EIS) taken after each plating cycle for a symmetrical sodium sandwiching the glyme-based gel electrolyte. a) The full data range and b) a reduced range show the decrease in cell resistance after the first cycle.

Figure 3.11. a) X-ray diffraction (XRD) b) thermogravimetric analysis (TGA) and c,d) scanning electron microscopy (SEM) images of the NVOPF@rGO cathode.

Figure 3.12. Electrochemical results for the NVOPF sodium-metal battery with glyme-based gel electrolyte. a) Charge/discharge curve at a rate of 0.5C b) Rate retention for C-rates: 0.2C, 0.25C, 0.33C, 0.5C, 1C, 2C, and 4C c) long-term cycling at a rate of 0.5C d) Ragone plot comparing this work to other full-cell, sodium-based devices.

Figure 4.10. Slow galvanostatic cycling (40 mA g^{-1}) of a–VO_2 with glyme-based gel electrolyte and sodium metal counter/reference electrode.

Figure A.1. Structural and morphology characterizations of c-VO_2 and a-VO_2. a) Plan view of c-VO_2. b) Plan view of a-VO_2. c) Cross-section of a-VO_2 on graphite foam. d) XRD of c-VO_2 shows that the material corresponds to VO_2 (B). The strong reflection at 26.6^o is from the graphite foam. The inset shows the TEM image with the fast Fourier transform (FFT) pattern. e) XRD of a-VO_2 shows only the peaks for the GF. The inset shows the TEM image of the thin plate with the FFT pattern.

Figure A.2. High-resolution XPS spectra of V *2p* for c-VO_2 and c-VO_2. a,b) pristine state of c-VO_2 (a) *c*-VO_2 (b). c,d) upon discharge to 2.5 V (D2.5 V) of c-VO_2 (c) c-VO_2 (d). e,f) upon discharge to 1.0 V (D1.0 V) of c-VO_2 (e) *c*-VO_2 (f).

Figure A.3. The charge storage properties for a-VO_2 in the 4.0 to 1.0 V (vs. Na/Na^+) regime as well as in specific voltage regions for positive electrode and negative electrodes. a) Initial first three charge/discharge profiles of the a-VO_2 electrode at 0.1C (40 mA g^{-1}). b) CV curves at various scan rates from 0.2 to 5 mV s^{-1}. c) The triangular charging and discharging over the entire 1 to 4 volt region at 60C and extend for multiple cycles. d) Capacitive (shaded area) and diffusion-controlled (cavity area) contribution to charge storage of a-VO_2 at 0.8 mV s^{-1}. e,f) Galvanostatic charge/discharge profiles at different rates from 0.5−60C of a-VO_2 electrode in cathodic (e) and anodic (f) windows, respectively. 1C is defined as 200 mA g^{-1} in specific cathodic/anodic window.

Figure A.4. Symmetric battery based on a-VO_2 with pseudocapacitive behavior. a) Schematics of two types of symmetric batteries based on bipolar electrode materials. For the top row, traditional phase transition based symmetric device configuration. The bipolar material with two obvious plateaus in the half-cell. The electrode can be assembled and cycled at both cathodic voltage plateau and anodic voltage plateau. For the bottom row, pseudocapacitance-enabled symmetric devices configuration. Bipolar material shows with wide-window capacitive behavior.

b) Galvanostatic charge/discharge profiles at different rates from 1−50C. c) High-rate long-term cycling stability of a-VO_2 based symmetric device at 50C. A rate of 1C corresponds to 100 mA g^{-1} in the symmetric cell, based on the mass of both the cathode and anode materials.

Figure A.5. Morphology and structural characterizations of c-VO_2 and a-VO_2. a,b) FESEM and TEM of GF supported c-VO_2 electrodes. c,d) FESEM and TEM of GF supported a-VO_2 electrodes. e) Crystal structure of monoclinic VO_2 (B) with two different types of square pyramidal sites at the intervals of the VO6 octahedra. f) Photograph showing the electrode is bent by a small force to demonstrate the flexibility and lightweight.

Figure A.6. Cross-section view of GF supported a-VO_2 electrodes at different magnification. The figures show a height of ~100 nm of the a-VO_2 nanosheet and the nanosheets anchor on both the outside and inner wall of the graphene foam.

Figure A.7. Galvanostatic charge/discharge performance of pure GF in the voltage window of 4.0 and 1.0 V vs Na/Na^+. The result shows that the capacity contribution from GF in the composites are neglectable.

Figure A.8. EDX spectra of c-VO_2 (a) and a-VO_2 (b) after discharge. The results give Na:V ratio of nearly 1.10:1 for c-VO_2 and 1.22:1 for a-VO_2 electrodes.

Figure A.9. *Ex situ* XRD patterns of a-VO_2 before and after charge/discharge cycles at 0.1C. The absence of any new peaks confirms the a-VO_2 retains its amorphous state after discharge in following cycles.

Figure A.10. Galvanostatic charge/discharge profile of c-VO_2 compared with a-VO_2 electrodes after 3 cycles activation at 0.1C. The *a*-VO_2 electrode delivers a specific discharge capacity of ~400 mAh g^{-1} at a slow rate of 0.1C (40 mA g^{-1}), whereas the c-VO_2 electrode shows a lower capacity of ~360 mAh g^{-1}. Notably, a-VO_2 leads to lower polarization (90 mV for the *a*-VO_2) and

a sloped galvanostatic profile, suggesting the capability of fast charge storage through pseudocapacitance. In contrast, the galvanostatic profile for c-VO_2 shows a higher overpotential of 680 mV during the charge and discharge process.

Figure A.11. Structural evolutions of of c-VO_2 during cycles. *Ex situ* XRD patterns of c-VO_2 collected over 50 cycles at different discharge–charge voltages. The current density is 0.1C. No phase change occurs but the peaks do shift as Na^+ insertion and de-insertion affect the lattice parameter.

Figure A.12. *Ex situ* HRTEM images of the c-VO_2 collected after discharge at 0.1C. Single crystalline feature reserved after cycle with slight lattice expansion.

Figure A.13. XPS survey scan for c-VO_2 and a-VO_2 at the desodiated state D4.0V-50th after argon plasma etching to remove the outer surface layer. Note the absence of Na peak in the a-VO_2.

Figure A.14. a) CV curves at various scan rates (10 to 50 mV s^{-1}) for a-VO_2. b,c) for c-VO_2 electrodes. d) Capacitive (shaded area) and diffusion-controlled (cavity area) contribution to charge storage of c-VO_2 at 0.8 mV s^{-1}.

Figure A.15. a) Relationship between logarithm anodic peak current (at ca. 2.0 V) and logarithm scan rate for a-VO_2 from 0.2 to 10 mV s^{-1}. b) The mass-normalized capacity as function of sweep rate for a-VO_2 and c-VO_2.

Figure A.16. Galvanostatic charge/discharge profiles of a-VO_2 electrode. Galvanostatic response at 20C for a-VO_2 for 500 cycles in a) the cathodic window and b) the anodic window.

Figure A.17. CV curves at various scan rate for a-VO_2 electrode at specific cathode/anode window. a,c) in cathodic and anodic windows, respectively. b,d) Capacitive (shaded area) and

diffusion-controlled (cavity area) contribution to charge storage of a-VO_2 electrode in cathodic and anodic windows, respectively.

Figure A.18. CV curves at various scan rate for c-VO_2 electrode at specific cathode/anode window. a,c) in cathodic and anodic windows, respectively. b,d) Capacitive (shaded area) and diffusion-controlled (cavity area) contribution to charge storage of c-VO_2 electrode in cathodic and anodic windows, respectively.

Figure A.19. High-rate long-term cycling stability of a-VO_2 electrode at 60C in both cathodic and anodic windows. A rate of 1C corresponds to 200 mA g^{-1}.

Figure A.20. The electrochemical performance of bipolar a-VO_2 based symmetric device. a) First ten cycles activation of a-VO_2 based symmetric device at 1C. b) CV curves at various scan rate of 0.2, 0.4, 0.6, 0.8 mV s^{-1} of a-VO_2 symmetric device after activation.

Figure A.21. Overcharging and overdischarging characteristics of the a-VO_2 symmetric cell at 1C. a) Over charge performance in the voltage range of 0 to 3.3 V. b) Over discharge performance in the voltage range of −0.3 to 3.0 V.

Figure A.22. The polarity swap test of the a-VO_2 symmetric cell. Comparison of discharge profiles at 1C before and after electrode reversion.

Figure A.23. Self-discharge properties of the individual electrode and the entire device. a) Photograph of a soft-packed pouch cell demonstration of a-VO_2 symmetric cell. b) The stability of open-circuit potential as a function time. c-e) The discharge behavior of the VO_2//Na cell at cathodic window (c), anodic window (d), and VO_2 symmetric cell (e) after 100 hours of open circuit, the cell retains nearly 90% of its initial capacity at 2C.

Figure B.1. Structural information on the CNF papers including cross-sectional SEM of the a) 40/500 and b) 50/500 architectures; c) X-ray diffraction; and d) Raman spectroscopy.

Figure B.2. Cyclic voltammograms at various sweep rates for cells containing a) 40/500 and b) 50/500 carbon nanofoams.

Figure B.3. a) Galvanostatic cycling at a current of 100 mA g_T^{-1}; b) galvanostatic rate retention; and long-term cycling of c) 50/500 CNF paper and d) 40/500 paper at a current density of 100 mA g_T^{-1}.

Figure B.4. Galvanostatic cycling (100 mA g^{-1}) of Na-ion half-cell containing Lydall carbon-paper as the cathode.

Figure B.5. a) Normalized diffusion coefficient derived from a GITT experiment and b) *b*-value analysis to differentiate regimes of differing charge-storage mechanism.

Figure B.6. Galvanostatic sodiation curves for galvanostatic intermittent titration (GITT) tested with a current pulse of 10 mA g_T^{-1} for 30 min followed by a relaxation period of 2 hours.

Figure B.7. Cyclic voltammograms of the 40/500 (a,c,e) and 50/500 (b,d,f) CNF electrodes with a,b) current normalized only to area c,d) current normalized to area and sweep rate and e,f) current normalized to area and the square root of sweep rate.

Figure B.8. Capacity distribution from the sloping region (solid) and from the plateau region (shaded) for both the 40/500 (red) and the 50/500 (blue) CNF paper electrodes.

Figure B.9. Sloping and total discharge capacity from galvanostatic cycling at 50 mA g_T^{-1} as a compared to the relative intensity of the D- and G-bands from Raman spectroscopy.

List of Tables

Acknowledgments

As far back as I can remember, I always told people that I wanted to be a “scientist” when I grew up. Though I certainly misunderstood what that actually entailed, I was firmly resolute on the matter. I have worked hard to make that dream a reality, but what enabled my success was a vast support system comprising mentors, friends, and family; I would like to thank some of them now.

First and foremost, I would like to thank Dr. Dunn for a number of things. His guidance has been instrumental in my development as a scientist. He constantly exposed me to new aspects of academia to push my boundaries as a researcher. In addition, he has cultivated a lab dynamic which is based on collaboration. Many of my lab mates are both close friends and wonderful scientists.

For brevity I will not list all of the Dunn lab members who have helped me along the way, but I would like to thank some of my current and former lab mates specifically. Jonathan Lau, Terri Lin, Dean Cheikh, and David Ashby were inspiring mentors; we continue to have lively scientific discussions after their graduation and I consider them integral to my knowledge of electrochemistry. Danielle Butts and Christopher Choi have been immeasurably helpful throughout my time in graduate school; we have accomplished a great deal as a trio and I am excited to see what both of you accomplish in the future. Matt Lai, Qiulong Wei, and I have worked on many impactful projects together. With their help and the work of Dongliang Chao, we have prepared an impressive manuscript on amorphous vanadium dioxide (Appendix A).

Through the Nippon Sheet Glass Fellowship, I worked with many wonderful people at Nippon Sheet Glass (NSG) in Itami, Japan. Kamitani-san, Yabuta-san, and Shimokawa-san

were extremely helpful in my transition into Japanese life. My time in Japan is one that I will always remember fondly.

I would also like to thank the Office of Naval Research and specifically the Naval Undersea Research Program (NURP) for funding (ONR: N00014-17-1-2244). Maria Medeiros, Bob Nowak, Eric Dow, and Rear Admiral Millard Firebaugh provided invaluable feedback which significantly improved my scientific presentations. In conjunction with the funding from NURP, I spent two summers working at the Naval Research Laboratory through the Naval Research Enterprise Internship Program (NREIP).

At NRL, I worked heavily with Debra Rolison, Jeff Long, Megan Sassin, and Chris Chervin on a variety of projects including carbon nanofoam electrodes for Na-ion batteries. We published this work (DOI: 10.1016/j.ensm.2019.05.040) and a modified version is included in Appendix B. Working with these inquisitive and diligent researchers so closely has enhanced my critical thinking and writing skills tremendously. I look forward to working with all of them in the future.

My friends in California, who have also been pertinent to this journey, also deserve appreciation. Tait McLouth, Nicole Carpentier, Grace Whang, Alexander Cheikh, and I have shared many unforgettable memories. Graduate school can be both frustrating and arduous at times, but my time spent with all of you always had me laughing and at ease.

I would also like to thank my committee members (Aaswath Raman, Yongjie Hu, and Yang Yang) for their comments and constructive criticism.

Lastly, I would like thank my wife, Sarah. Without her patience and unyielding support, this journey would have been much more difficult, if not impossible. Having a partner who supports my dreams has easily been my greatest treasure in life.

Vita

2010–2015 *Bachelor of Science, Materials Science and Engineering*

2015–2020 *Graduate Student Researcher, Materials Science and Engineering*

Publications, Patents, and Presentations

- J. Ko, P. Paul, G. Wan, N. Seitzman, **R.H. DeBlock,** B. Dunn, S. Pylypenko, M. Toney, J. Welker, "NASICON $Na_3V_2(PO_4)_3$ Enables Quasi–Two-Stage Na^+ and Zn^{2+} Intercalation for Multivalent Zn-ion Batteries", *Chemsitry of Materials*, **32**, 3028–3035 (2020)
- O. Munteshari, A. Borenstein, **R.H. DeBlock**, J. Lau, G. Whang, Y. Zhou, A. Likitchatchawankun, R. Kaner, B. Dunn, L. Pilon, "Calorimetric measurements for activated carbon electrodes in neat or diluted ionic liquid electrolytes under large potential windows", *ChemSusChem*, **13**, 1013–1026 (2019).
- C. Choi, D.S. Ashby, D.M. Butts, **R.H. DeBlock**, Q. Wei, J. Lau, B. Dunn, "Bridging the Power and Energy Gap with Pseudocapacitive Materials", *Nature Reviews Materials*, (2019).
- **R.H. DeBlock**, J.S. Ko, M.B. Sassin, A.N. Hoffmaster. B. Dunn, D.R. Rolison, J.W. Long, "Carbon nanofoam paper enables high-rate and high-capacity Na-ion storage", *Energy Storage Materials*, **21**, 481-486 (2019)
- D.S. Ashby, **R.H. DeBlock**, C.S. Choi, W. Sugimoto, B.S. Dunn, "Electrochemical and Spectroscopic Analysis of the Ionogel–Electrode Interface", *ACS Applied Materials & Interfaces*, **11** (12), 12088-12097 (2019)
- J. Lau*, **R.H. DeBlock***, D.M. Butts, D.S. Ashby, C.S. Choi and B.S. Dunn. "Sulfide Solid Electrolytes for Lithium Battery Applications." *Advanced Energy Materials,* **8**, 1800933 (2018)

- E.P. Young, J. Park, T. Bai, C.S. Choi, **R.H. DeBlock**, M. Lange, S. Poust, J. Tice, C. Cheung, B.S. Dunn, M.S. Goorsky, V. Ozolinš, D.C. Streit, V. Gambin, “Wafer-Scale Black Arsenic–Phosphorus Thin-Film Synthesis Validated with Density Functional Perturbation Theory Predictions” *ACS Applied Nano Materials* **1** (9), 4737-4745 (2018)
- S. Fischer, J. Roeser, T.C. Lin, **R.H. DeBlock**, J.S. Lau, B.S. Dunn, F. Hoffmann, M. Froeba, A. Thomas, S.H. Tolbert, “A Metal-Organic Framework with Tetrahedral Aluminate Sites as a Single-Ion Li^+ Solid Electrolyte” *Angewandte Chemie*, **130** (2018)
- D.S. Ashby, **R.H. DeBlock**, C.H. Lai, C.S. Choi, B.S. Dunn, “Patternable, Solution-Processed Ionogels for Thin-Film Lithium-Ion Electrolytes” *Joule*, **1**, 1-15 (2018)
- L. Zuo, H. Guo, D.W. deQuilettes, S. Jariwala, N.D. Marco, S. Dong, **R.H. DeBlock**, D. Ginger, B.S. Dunn, M. Wang, Y. Yang, “Polymer-modified halide perovskite films for efficient and stable planar heterojunction solar cells” *Science Advances* **3** (8) (2017)
- J.S. Ko, V.V.T. Doan-Nguyen, H.S. Kim, X. Petrissans, **R.H. DeBlock**, C.S. Choi, J.W. Long, B.S. Dunn, “High-Rate Capability of Na_2FePO_4F Nanoparticles by Enhancing Surface Carbon Functionality for Na-Ion Batteries” *Journal of Materials Chemistry A*, **5**, 18707-18715, (2017) Journal of Materials Chemistry A (2017)
- Microporous Aluminate Polymers and their Use as Solid Electrolytes and Conductive Binders for Lithium-ion Batteries, U.S. Provisional Patent (62/727,478), S.H. Tolbert, B.S. Dunn, S. Fischer, T.C. Lin, **R.H. DeBlock**, J.S. Lau, P.Y. Yee, (2019)
- “Free-standing, carbon fiber-paper–supported carbon nanofoams enable promising sodium-ion capacitors” R.H. DeBlock, J.S. Ko, M.B. Sassin, A.N. Hoffmaster. B. Dunn, D.R. Rolison, J.W. Long, International Conference on Advanced Capacitors, September 2019
- “Carbon nanofoam paper enables high-rate and high-capacity Na-ion storage" R.H. DeBlock, J.S. Ko, M.B. Sassin, A.N. Hoffmaster. B. Dunn, D.R. Rolison, J.W. Long, Materials Research Society, Phoenix, AZ, April 2019

Chapter 1: Introduction and Objectives

1.1. Background on Electrochemical Energy Storage

As electrochemical energy storage (EES) devices become ubiquitous in the 21st century, the development of new materials and devices continues to drive innovation. The primary focus of these efforts is to increase both specific energy (the amount of charge a device holds per weight) and specific power (how fast the charge is utilized per weight) which are beneficial for applications ranging from portable electronics to electric vehicles.[1,2] For the case of electric vehicles, greater specific energy leads to a longer driving range and greater specific power allows for faster charging.[3] As readily seen in Figure 1.1, typical lithium-ion batteries (LIBs) excel in their energy density, but are somewhat slow and limited to charge/discharge timescales on the order of hours. In comparison, capacitors have extremely fast response times, but store limited charge. Ideal device progress would push performance into the upper right-hand corner of the graph to compete with the performance of an internal combustion engine.

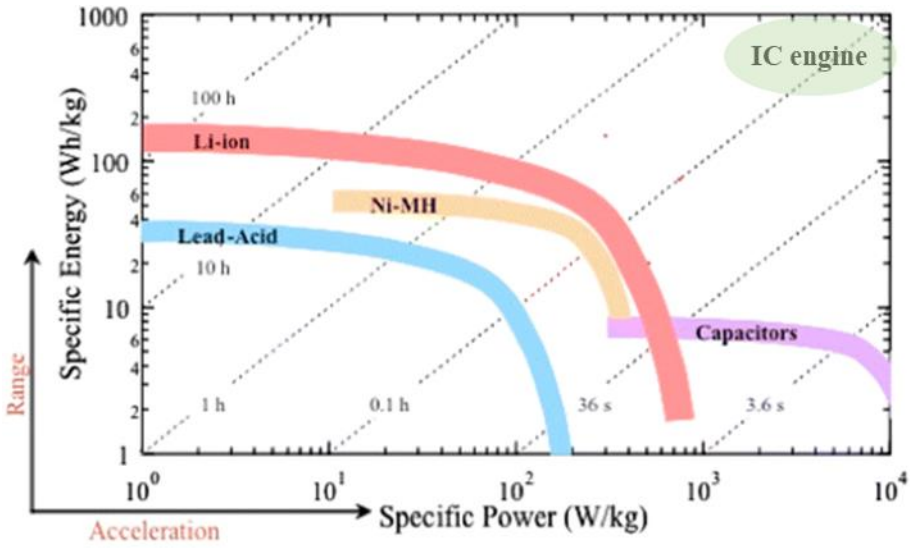

Figure 1.1. Ragone plot comparing the specific energy and specific power of common energy storage devices.[4] Modified from its original version.

Generally, materials which comprise the EES devices determine performance and are classified by the mechanism in which they store charge (Figure 1.2). Each of these mechanisms are discussed throughout this dissertation, but a brief summary is provided here. Electrical double-layer capacitors (EDLCs) store charge purely through ion adsorption/desorption at the surface of a porous material, typically carbon. This process is extremely fast, but only stores a limited amount of charge.[5] In comparison, battery-type materials undergo chemical reactions via the oxidation/reduction of transition metal ions in the crystal lattice.[3] This process results in a phase change which typically limits the speed and longevity of most battery materials. Pseudocapacitive materials, which will be expanded on in Chapter 4 and Appendix A, experience redox reactions, but no phase change and can subsequently operate at much faster rates than traditional battery materials. More specifically, pseudocapacitance occurs through either through surface redox reactions (i.e. $RuO_2 \cdot H_2O$) or intercalation reactions (T-Nb_2O_5).[6,7]

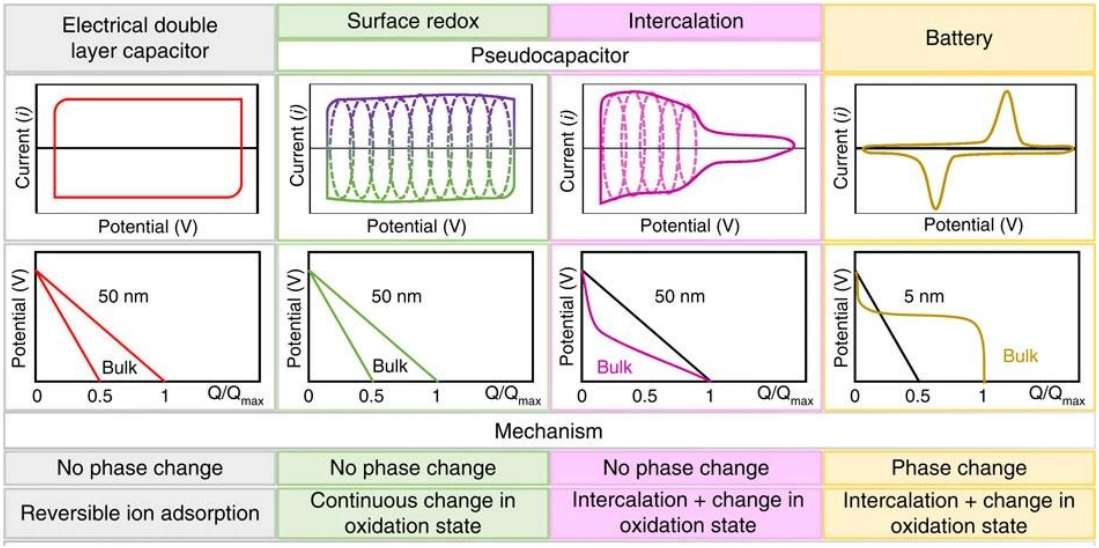

Figure 1.2. Differentiation of charge-storage mechanisms for capacitive (grey), pseudocapacitive (green and pink), and battery materials (yellow). Modified from its original version.[8]

1.2. Battery Fundamentals

Of all EES devices, lithium-ion batteries (LIBs) have been the storage of choice for portable electronics since the 1990s when they became commercially available. This is primarily due to their extremely high energy density when compared to other technologies such as lead acid and zinc carbon.[3,9] Over the past few decades, LIB technology has developed significantly and is now a 40 billion USD industry in 2020, projected to be more than 130 billion USD by 2027.[10] A schematic for a typical lithium-ion battery is depicted in Figure 1.3. below.

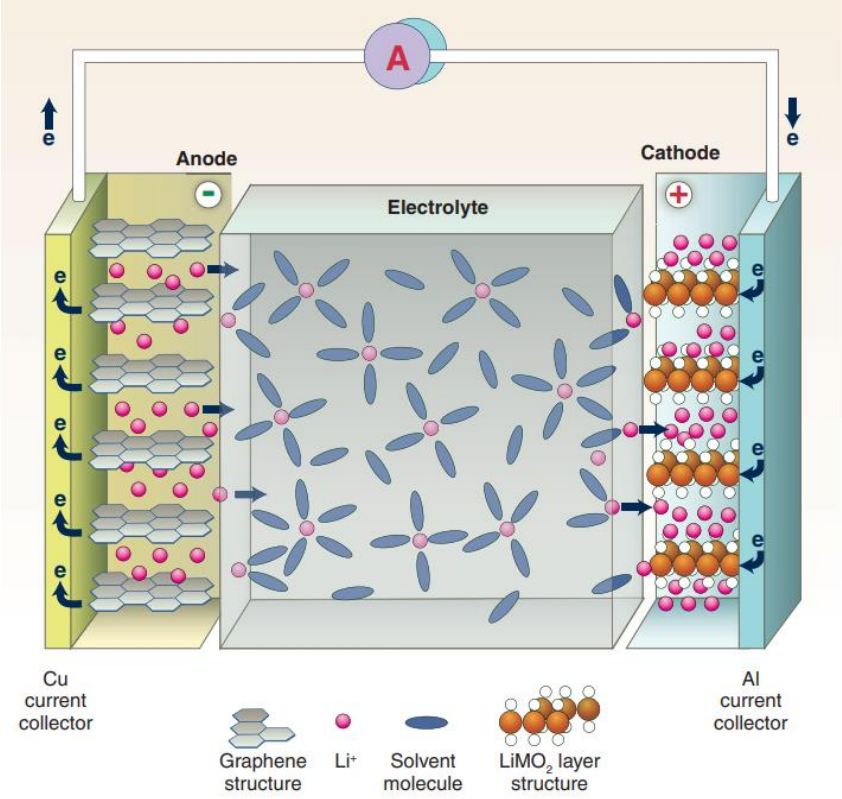

Figure 1.3. Schematic of a lithium-ion battery depicting the discharge process[3] (lithium ions removed from the graphite and inserted into the layered oxide compound).

Although there are variations of LIBs for different applications, each one contains the same basic components:

Electrodes

The electrodes of a LIB are what determine the energy density. Their function is to serve as hosts for lithium ion insertion/deinsertion. Upon charging, lithium ions flow from the cathode to the anode. This process is reversed on discharge. Electrodes are fabricated by mechanical mixing of active battery materials (the materials which store lithium ions) with conductive carbon

to decrease electronic resistance and binder to attach the particles to a metallic foil called a current collector.[11]

***Cathode*:** the high-potential electrode which generally consists of a layered, transition metal oxide (i.e. lithium cobalt oxide or LCO). These materials are usually layered structures which can intercalate lithium between crystallographic layers. The current collector for this electrode is nearly always aluminum because it is lightweight and has high electronic conductivity.

Anode: the low-potential electrode which is almost always graphite. The current collector for this electrode is copper. Although copper is heavier and more expensive, aluminum alloys with lithium at the low potentials seen on the anode side of the battery.[12]

Electrolyte

The electrolyte for a LIB serves as a conduction pathway for lithium ions to travel between electrodes. In order to force electrons through an external circuit, the electrolyte must necessarily be electronically insulating. Electrolytes are commonly organic solvents (mixtures of linear and cyclic carbonates) and a lithium-containing salt.[13]

1.3. Sodium-ion Batteries

Currently, lithium-ion batteries hold a large portion of the energy storage market, but questions remain regarding the abundance and economic viability of LIBs. As the battery market is on target to nearly triple by 2027,[10] the demand for the components of LIBS is set to increase dramatically. Currently, lithium is produced primarily in Australia and South America from salt

brine or lithium-containing rock with the vast majority of remaining reserves located in Chile (Figure 1.4.). Equally important to consider is that the Democratic Republic of the Congo produces roughly 50% of the global supply of cobalt, a common transition metal in LIB cathodes. This severe regionality of resources needed for LIBs is projected to be a large roadblock towards electric vehicle production.[14]

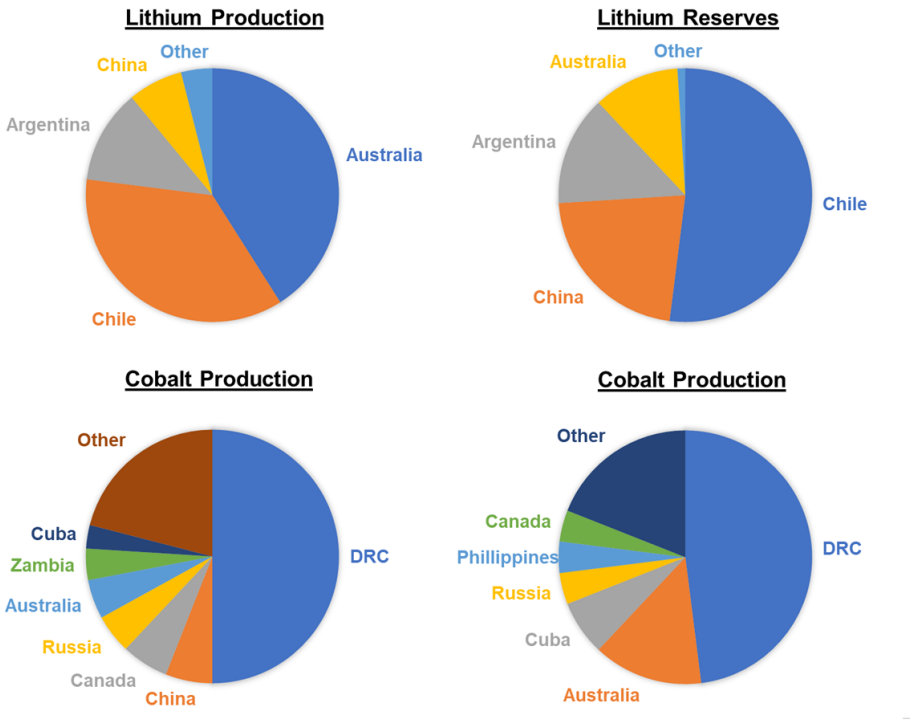

Figure 1.4. Geographical breakdown of the production and reserves for both lithium and cobalt.[15] Modified from its original version.

Table 1.1. Comparison of sodium and lithium ions as charge carriers for energy storage. Modified form its original version.[16]

	Sodium	Lithium
Price (for carbonates)	~0.2 $ kg^{-1}	~4.7 $ kg^{-1}
Specific Capacity	1.16 A h g^{-1}	3.86 A h g^{-1}
Voltage vs. S.H.E.	-2.7 V	-3.0 V
Ionic Radius	0.98 Å	0.69 Å
Melting Point	97.7 °C	180.5 °C

To combat the resource drawbacks of LIBS, many researchers are developing alternative chemistries.[17–20] One promising substitute is the sodium-ion battery (SIB). Lithium and sodium are quite similar from a chemistry perspective, but differ in a few key areas which are highlighted in Table 1.1. Although sodium is heavier and slightly larger than lithium, sodium-ion technology offers other benefits over LIBs. For instance, lithium precursors are orders of magnitude more expensive than those for sodium (primarily sodium carbonate) which are abundant and mined throughout the world. Due to its naturally high occurrence in the Earth's crust, sodium precursors are 1000–10,000 times more prevalent and 10 times cheaper than lithium ones.[15,16] Most cathodes for SIBs utilize iron, manganese, or vanadium as their transition metal for redox instead of cobalt which bolsters their position as a "greener" alternative to LIBs. From an engineering perspective, aluminum can be used as a current collector for both cathode and anode in SIBs (LIBs require copper on the anode side due to alloying reactions) which further reduces cost and weight.[21] A general schematic for SIBs is depicted in Figure 1.5. Similar to LIBs, SIBs typically utilize a layered oxide cathode and a carbon anode. In this case,

however, hard carbon (also known as non-graphitizable carbon) is used on the low-potential side.[22] This is discussed in detail in Appendix B of this dissertation. In recent years, the performance of SIBs has begun to approach that lithium-based storage and remains promising technology.[23–25]

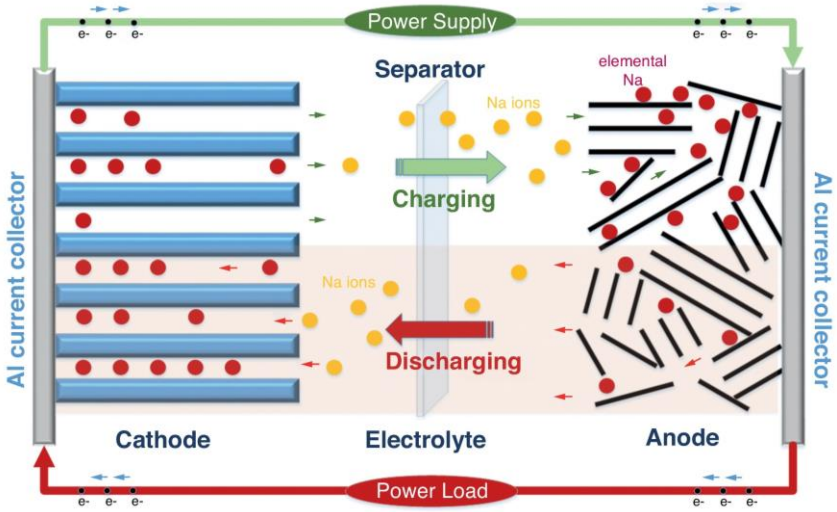

Figure 1.5. Schematic for a typical sodium-ion battery. The cathode is a layered oxide material, the anode is hard carbon, and the electrolyte is a sodium salt solvated in organic solvent.[22]

1.4. The Flammability of Common Battery Electrolytes

The flammability of LIB technology remains one of the largest impediments towards continued proliferation, especially in applications where safety is critical. Fires from LIBs are somewhat common in news media and have notoriously occurred in technology such as the Samsung Galaxy Note 7, the Boeing 787, and the Chevrolet Volt electric vehicle.[26] Furthermore, LIB fires can be difficult to extinguish and can release harmful chemicals upon ignition.[26] This

risk stems from the use of highly flammable organic solvents as electrolytes in LIBs. The majority of LIB systems utilize a solution of organic carbonates, such as ethylene carbonate and dimethyl carbonate, and lithium hexafluorophosphate salt. Generally, through internal short circuits (although mechanical abuse and electrical abuse can be triggers as well), a process called thermal runaway can occur by which the electrolyte will decompose in exothermic reactions causing subsequent degradation and heat.[27–29] To combat this issue, existing LIB devices incorporate safety vents and battery management systems to prevent overcharging. Even still, there are numerous conditions under which thermal runaway can occur (Figure 1.6.).[30]

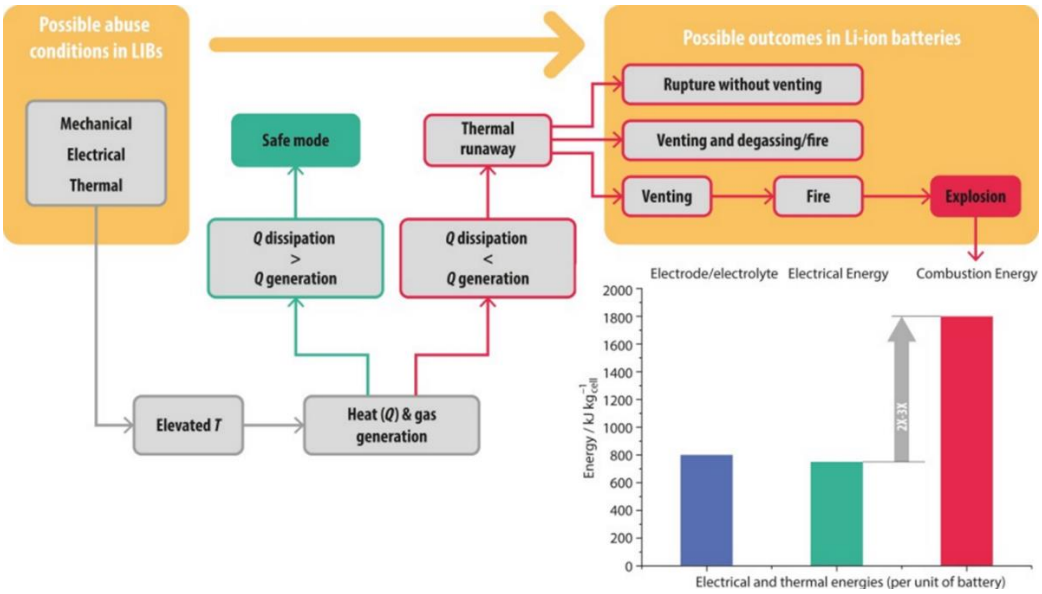

Figure 1.6. Schematic of potential pathways towards catastrophic failure in lithium-ion batteries.[30]

1.5. Sol-gel-derived, Pseudosolid Electrolytes

Solid electrolytes are a large step towards improving upon the safety and performance of sodium-ion battery systems. Not only does a thermally and chemically stable solid electrolyte provide a significant margin of safety, it also makes cell processing and fabrication more facile, and generally allows for a larger voltage window, ultimately improving upon the energy storage properties of the system.[31–33] On the cell level, solid electrolytes may allow for less packaging which would increase both energy and power density. Typically, significant portions of a battery pack's weight are attributed to preventing electrolyte leakage and containment in case of thermal runaway.[1,34,35]

Despite the tremendous advantages of solid electrolytes however, many challenges still remain. First solid electrolytes typically suffer from a significantly lower ionic conductivity than their liquid counterparts due to sluggish diffusion.[36] Second, highly-resistive, solid-solid interfaces between the electrode and electrode slow sodium-ion dynamics further.[37] Many solid electrolytes additionally have issues with stability against various electrode materials.[38]

As a route towards combining the favorable traits of solid and liquid electrolytes, a new class of "pseudosolid" electrolytes has recently emerged in the field of energy storage.[39–41] Ionogel electrolytes incorporate an ionic liquid (room temperature molten salt) into a matrix of nanoscopic porosity which provides mechanical stability. These electrolytes take advantage of the inherently high ionic conductivity of ionic liquids (up to 25 mS cm^{-1}) and the stability and ease of cell fabrication associated with solids. Ionic liquids have many other desirable traits for battery electrolytes including low vapor pressure, good thermal stability (>300°C), large voltage windows (some up to 5.5 V), and are generally inflammable. [42,43]

There are various materials which can provide mechanical stability to an ionogel. Polymers such as poly(methyl methacrylate) and poly(vinylidene fluoride-co-hexafluoropropylene) are the most common.[44–47] Alternately, inorganic materials such as silica can also encapsulate an ionic liquid. [48,49] Figure 1.7. details the synthesis and functional components of a silica-supported ionogel derived from sol-gel synthesis. Thus far, research into ionogel electrolytes for sodium-ion batteries is fairly limited and consists of primarily polymer-based matrices. In Chapter 2, we synthesize sol-gel derived ionogel electrolytes and apply them in sodium-ion devices as nonflammable alternatives to carbonate electrolytes. Chapter 3 also explores a pseudosolid electrolyte supported by sol-gel-derived silica, but a long-chain glyme replaces the ionic liquid to improve stability with sodium metal.

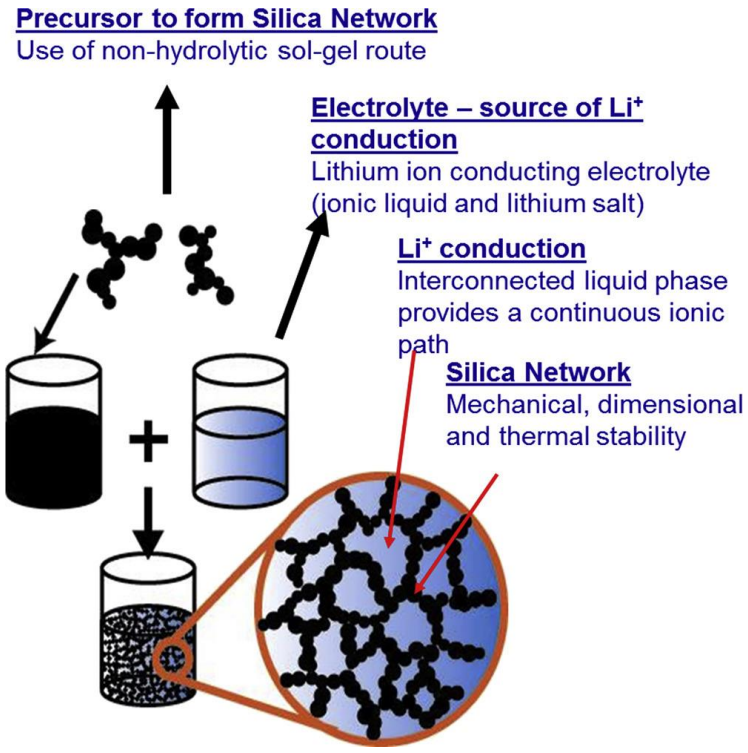

Figure 1.7. Description of ionogel components and their functions in a pseudosolid electrolyte.

1.6. The Low Capacity and Poor Rate Capability of Current LIB Cathode Materials

In recent years, lithium-ion battery materials have plateaued with regard to both energy density and power density.[50–52] Technology such as electric vehicles still requires significant improvements in both energy and power density of electrochemical energy storage for full market breakthrough and competition with internal combustion engines (Figure 1.8.).

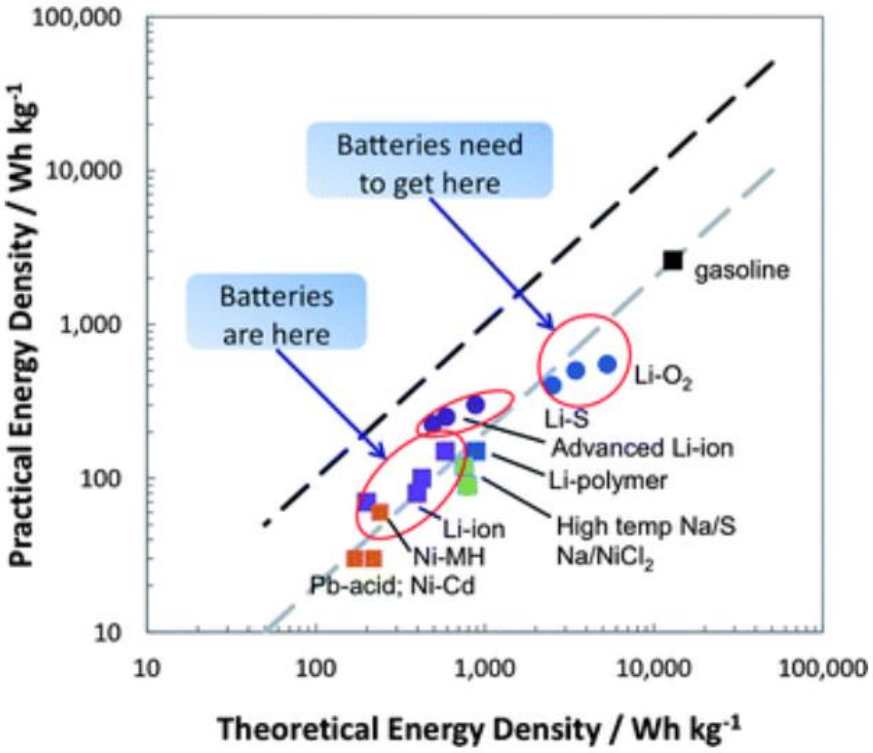

Figure 1.8. Theoretical specific energy compared to practical specific energy delivery for a variety of electrochemical energy storage devices.

Research to date on high-rate electrode materials has concentrated on crystalline materials where crystallographic pathways such as open channels or sparsely occupied planes lead to high-ion mobility.[53,54] In contrast, amorphous materials do not have such structural features and, although these materials have been investigated as electrolytes, there are relatively few studies on their use as electrodes in batteries.[55,56] Recently however, researchers have begun investigating amorphous materials due to their open framework, isotropic diffusion pathways, lack of phase change, and better stress accommodation.[57–59] Our work on amorphous vanadium dioxide (a-VO_2) offers a dramatic change in common perceptions of

battery materials as the material exhibits high energy density at high discharge rate (Chapter 4 and Appendix A). In combination with a linear discharge curve under galvanostatic conditions, a–VO_2 delivers a high capacity over 3 volts in sodium electrolyte.

1.7. Objectives

1. Create a novel, pseudosolid-state electrolyte for Na-ion batteries that offers the ionic conductivity of a liquid electrolyte in combination with the chemical and thermal stability and enhanced safety of a solid-state electrolyte.
    a. Chapter 2 details the synthesis and electrochemical performance of an ionogel electrolyte created through the encapsulation of an ionic liquid within an organosilica matrix. Chapter 3 explores the adaptation of the sol-gel synthesis techniques to a glyme-based electrolyte which boasts incredibly stable cycling in contact with sodium metal.

2. Investigate the potential of amorphous materials as hosts for high-performance, sodium-ion batteries.
    a. Chapter 4 investigates the use of amorphous vanadium dioxide as a sodium-ion battery electrode. This work is improved upon in Appendix A by growing amorphous VO_2 onto a graphene foam scaffold. In Appendix B, examines the rate capability and charge-storage mechanisms of an amorphous carbon nanofoam electrode.

1.8. References

1. Saw, L. H., Ye, Y. & Tay, A. A. O. Integration issues of lithium-ion battery into electric vehicles battery pack. *Journal of Cleaner Production* **113**, 1032–1045 (2016).
2. Blomgren, G. E. The Development and Future of Lithium Ion Batteries. *Journal of The Electrochemical Society* **164**, A5019–A5025 (2017).
3. Dunn, B., Kamath, H. & Tarascon, J.-M. Electrical Energy Storage for the Grid: A Battery of Choices. *Science* **334**, 928–935 (2011).
4. McCloskey, B. D. Expanding the Ragone Plot: Pushing the Limits of Energy Storage. *J. Phys. Chem. Lett.* **6**, 3592–3593 (2015).
5. Sharma, P. & Bhatti, T. S. A review on electrochemical double-layer capacitors. *Energy Conversion and Management* **51**, 2901–2912 (2010).
6. Choi, C. *et al.* Achieving high energy density and high power density with pseudocapacitive materials. *Nat Rev Mater* **5**, 5–19 (2020).
7. Augustyn, V., Simon, P. & Dunn, B. Pseudocapacitive oxide materials for high-rate electrochemical energy storage. *Energy & Environmental Science* **7**, 1597 (2014).
8. Lukatskaya, M. R., Dunn, B. & Gogotsi, Y. Multidimensional materials and device architectures for future hybrid energy storage. *Nature Communications* **7**, 12647 (2016).
9. Lu, L., Han, X., Li, J., Hua, J. & Ouyang, M. A review on the key issues for lithium-ion battery management in electric vehicles. *Journal of Power Sources* **226**, 272–288 (2013).
10. Choudhary, A. & Prasad, E. Lithium-ion Battery Market by Component (Cathode, Anode, Electrolytic Solution, and Others), End-use Industry [Electrical & Electronics (Smartphones &Tablet/PC, UPS, and Others) and Automotive (Cars, Buses, &Trucks; Scooters & Bikes;and Trains & Aircraft), and Industrial (Cranes & Forklift, Mining Equipment, and Smart Grid & Renewable Energy Storage): Global Opportunity Analysis and Industry Forecast, 2019–2027. *Allied Market Research* (2020).

11. Li, J., Daniel, C. & Wood, D. Materials processing for lithium-ion batteries. *Journal of Power Sources* **196**, 2452–2460 (2011).
12. Braithwaite, J. W. Corrosion of Lithium-Ion Battery Current Collectors. *J. Electrochem. Soc.* **146**, 448 (1999).
13. Aurbach, D. *et al.* Design of electrolyte solutions for Li and Li-ion batteries: a review. *Electrochimica Acta* **50**, 247–254 (2004).
14. Olivetti, E. A., Ceder, G., Gaustad, G. G. & Fu, X. Lithium-Ion Battery Supply Chain Considerations: Analysis of Potential Bottlenecks in Critical Metals. *Joule* **1**, 229–243 (2017).
15. Vaalma, C., Buchholz, D., Weil, M. & Passerini, S. A cost and resource analysis of sodium-ion batteries. *Nature Reviews Materials* **3**, 18013 (2018).
16. Palomares, V. *et al.* Na-ion batteries, recent advances and present challenges to become low cost energy storage systems. *Energy Environ. Sci.* **5**, 5884 (2012).
17. Massé, R. C., Uchaker, E. & Cao, G. Beyond Li-ion: electrode materials for sodium- and magnesium-ion batteries. *Sci. China Mater.* **58**, 715–766 (2015).
18. Peng, L., Zhu, Y., Chen, D., Ruoff, R. S. & Yu, G. Two-Dimensional Materials for Beyond-Lithium-Ion Batteries. *Adv. Energy Mater.* **6**, 1600025 (2016).
19. Ponrouch, A., Frontera, C., Bardé, F. & Palacín, M. R. Towards a calcium-based rechargeable battery. *Nature Mater* **15**, 169–172 (2016).
20. Li, Q., Chen, J., Fan, L., Kong, X. & Lu, Y. Progress in electrolytes for rechargeable Li-based batteries and beyond. *Green Energy & Environment* **1**, 18–42 (2016).
21. Chayambuka, K., Mulder, G., Danilov, D. L. & Notten, P. H. L. Sodium-Ion Battery Materials and Electrochemical Properties Reviewed. *Adv. Energy Mater.* **8**, 1800079 (2018).
22. Tang, J., Dysart, A. D. & Pol, V. G. Advancement in sodium-ion rechargeable batteries. *Current Opinion in Chemical Engineering* **9**, 34–41 (2015).

23. Sawicki, M. & Shaw, L. L. Advances and challenges of sodium ion batteries as post lithium ion batteries. *RSC Adv.* **5**, 53129–53154 (2015).
24. Chen, L. *et al.* Readiness Level of Sodium-Ion Battery Technology: A Materials Review. *Adv. Sustainable Syst.* **2**, 1700153 (2018).
25. Delmas, C. Sodium and Sodium-Ion Batteries: 50 Years of Research. *Adv. Energy Mater.* **8**, 1703137 (2018).
26. Larsson, F., Andersson, P., Blomqvist, P. & Mellander, B.-E. Toxic fluoride gas emissions from lithium-ion battery fires. *Sci Rep* **7**, 10018 (2017).
27. Arbizzani, C., Gabrielli, G. & Mastragostino, M. Thermal stability and flammability of electrolytes for lithium-ion batteries. *Journal of Power Sources* **196**, 4801–4805 (2011).
28. Feng, X. *et al.* Thermal runaway mechanism of lithium ion battery for electric vehicles: A review. *Energy Storage Materials* **10**, 246–267 (2018).
29. Wang, Q., Jiang, L., Yu, Y. & Sun, J. Progress of enhancing the safety of lithium ion battery from the electrolyte aspect. *Nano Energy* **55**, 93–114 (2019).
30. Kalhoff, J., Eshetu, G. G., Bresser, D. & Passerini, S. Safer Electrolytes for Lithium-Ion Batteries: State of the Art and Perspectives. *ChemSusChem* **8**, 2154–2175 (2015).
31. Wang, Y. *et al.* Development of solid-state electrolytes for sodium-ion battery–A short review. *Nano Materials Science* **1**, 91–100 (2019).
32. Lau, J. *et al.* Sulfide Solid Electrolytes for Lithium Battery Applications. *Adv. Energy Mater.* **8**, 1800933 (2018).
33. Li, J., Ma, C., Chi, M., Liang, C. & Dudney, N. J. Solid Electrolyte: the Key for High-Voltage Lithium Batteries. *Adv. Energy Mater.* **5**, 1401408 (2015).
34. Balakrishnan, P. G., Ramesh, R. & Prem Kumar, T. Safety mechanisms in lithium-ion batteries. *Journal of Power Sources* **155**, 401–414 (2006).

35. Warner, J. *The handbook of lithium-ion battery pack design: chemistry, components, types and terminology*. (Elsevier, 2015).
36. Vignarooban, K. *et al.* Current trends and future challenges of electrolytes for sodium-ion batteries. *International Journal of Hydrogen Energy* **41**, 2829–2846 (2016).
37. Zhao, C. *et al.* Solid-State Sodium Batteries. *Adv. Energy Mater.* **8**, 1703012 (2018).
38. Kim, J.-J., Yoon, K., Park, I. & Kang, K. Progress in the Development of Sodium-Ion Solid Electrolytes. *Small Methods* **1**, 1700219 (2017).
39. Chen, N., Zhang, H., Li, L., Chen, R. & Guo, S. Ionogel Electrolytes for High-Performance Lithium Batteries: A Review. *Adv. Energy Mater.* **8**, 1702675 (2018).
40. Le Bideau, J., Viau, L. & Vioux, A. Ionogels, ionic liquid based hybrid materials. *Chem. Soc. Rev.* **40**, 907–925 (2011).
41. Noor, S. A. M., Bayley, P. M., Forsyth, M. & MacFarlane, D. R. Ionogels based on ionic liquids as potential highly conductive solid state electrolytes. *Electrochimica Acta* **91**, 219–226 (2013).
42. Galiński, M., Lewandowski, A. & Stępniak, I. Ionic liquids as electrolytes. *Electrochimica Acta* **51**, 5567–5580 (2006).
43. Watanabe, M. *et al.* Application of Ionic Liquids to Energy Storage and Conversion Materials and Devices. *Chem. Rev.* **117**, 7190–7239 (2017).
44. Mohd Noor, S. A., Yoon, H., Forsyth, M. & MacFarlane, D. R. Gelled ionic liquid sodium ion conductors for sodium batteries. *Electrochimica Acta* **169**, 376–381 (2015).
45. Kumar, D. & Hashmi, S. A. Ionic liquid based sodium ion conducting gel polymer electrolytes. *Solid State Ionics* **181**, 416–423 (2010).
46. Hashmi, S. A. *et al.* Ionic liquid-based sodium ion-conducting composite gel polymer electrolytes: effect of active and passive fillers. *J Solid State Electrochem* **20**, 2817–2826 (2016).

47. Mendes, T. C. *et al.* Supported Ionic Liquid Gel Membrane Electrolytes for a Safe and Flexible Sodium Metal Battery. *ACS Sustainable Chemistry & Engineering* (2019) doi:10.1021/acssuschemeng.8b06212.
48. Ashby, D. S., DeBlock, R. H., Lai, C.-H., Choi, C. S. & Dunn, B. S. Patternable, Solution-Processed Ionogels for Thin-Film Lithium-Ion Electrolytes. *Joule* **1**, 344–358 (2017).
49. Wang, S. *et al.* Comparative studies on electrochemical cycling behavior of two different silica-based ionogels. *Journal of Power Sources* **301**, 299–305 (2016).
50. Thackeray, M. M., Wolverton, C. & Isaacs, E. D. Electrical energy storage for transportation—approaching the limits of, and going beyond, lithium-ion batteries. *Energy & Environmental Science* **5**, 7854 (2012).
51. Luntz, A. Beyond Lithium Ion Batteries. *The Journal of Physical Chemistry Letters* **6**, 300–301 (2015).
52. Cabana, J., Monconduit, L., Larcher, D. & Palacín, M. R. Beyond Intercalation-Based Li-Ion Batteries: The State of the Art and Challenges of Electrode Materials Reacting Through Conversion Reactions. *Advanced Materials* **22**, E170–E192 (2010).
53. Bresser, D. *et al.* The importance of “going nano” for high power battery materials. *Journal of Power Sources* **219**, 217–222 (2012).
54. Kang, B. & Ceder, G. Battery materials for ultrafast charging and discharging. *Nature* **458**, 190–193 (2009).
55. Yamauchi, A., Sakuda, A., Hayashi, A. & Tatsumisago, M. Preparation and ionic conductivities of (100 − x)(0.75Li2S·0.25P2S5)·xLiBH4 glass electrolytes. *Journal of Power Sources* **244**, 707–710 (2013).
56. Sakuda, A., Hayashi, A. & Tatsumisago, M. Sulfide Solid Electrolyte with Favorable Mechanical Property for All-Solid-State Lithium Battery. *Sci Rep* **3**, 2261 (2013).

57. Wei, Z. *et al.* From Crystalline to Amorphous: An Effective Avenue to Engineer High-Performance Electrode Materials for Sodium-Ion Batteries. *Advanced Materials Interfaces* 1800639 (2018) doi:10.1002/admi.201800639.
58. Delmer, O., Balaya, P., Kienle, L. & Maier, J. Enhanced Potential of Amorphous Electrode Materials: Case Study of RuO2. *Advanced Materials* **20**, 501–505 (2008).
59. Uchaker, E. *et al.* Better than crystalline: amorphous vanadium oxide for sodium-ion batteries. *J. Mater. Chem. A* **2**, 18208–18214 (2014).

Chapter 2: Siloxane-modified, silica-based ionogel as a pseudosolid electrolyte for sodium-ion batteries

We employ a one-pot, siloxane-modified sol-gel synthesis to encapsulate an ionic liquid within a silica matrix leading to a monolithic ionogel electrolyte (IG). This pseudosolid electrolyte provides a non-flammable alternative to traditional carbonate liquids and demonstrates a wide stability window (5V) as well as a high ionic conductivity (~1 mS cm^{-1}). Electrochemical methods reveal reversible cycling with both high- and low-potential electrodes materials in both modified half-cell and full-cell testing formats.

2.1 Introduction

Lithium-ion batteries (LIBs) have become the battery of choice for mobile electronics and electric vehicles due to their versatility and high energy density.[1] However, the localized origin of lithium is a crucial limitation as the LIB market is predicted to more than triple in size between 2020 and 2027.[2] Moreover, the world supply of cobalt, a main component of common cathode materials in LIBs, is primarily excavated as a by-product of copper or nickel mines which causes widely varying prices and concerns over future availability.[3]

The potential limitations in LIBS have led to investigations of alternative chemistries. One such substitute is the sodium-ion battery (SIB) which uses a slightly larger, more electropositive sodium-ion as the energy carrier. In general, SIBs exhibit similar characteristics to LIBs, albeit with generally slower kinetics and a smaller number of viable intercalation electrode materials as a consequence of the larger ionic radius. Despite these drawbacks, sodium is 1,000–10,000 times more abundant than lithium and is found in the Earth's crust globally.[4] Many prominent cathode materials for SIBs contain iron, manganese, or vanadium which are more plentiful than cobalt.[5] Additionally, sodium does not alloy with aluminum appreciably which allows for its use as the current collector for the negative electrode as opposed to LIBs which utilize copper. Together,

these features make sodium-ion batteries somewhat less expensive than their lithium counterparts and particularly desirable for applications such as grid-level storage.[5]

Another readily observable problem with current LIB technology is their thermal instability. Traditional liquid electrolytes in LIBs consist of a lithium salt (generally lithium hexafluorophosphate) solvated in a mixture of organic carbonates, typically a mixture of ethylene carbonate and dimethyl carbonate which are highly flammable. Excessive heat from operation or environment often leads to thermal runaway whereby thermal energy induces unfavorable side reactions which produce additional heat and flammable by-products.[6]

Ionic liquids (commonly called room-temperature ionic liquids) have recently emerged as a class of solvents which have potential applications in numerous fields such as catalysis, green synthesis, and energy storage due to their unique characteristics when compared to traditional solvents. Although numerous ionic liquids exist, most consist of a bulky, asymmetrical cation (such as imidazole, pyrrolidine, piperidine, etc.) coupled with an anion which range from simple halides to more complicated sulfonamides.[7] The high formation energy of efficient, three-dimensional packing leads to low melting points below 100°C.[8] A number of ionic liquids possess properties desirable for electrolytes such as stability (thermal, electrochemical, etc.), reasonable levels of ionic conductivity, low vapor pressure, nonflammability, and effective solvation of alkali ions. In the field of energy storage, the use of ionic liquids as an electrolyte in supercapacitors widens their voltage window and increases energy density.[9] A number of battery-type materials used in lithium-ion systems also function with ionic liquid electrolytes.[10]

Pseudosolid electrolytes called “ionogels” address the problems of flammability by taking advantage of the nonvolatility of ionic liquids. One family of ionogels is based on having ionic liquids swelled into polymer matrices creating freestanding solids.[11,12] Although electrolytes for lithium-ion battery research are much more common (primarily for non-flammable and high-temperature applications)[10] a small number of reports exist regarding ionogels for sodium-ion

batteries. Singh et. al, for example, reported an ionogel electrolyte consisting of an ionic liquid immobilized by poly (ethylene oxide) (PEO).[13] Other polymer hosts include poly (vinyl chloride) (PVC)[14], poly (methyl methacrylate) (PMMA)[15], poly (ethylene glycol) diacrylate (PEGDA)[16], and, most commonly, poly (vinylidine fluoride-co-hexafluoropropylene) (PVDF-HFP).[17–19] Although polymer-based ionogels exhibit reasonable electrochemical properties and are easy to synthesize, they suffer from thermal degradation when the polymer either melts or decomposes, typically between 100–150°C.

A second family of ionogels involves sol-gel synthesis to encapsulate ionic liquids within a mesoporous silica matrix.[20] In typical sol-gel syntheses, a metal alkoxide precursor undergoes hydrolysis and condensation polymerization. In the case of silica sol-gel reactions, hydrolysis produces Si–OH groups which undergo condensation to form Si–O–Si bonds. The resulting sol is comprised of colloidal SiO_2 particles suspended in a solvent. Upon gelation, a two-phase system forms consisting of a network of 5-10 nm amorphous silica particles in combination with a solvent phase that fills the pores. Removal of the solvent leads to the formation of highly porous solids known as xerogels (ambient drying) or aerogels (supercritical drying). When an ionic liquid is used as the solvent instead of a volatile one such as ethanol, no evaporation occurs. The resulting material is a macroscopically rigid, nonporous material in which the ionic liquid is trapped by capillary forces in the nanometer sized pores in the silica network.[21]

The inorganic ionogel synthesis route has several advantages. First, the amount of ionic liquid incorporated into the solid can reach near 90 wt% by controlling the volume of the inorganic phase. The high weight loading of ionic liquid allows for electrochemical properties similar to those of the neat ionic liquid within the mesoscopic pores while simultaneously maintaining the structure of a macroscopic solid. Second, because all precursors are in the liquid phase, ionogels can permeate into porous electrode architectures and maintain intimate solid-liquid contact to improve transport kinetics. Liquid-phase synthesis also allows for the creation of thinner electrolytes or

arbitrary form factors through spin-coating or infiltration.[20] The ability to have the in-situ formation of a mesoporous silica network distinguishes sol-gel-derived ionogels from those formed through the incorporation of fumed silica, i.e. physical gels.[22]

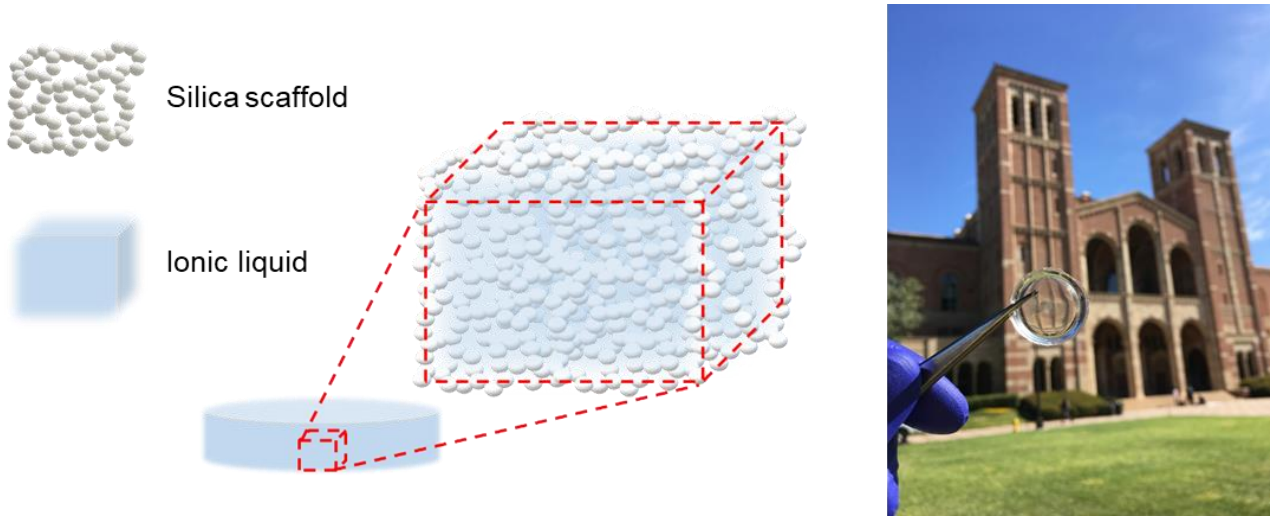

Figure 2.1. Schematic representation and photograph of our ionogel electrolyte for sodium-ion batteries.

In the present work, we use sol-gel synthesis to form a siloxane-modified silica scaffold that traps an ionic liquid electrolyte which contains a solvated sodium salt (Figure 2.1.). This process leads to a freestanding solid electrolyte for sodium-ion battery applications. In addition to characterizing the structural and chemical nature of the pseudosolid electrolyte, we incorporate ionogel electrolytes in electrochemical cells and evaluate their performance in sodium-ion batteries. Although a few ionogel electrolytes for sodium-ion batteries are reported in literature, this is the first demonstration of a full Na-ion battery based on an ionogel electrolyte and two insertion electrodes.

2.2. Experimental

Materials

Dimethylsiloxane-(25-30% ethylene oxide, 400 cSt) block copolymer (m-PDMS) was purchased from Gelest. 1-Butyl-1-methylpyrrolidinium bis(trifluoromethanesulfonyl)imide (99.9%) [PYR14][TFSI] was purchased from Millipore Sigma and dried at 100C under vacuum on a Schlenk line before use. Sodium(I) bis(fluorosulfonyl)imide (99.7%) [NaFSI] was purchased from Solvionic and was used as purchased. Trimethoxymethylsilane (98%) (MTMS), formic acid (98%), and all reagents used in the electrode synthesis were purchased from Sigma Aldrich.

Synthesis of ionogel electrolyte

A specific amount of trimethoxymethylsilane (MTMS) was combined with dimethylsiloxane block copolymer (m-PDMS) and formic acid (500 µL) to form the initial sol. This was allowed to stir for 10 minutes at a temperature of 30°C. An ionic liquid electrolyte (ILE) solution of 0.5M NaFSI in [PYR14][TFSI] was then added to the stirring mixture. The volume ratio of MTMS:m-PDMS:ILE was adjusted to create ionogels of varying composition. For example, the ★ composition had a volume ratio of MTMS:m-PDMS:ILE of 1.8:2:1. The initial total volume was kept at 850 µL and the amount of formic acid was held constant at 500 µL. The solution was subsequently vortex mixed and cast into ~2 cm^2 polypropylene molds. Gelation occurred within 1 hour. Samples were left to dry ambiently for 6 hours followed by 2 hours under vacuum and then overnight under vacuum at 70°C. Ionogel electrolytes (IGs) were appropriately sized for testing with a leather punch.

Synthesis of $Na_3V_2(PO_4)_3$@C (NVP)

NVP@C cathode was synthesized using a method adapted from literature.[23] Vanadium pentoxide (2 mmol) and anhydrous oxalic acid (6 mmol) were dissolved in water (10 mL) under

stirring in a water bath (80 °C) until the color of the solution turned blue. Then, glucose (2 mmol), sodium oxalate (3 mmol) and excess ammonium dihydrogen phosphate (6 mmol) were slowly added into the blue solution sequentially. Ethylene glycol (20 mL) was added dropwise into the above solution and stirred for one hour. The mixed solution was slowly dried at 100 °C under air flow. After the solution had dried completely, the powders were ground and then kept in a vacuum oven at 120 °C for 12 hours. Finally, the dried powder was further ground and annealed at 750 °C for 8 hours (5 °C min^{-1}) in Ar atmosphere.

Synthesis of $NaTi_2(P0_4)_3$@C (NTP)

NTP@C anode was synthesized by proper modification of the NVP recipe above. Titanium (IV) isopropoxide (2 mmol), sodium oxalate (1 mmol), dihydrogen phosphate (3 mmol), and glucose (2 mmol) were mixed into DI water (10 mL) sequentially under rapid stirring. After 5 minutes of stirring, ethylene glycol (20 mL) was then mixed into the solution. Once fully dissolved and homogenous, the solution was dried slowly at 100 °C under air flow. After the solution had dried completely, the powders were ground and then kept in a vacuum oven at 120 °C for 12 hours. Finally, the dried powder was further ground and annealed at 700 °C for 6 hours (5 °C min^{-1}) in Ar atmosphere.

Electrode preparation

For NVP@C electrodes, a slurry was obtained by mixing 85 wt% active material, 10 wt% Ketjen black carbon and 5 wt% PVDF binder in N-methyl-2-pyrrolidone (NMP) and coated on Al foils. For NTP@C electrodes, the ratios were kept the same, except that carboxymethyl cellulose (CMC) was used as the binder in water. The electrodes were dried in a vacuum oven at 120 °C overnight before testing. The mass loading of active material in electrodes was about 1.0 mg cm^{-2}. As described previously[24], overcapacitive activated carbon (AC) electrodes were created by

infiltrating nickel foam with a slurry of conductive carbons to a weight loading of ~10 mg cm^{-2}, with an area ratio of ~3:1, and a capacity ratio of ~10:1 activated carbon:NVP.

Electrochemical characterization

Ionic conductivity for both ionic liquid and ionogel electrolytes was calculated from electrochemical impedance spectroscopy (EIS) measured using two stainless steel blocking electrodes. An AC voltage of 10 mV was applied with frequencies ranging from 100 mHz to 500 kHz. Activation energy was calculated using an Arrhenius analysis with a linear regression fit R^2>0.995. The electrochemical stability window of the ionogel electrolyte was assessed using linear sweep voltammetry at a sweep rate of 0.1 mV s^{-1} with a platinum working electrode and a silver foil counter/reference electrode.

EIS was also utilized to assess cell resistance changes over time for various devices. Coin cells were constructed with ionogel electrolyte and various combinations of sodium metal and NVP electrodes. Impedance measurements were made on several cells: symmetric sodium (Na|IG|Na), symmetric NVP (NVP|IG|NVP), and an asymmetric configuration (Na|IG|NVP). The measurements were made immediately after cell construction and 72 hours later.

Galvanostatic cycling was performed in coin cell format with the ionogel electrolyte pressed between two electrodes. For half-cell devices, NVP was the working electrode and either sodium metal or activated carbon served as the counter/reference electrode. Capacity was normalized to the weight of the NVP in these devices. For full-cell cycling, NVP was the working electrode and NTP was the counter/reference electrode. An excess of 10 wt% NTP anode was used so capacity could be normalized solely to the NVP.

Physical characterization

The ionogel morphology was characterized by nitrogen gas adsorption analysis (ASAP2020 Plus, Micromeritics Instruments Corp.) After removal of ionic liquid from the sol-gel network as reported previously.[20] Briefly, the ionic liquid was solvent exchanged for acetone by soaking the ionogel electrolyte for three days in 20 mL acetone. The acetone was subsequently exchanged with liquid CO_2 and supercritically dried. This procedure prevents the sol-gel network from pore collapse and retains the morphology of the inorganic matrix when it contained the ionic liquid. TEM (T12, FEI) and SEM (Nova NanoSEM 230, FEI) images were obtained on solvent-exchanged gels after coating the samples with gold. Thermogravimetric analysis was carried out in air using a TA SDT Q600 analyzer at a heating rate of 10 °C min^{-1}. X-ray photoelectron spectroscopy (XPS; Kratos Axis Ultra) was performed using a monochromatic aluminum X-ray source with peak calibration determined using adventitious carbon. Fourier-transform infrared spectroscopy (FTIR; Jasco-670 Plus) measurements were performed on ionogel samples after casting onto PTFE sample cards. Young's modulus was calculated using nanoindentation experiments (n=5) taken on an MTS Nano Indenter XP. A Poisson ratio of 0.5 was used for the calculation of modulus.[25]

2.3 Results and Discussion

Synthesis and fundamental characterization

Sol-gel chemistry is often utilized to create porous, interconnected structures of various metal oxides. For instance, acid-catalyzed hydrolysis of silicon alkoxides (e.g. silicon tetraethylorthosilicate [TEOS]) produces silica scaffolds and proper selection of precursor tunes structural properties.[21] Multiple end groups can be changed from an ethoxy group ($-O-C_2H_5$) in tetrafunctional TEOS to a methacrylate group, vinyl group, phenyl group, etc. Alternatively, substitution with a methyl group terminates bonding for that section of the monomer making the

silane trifunctional.[26] In the present study, methyltrimethoxysilane (MTMS) is used as a means to impart hydrophobicity as well as increase porosity and mechanical robustness. Silica synthesized using MTMS retains the nonhydrolyzable methyl group in the final structure which provides electrostatic repulsion between neighboring silica chains and subsequent flexibility.[26] To provide further compliance, we also incorporate an organic silica component, poly(dimethylsiloxane) (PDMS) which has been employed successfully in ionogel electrolytes.[27] Flexibility, and more importantly structural integrity under compression, are vital to prevent mechanical failure of the electrolyte during construction of electrochemical cells which experience ~5 MPa of pressure in coin cell format.[28]

Equally as important as the silica network is the choice of ionic liquid electrolyte (ILE). In this work, we employ 1-butyl-1-methylpyrrolidinium bis(trifluoromethanesulfonyl)imide (also known as [PYR14][TFSI]) as the ionic liquid component and sodium bis(fluorosulfonyl)imide [Na][FSI] as the sodium-containing salt. [PYR14][TFSI] is known for its wide voltage window (~5–6V) and its moderate conductivity (~2 mS cm^{-1})[29] while the sodium salt was chosen for its stable cycling behavior and role in the formation of a dense solid electrolyte interphase (SEI).[30–32] The components utilized in the ionogel synthesis are depicted in Figure 2.2a.

In this one-pot, liquid-phase synthesis (Figure 2.2b), we utilize an ethylene oxide-modified PDMS (m-PDMS) to ensure miscibility with the ionic liquid. Both silica precursors (MTMS and m-PDMS) mix with formic acid to begin hydrolysis followed by condensation reactions. After the sol-gel reaction has begun, but before gelation has occurred, ionic liquid is added to the precursor solution which, after mixing, is cast into a propylene mound. After several drying steps to evaporate water and methanol produced from the synthesis, a monolithic ionogel electrolyte of typical area of 2 cm^2 and thickness of 400 µm is removed from the polypropylene mound.

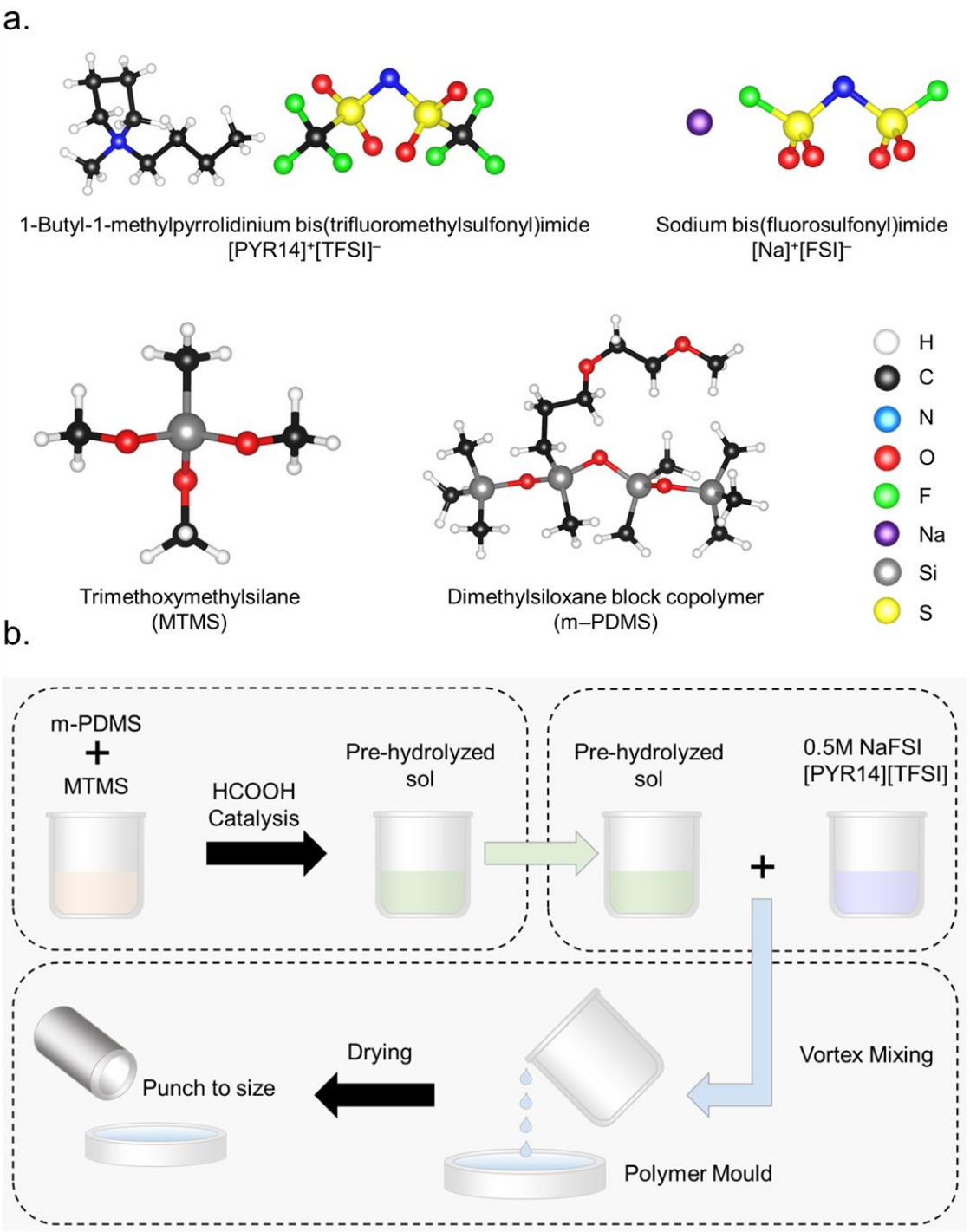

Figure 2.2. **a.** Components (ionic liquid, sodium salt, and silica structure precursors) and **b.** synthesis schematic for the ionogel electrolyte.

The ternary phase diagram (Figure 2.3.) shows how ionogel stability is affected by composition. This phase diagram is comprised of the volume fractions of three components (m-PDMS, MTMS, and PYR14 TFSI) while the volume of formic acid was held constant. All samples were aged and dried in the same manner. Ideally, the largest ratio of ionic liquid would produce an ionogel with the best electrochemical performance because its composition is closest to that of the ionic liquid electrolyte. However, without sufficient solid content, the ionogel will not gel into a monolith. The balance between m-PDMS and MTMS is also important; m-PDMS alone will not produce monoliths and MTMS alone leads to the formation of brittle ionogels. Mixtures with the incorrect ratio of the two silica precursors result in ionogels with low conductivity (below 0.1 mS cm^{-1}) or those which are noted as 'Fragile' in Figure 2.3. These ionogels are either too brittle or too soft and tend to produce short circuits during cell fabrication or testing. All subsequent experiments described in this study pertain to the 'Ideal' composition range in Figure 2.3 whose composition was based on the volume ratio of MTMS:m-PDMS:ILE of 1.8:2:1.

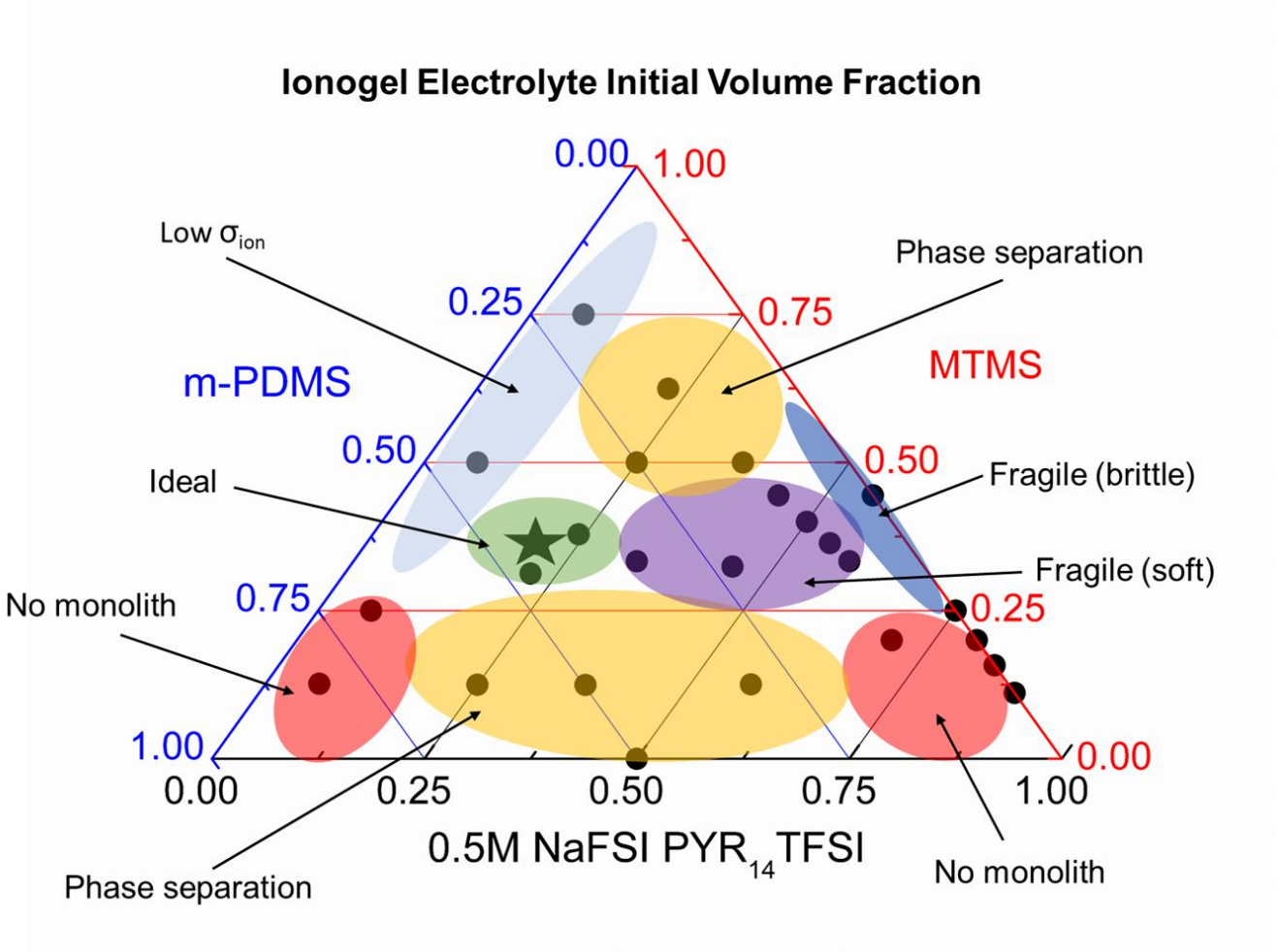

Figure 2.3. Ternary phase diagram for ionogel electrolyte synthesis. Values are from the initial volume fraction of each component. In these experiments, formic acid was kept at a constant volume. Regions of phase separation (yellow) are those in which some gelation occurred, but was separated from the ionic liquid. "No monolith" regions (red) showed no indication of gelation in the time of the experiment. The cutoff from low ionic conductivity (light blue) was 0.1 mS cm^{-1} and the cutoff for "too soft" (purple) was 1 MPa. Brittle samples (dark blue) fractured immediately upon cell construction. The ★ sample was utilized for subsequent testing in this manuscript.

Thermogravimetric analysis (TGA) shows the evolution of the weight change upon heating (Figure 2.4a). There is no weight loss below 100°C, indicating minimal adsorbed moisture due to the hydrophobicity. The ionogels are thermally stable up to 150°C at which point the NaFSI salt begins degradation.[33] Subsequent weight loss is from a combination of the decomposition of m-PDMS (boiling point ~200 °C), [PYR14][TFSI] (degradation temperature 400 °C), and removal of the methyl groups from the silica surface (continuously from 300-700 °C).[26,33–38] At temperatures above 500°C, the remaining weight pertains to primarily to silica from the MTMS. Based on these data, we estimate the ionic liquid electrolyte content of the MTMS:m-PDMS:ILE 1.8:2:1 ionogel to be between 50–55 wt% after all drying steps were completed. This was confirmed by measuring the remaining scaffold weight after removal of the ionic liquid electrolyte with acetone. Nanoindentation on ionogel samples reveals an elastic modulus of 13±5 MPa for our optimized sample which compares well with other gel electrolytes in literature (Figure 2.5.). X-ray diffraction (XRD) of the ionogel (Figure 2.4b) displays two broad peaks at 12.5° and 21° corresponding to a combination of the ionic liquid and amorphous silica.[39] Fourier-transform infrared spectroscopy (FTIR) measurements of the ionogel (Figure 2.4c) exhibit peaks corresponding to the ionic liquid superimposed with those from Si-O-Si and Si-CH_3.[40] Taken together, the TGA, XRD, and FTIR results confirm the presence of only ionic liquid and organically-modified silica in the final sample.

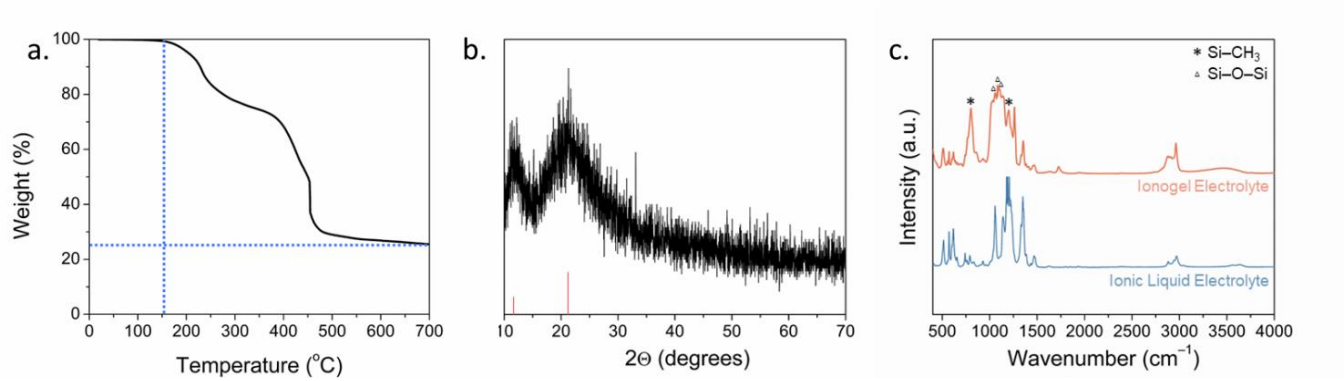

Figure 2.4. a. Thermogravimetric analysis **b.** X-ray diffraction and **c.** Fourier-transform infrared spectroscopy of the ionogel electrolyte.

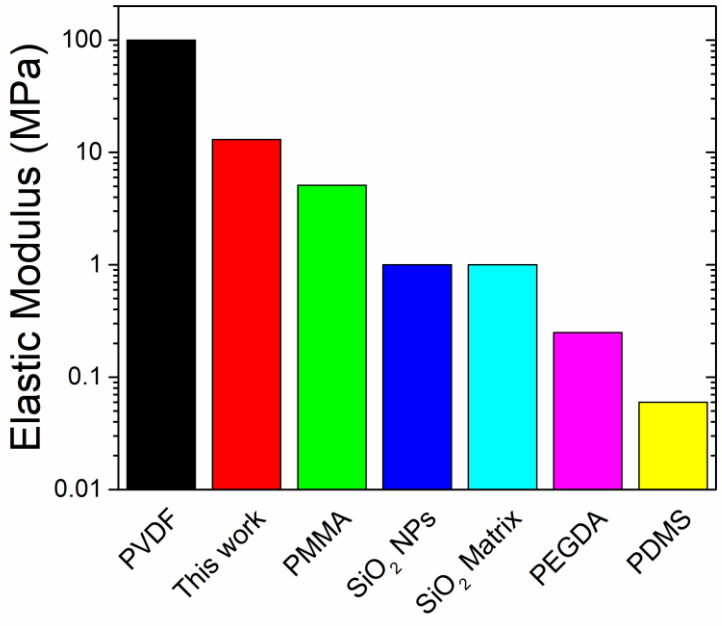

Figure 2.5. Elastic moduli for gel electrolytes with various supporting matrices. PVDF: poly(vinylidene fluoride)[41], PMMA: poly(methyl methacrylate)[42], SiO_2 NPs: silica nanoparticles[11], SiO_2 Matrix: sol-gel-derived silica[43], PEGDA: poly(ethylene glycol) diacrylate[16], PDMS: poly(dimethylsiloxane).[27]

Structurally, the ionogels display flat surfaces covered with droplets of ionic liquid, (Figure 2.6a,b). To determine the morphology of the mesoporous silica scaffold, gas adsorption measurements were made on materials in which the ionic liquid electrolyte was removed by a 2-step process.[20] First, the ILE was solvent exchanged with acetone. This solvent was then removed by supercritical drying in CO_2 which suppresses capillary pressure during drying and preserves the mesoporous SiO_2 structure by preventing pore collapse.[44] The measurements were made on samples with an equimolar amount of MTMS replacing the m–PDMS which prevented pore collapse on the softer structure. The isotherm and pore-size distribution (Figure 2.7.) reveal an open structure with a surface area of 884 $m^2\ g^{-1}$ and an average pore size of 13

nm. Although there will be differences in the pore architecture upon addition of m–PDMS, this measurement provides a general idea of the pore architecture.

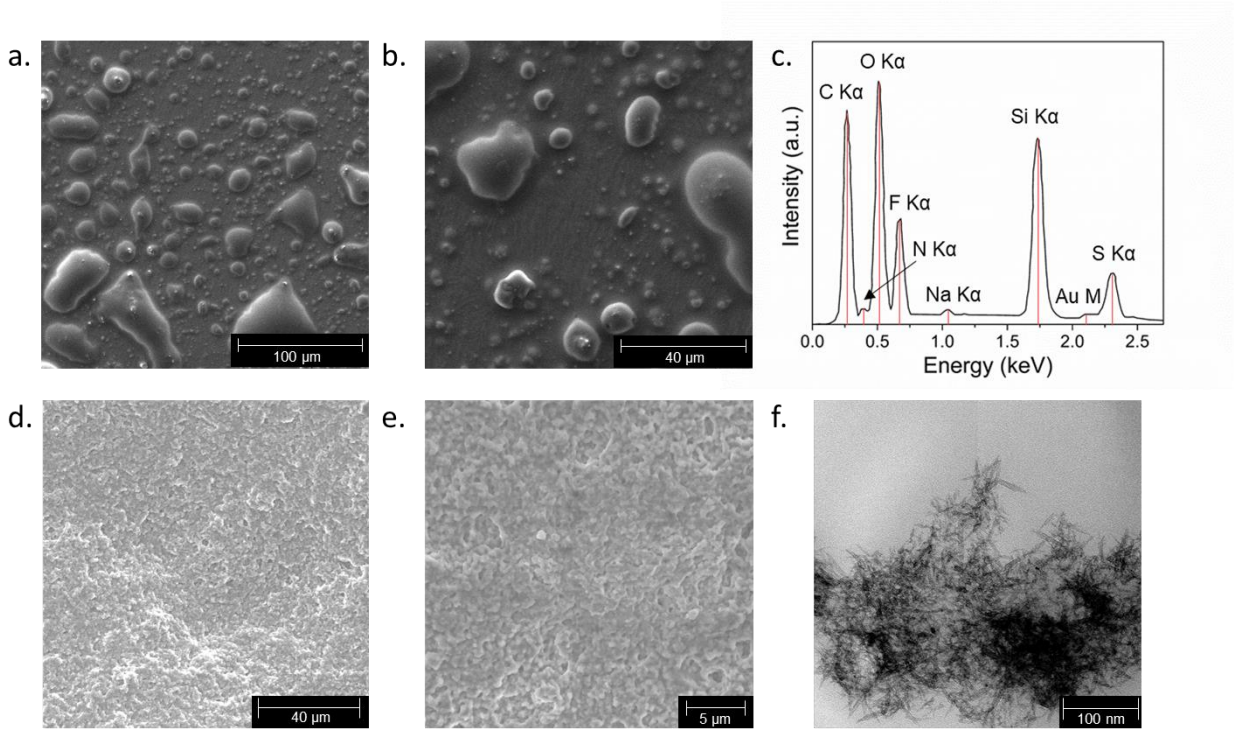

Figure 2.6. a,b. Scanning electron micrographs and c. a representative energy dispersive spectroscopy scan of the ionogel electrolyte before ionic liquid extraction. **d,e.** scanning electron micrographs and **f.** transmission electron micrograph of the ionogel electrolyte after ionic liquid extraction.

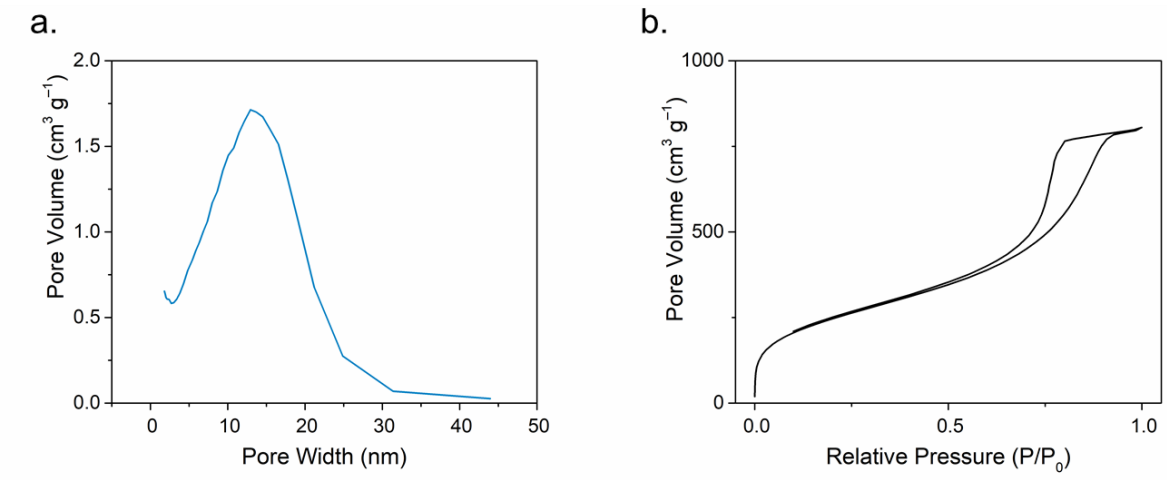

Figure 2.7. a. Nitrogen adsorption isotherm and **b.** the pore-size distribution for an ionogel with no m–PDMS (replaced with equimolar MTMS).

Electrochemical stability and cycling

We conducted a series of transport and electrochemical measurements to assess the suitability of using the ionogel in SIBs. All electrochemical experiments performed with ionogel electrolyte utilized the MTMS:m-PDMS:ILE 1.8:2:1 composition. Electrochemical impedance spectroscopy (EIS) is used to reveal the transport behavior of the ionogel electrolyte as a function of temperature as shown in Figure 2.8a. The room temperature ionic conductivity of 0.7 mS cm^{-1} is somewhat less than that of the ILE (2 mS cm^{-1}), but higher than most SIB solid electrolytes.[45] The temperature dependence of the conductivity exhibits an Arrhenius relationship for both the ILE and the ionogel electrolyte over the temperature range 20°C to 100°C. (Figure 2.8b). The ionogel electrolyte exhibits an activation energy of 0.3 eV which is on the same order as that of the ILE (0.2 eV) as well as other solid electrolytes such as $Na_{11}Sn_2PS_{12}$, Na_3SbS_4, and $Na_3Zr_2Si_2PO_{12}$.[46–48]

One significant advantage of ionogel electrolytes is their large electrochemical stability window (ESW). To assess the ESW for our system, we utilize linear sweep voltammetry (LSV) with blocking electrodes (Figure 2.8c). The positive sweep and negative sweep were performed on different samples to prevent influence from degradative species. Using a silver wire quasi-reference, the ionogel electrolyte demonstrates a stability window of nearly 5V with a conservative current cut-off of 10 μA cm^{-2}. This value correlates well with the window for [PYR14][TFSI] in the literature[49,50] and suggests that this solid electrolyte system may be compatible with high-voltage cathodes.

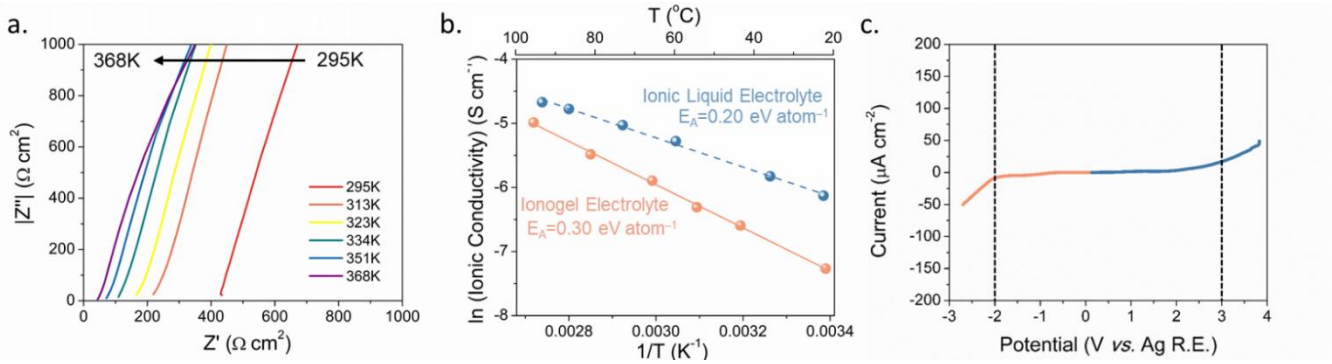

Figure 2.8. a. Electrochemical impedance spectroscopy as a function of temperature for the ionogel electrolyte **b.** Ionic conductivity–inverse temperature plot and extracted activation energy **c.** Linear sweep voltammetry to assess the electrochemical stability window of the ionogel electrolyte. Two separate samples were used for the forward and reverse scan.

Electrochemical stability and reversibility with electrode materials are important considerations for novel SIB electrolytes. To assess these properties, we pair our ionogel electrolyte with sodium vanadium phosphate (NVP), a prototypical sodium-ion battery cathode. NVP possesses the NASICON crystal structure, leading to a high sodium-ion diffusivity as well as a distinct redox couple upon sodiation/desodiation at 3.4 V vs $Na|Na^{+}$.[51] In addition to these

desirable traits, NVP has also been successfully demonstrated as a cathode in ionic liquid electrolytes[52,53] making it an ideal cathode for evaluating our ionogel electrolyte. Although NVP suffers from a low electronic conductivity, this is often ameliorated by hybridization with various carbon materials.[51] In the current work, we used a published method[23] to synthesize NVP with glucose-derived, pyrolyzed carbon to enhance conductivity.

When paired with our ionogel electrolyte and a sodium metal counter electrode, the NVP cathode displays broad, polarized redox peaks at a slow sweep rate of 0.1 mV s^{-1} (Figure 2.9a). As a control, we replace the ionogel with a common 1M $NaPF_6$ diglyme electrolyte[54] which exhibits sharp redox peaks with minimal peak separation at the same sweep rate. Upon disassembly of the coin cell with ionogel electrolyte, we observed significant discoloration on the sodium metal electrode, indicating that the sodium metal was unstable in contact with the ionogel electrolyte.

In order to investigate ionogel-electrode stability, we construct three cells with different combinations of sodium metal and NVP electrodes separated by ionogel electrolyte: Na|IG|Na, NVP|IG|Na, and NVP|IG|NVP. EIS of these cells (Figure 2.9b) reveals that devices with sodium metal electrodes (Na|IG|Na and NVP|IG|Na) exhibit significantly larger resistance than a symmetric NVP cell. In fact, the total resistance of the symmetric sodium cell was more than two orders of magnitude higher than that of the symmetric NVP cell. These data indicate that the Na|ionogel interface is highly resistive and impedes limits interfacial transport.

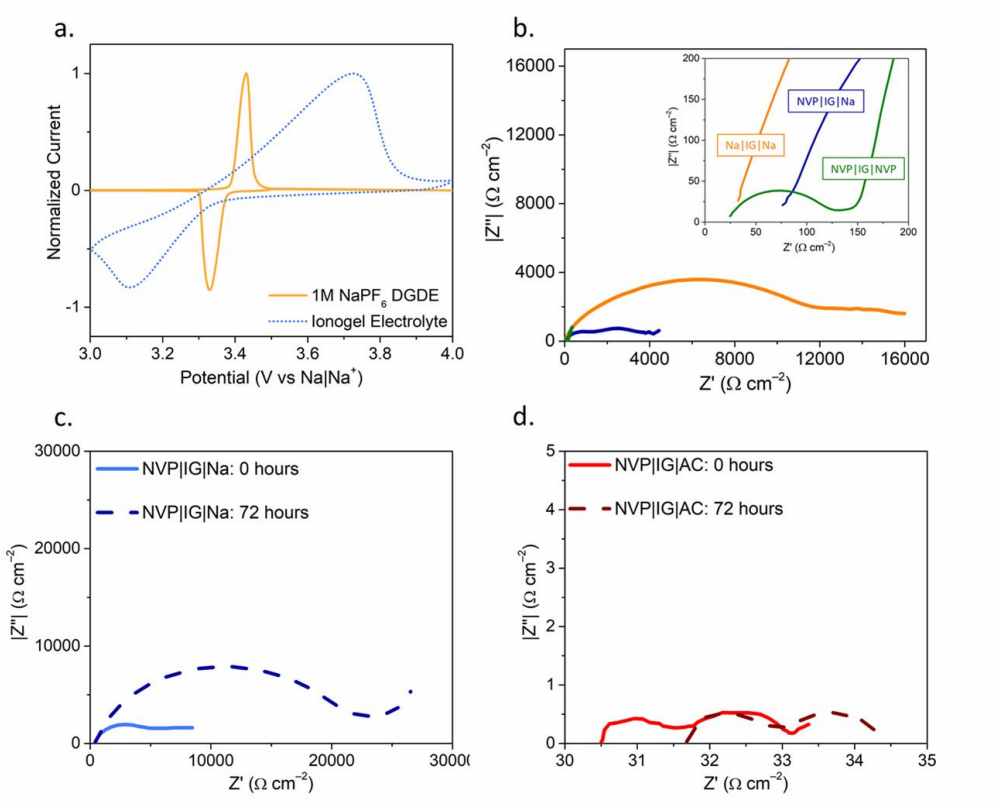

Figure 2.9. a. Cyclic voltammetry (0.1 mV s^{-1}) for an NVP cathode against sodium metal demonstrates severe polarization for the ionogel electrolyte. A control test in 1M $NaPF_6$ diglyme is included as a comparison at the same sweep rate. Current is normalized to peak current for proper comparison. **b.** EIS spectrum for 3 cells: Na|IG|Na, NVP|IG|Na, and NVP|IG|NVP. Inset shows the low resistance of the NVP|IG|NVP cell (green). EIS spectra for **c.** the traditional half-cell (NVP|IG|Na) and **d.** the modified half-cell (NVP|IG|AC) immediately after and 72 hours after construction.

In typical laboratory-scale battery testing, both galvanostatic discharge and cyclic voltammetry tests utilize the “half-cell” format to assess electrochemical performance. In this arrangement, the working electrode is the material under investigation with a counter/reference electrode of sodium metal (for SIBs) serving as an infinite source of sodium ions and a stable

reference potential. One critical assumption in this testing method is that sodium metal is either stable or quickly passivated in the electrolyte. Unfortunately, sodium metal is not stable in contact with most electrolytes and thus the suitability of half-cell testing has been called into question in recent literature.[55–57]

An alternative approach is to use an activated carbon (AC) electrode in place of the sodium metal to mitigate stability issues with sodium metal. Here, carbon stores charge capacitively at its surface and does not undergo faradaic reactions. This approach has been used in literature to more accurately test the electrochemical properties of sodium-ion electrodes.[58,59] In fact, Vogl et al. demonstrated reversible cycling of NVP cathode and AC anode in ionic liquid using this approach.[60] The resulting configuration resembles a sodium-ion capacitor (SIC) where one electrode stores charge faradaically (NVP) and the other stores charge capacitively (activated carbon). The capacitive charge storage of the carbon is considerably more reversible than the faradaic reaction of the NVP and effectively isolates the performance of the cell to that of the cathode material.

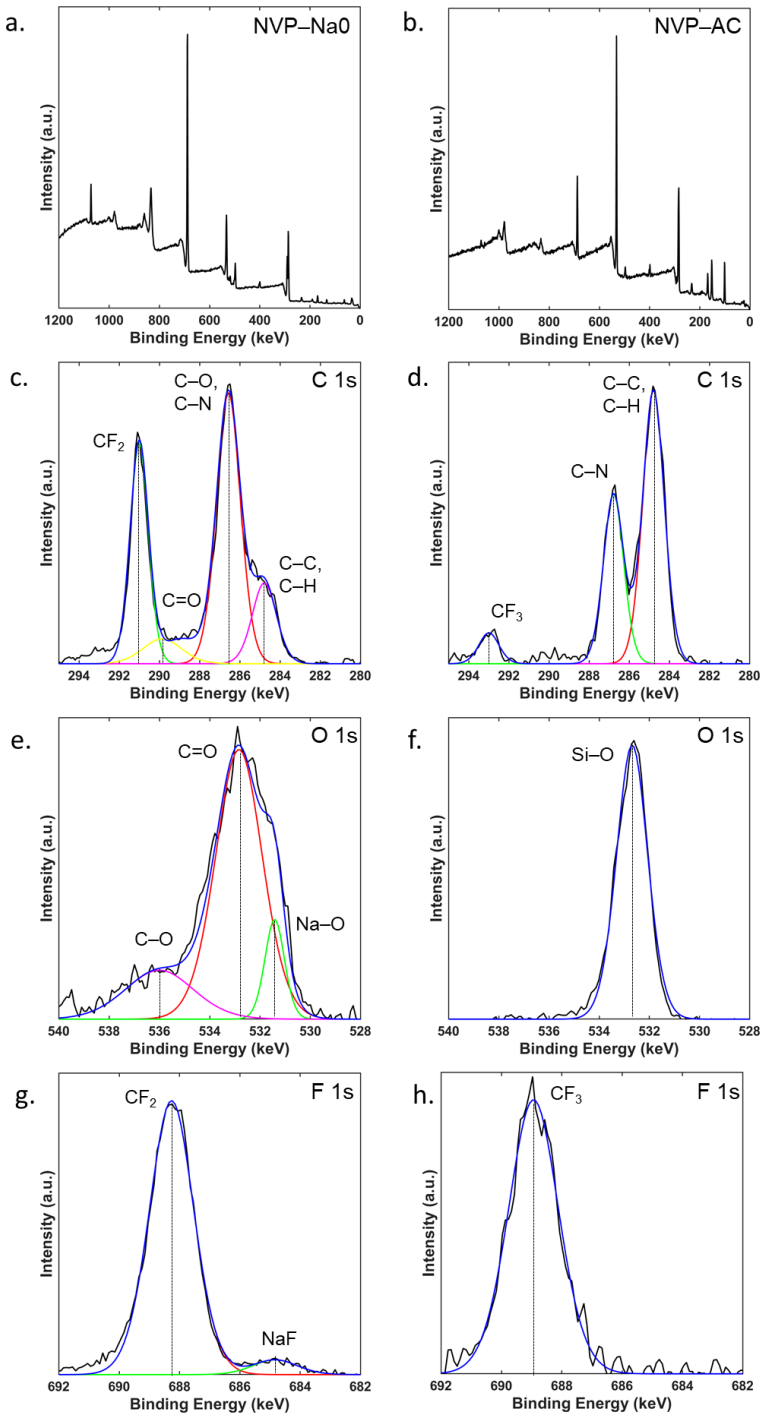

Figure 2.10. XPS for **a,c,e,g.** the NVP|IG|Na sample and **b,d,f,h**. the NVP|IG|AC sample after 72 hours exposure to electrolyte. **a,b.** Survey scans, **c,d.** C 1s **e,f.** O 1s and **g,h.** F 1s scans.

Table 2.1: Elemental composition of the NVP cathode surface after 72 hours exposure to ionogel electrolyte.

Element	NVP|IG|Na	NVP|IG|AC
Carbon	55.38%	44.93%
Oxygen	12.52%	23.53%
Fluorine	24.44%	5.67%
Sodium	1.89%	0.26%
Nitrogen	1.92%	2.14%
Sulfur	1.88%	6.56%
Phosphorus	1.63%	–
Silicon	–	16.92%
Vanadium	0.35%	–

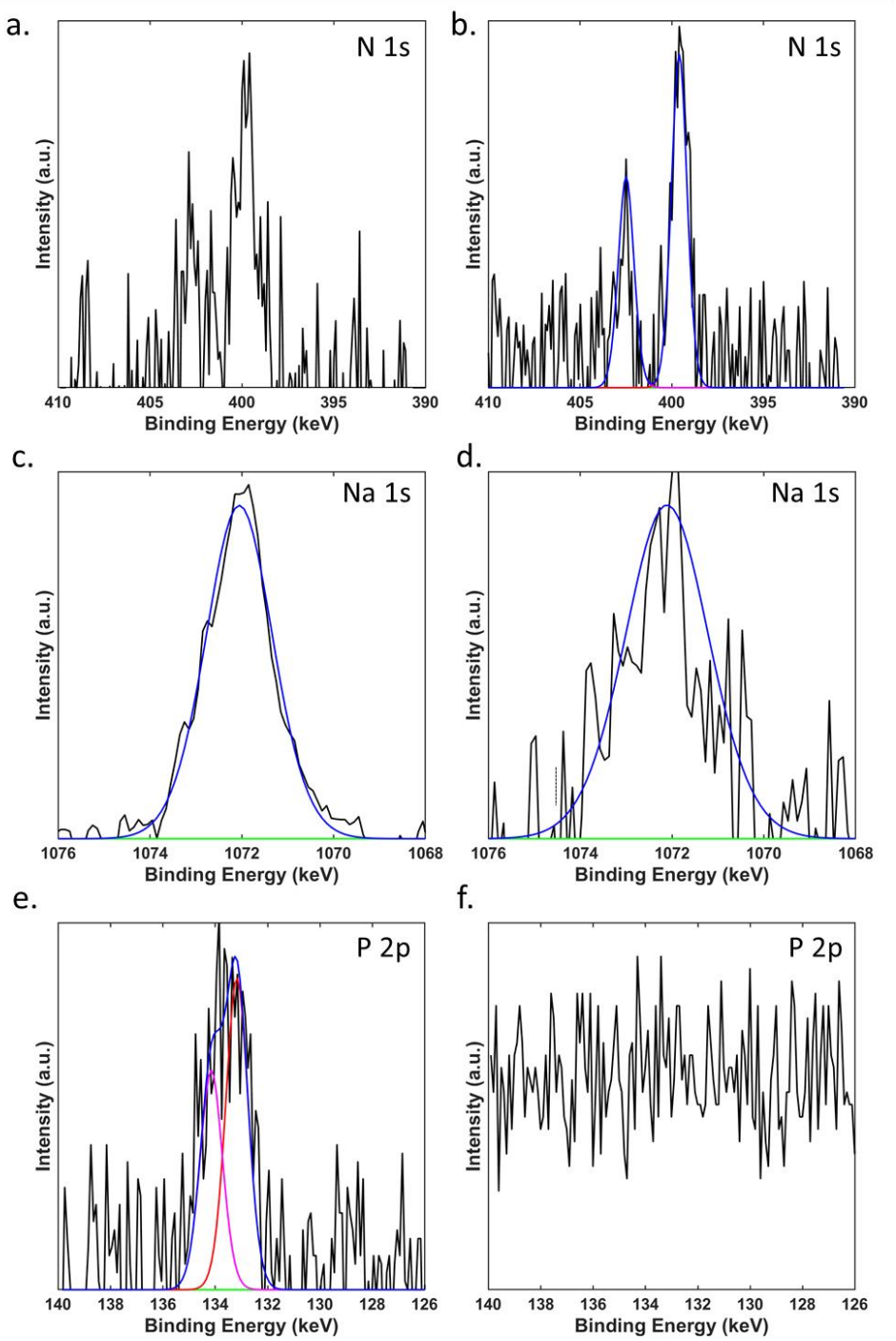

Figure 2.11. XPS (N 1s, Na 1s, P 2p) spectra for **a,c,e.** the NVP|IG|Na cell and **b,d,f.** the NVP|IG|AC cell.

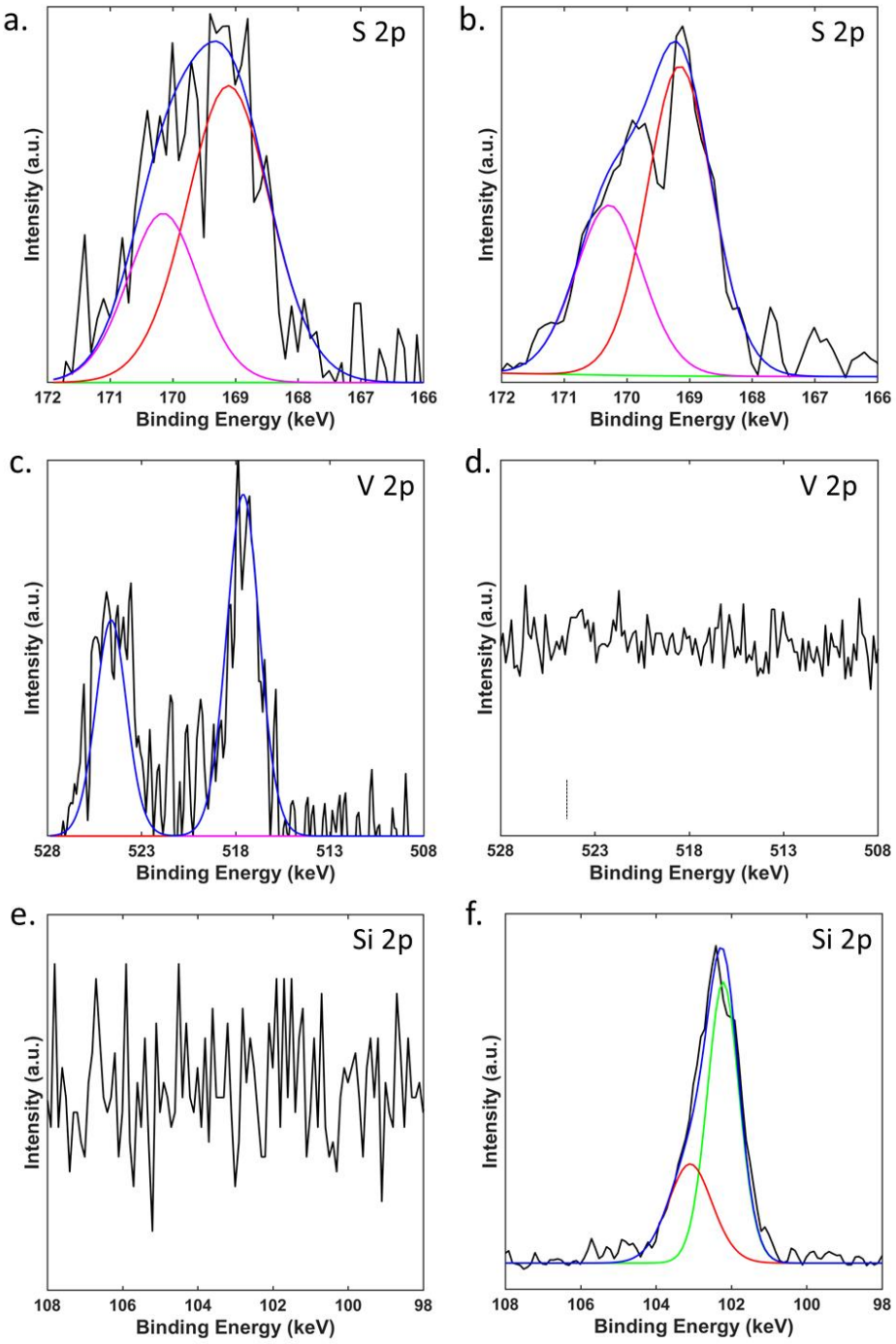

Figure 2.12. XPS (S 2p, V 2p, Si 2p) spectra for **a,c,e.** the NVP|IG|Na0 cell and **b,d,f.** the NVP|IG|AC cell.

To compare the ionogel interface of sodium metal and activated carbon, we evaluate two cells using EIS: (NVP|IG|Na) and (NVP|IG|AC). Measurements occurred immediately after and 72 hours after construction without cycling. The spectra in Figure 2.9c,d indicate drastically different impedance responses. The NVP|IG|AC cell displays a negligible impedance gain over three days (from 33 Ω to 34.5 Ω total resistance) whereas the NVP|IG|Na cell increases from 7000 Ω to 25000 Ω total resistance. In addition, the semi-circular arcs for NVP|IG|Na are severely depressed indicating the presence of a resistive, interfacial layer.[55,61,62] The dramatic difference in impedance emerges as a consequence of significant electrolyte breakdown.

To investigate this mechanism, we probe the surface of the NVP electrodes with X-ray photoelectron spectroscopy (XPS) 72 hours after cell construction. Figures 2.10.–2.12. and Table 2.1 summarize the XPS data and reveal that ionogel contact with sodium metal caused breakdown of fluorine-containing components, ($TFSI^-$, FSI^-). All bonds from the NVP–AC sample correspond to components of the ionic liquid (PYR14 TFSI), sodium salt (NaFSI), or the organosilica structure.[63–65] In contrast, the NVP|IG|Na sample exhibits additional peaks corresponding to degradation products. The C 1s scans depict C=O and C–O bonds, likely attributable to Na_2CO_3 and/or various organic species. This is corroborated by the presence of various carbon–oxygen bonds in the O1s spectrum for NVP|IG|Na. The most revealing spectra are the F 1s. The NVP|IG|AC surface contains only CF_3 bonds (from the $TFSI^-$) whereas NVP|IG|Na has peaks for both CF_2 (from the PVDF binder) and NaF. As there are no free F^- in solution, the fluorine must come from breakdown of either the $TFSI^-$ or FSI^-. The components found on the surface of the NVP|IG|Na sample resemble those found in the SEI (solid electrolyte interphase) and CEI (cathode electrolyte interphase) of similar cells,[35,52,63,64,66] but our cells have not been electrochemically cycled. The existence of NaF is also consistent with the effect of TFSI-based liquids on sodium metal.[30]

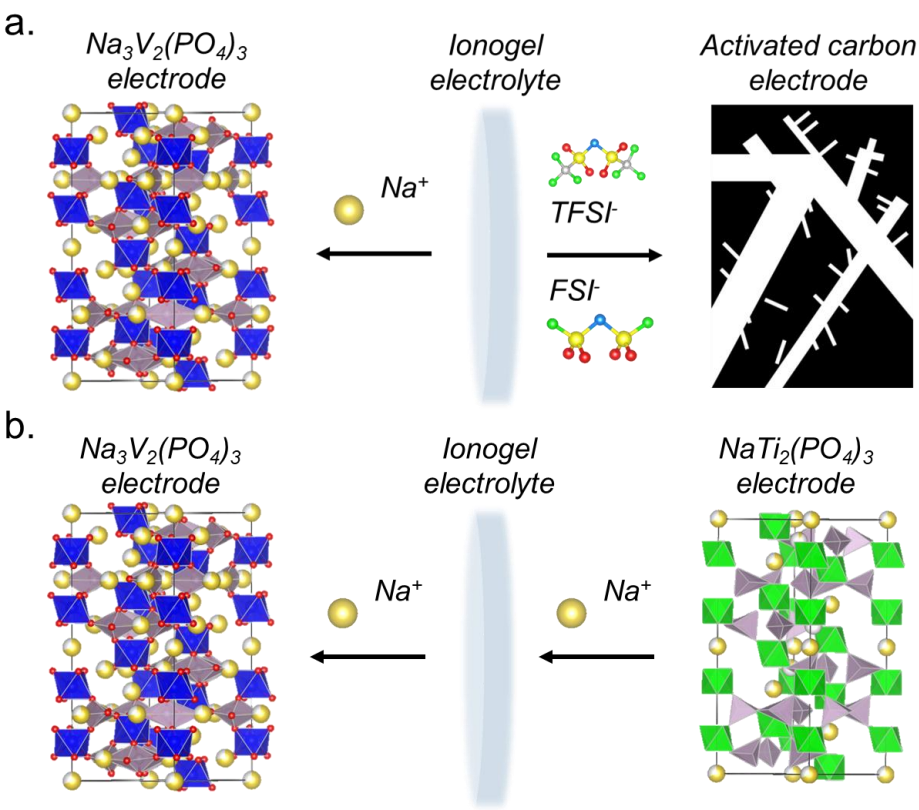

Figure 2.13. Schematic representation of the **a.** NVP|IG|AC half-cell and **b.** the NVP|IG|NTP full-cell devices.

Based on the above results, we characterized the electrochemical stability and reversibility using the NVP|IG|AC cell; a schematic of the cell is shown in the Figure 2.13a. Galvanostatic charge-discharge experiments at a rate of 0.25C (30 mA g^{-1}) were used to assess electrochemical cycling with the ionogel electrolyte. The activated carbon electrode possessed about 10x the capacity and 3x the area of the NVP electrode so that the performance of the cathode could be isolated. As seen in Figure 2.14a, the shape of the discharge curves changes only slightly between cycle 1 and cycle 50. No significant capacity fade occurred over 50 cycles and the Coulombic efficiency after the first 10 cycles remained above 98% (Figure 2.14b). The rate retention of the NVP|IG|AC cell is shown in Figure 2.14c. Near theoretical capacity is achieved at

both rates of 0.1C and 0.25C. At rates below 1C the NVP retains a discharge capacity above 100 mAh g^{-1} which is comparable to other ionic liquid and ionogel electrolytes with both sodium metal[19,52,53,67] and activated carbon[60] counter electrodes. At high rates above 1C, the NVP|IG|AC cell delivers increasingly less charge due to the low ionic conductivity of the electrolyte. As demonstrated in literature, however, the rate retention could be significantly improved by elevating the temperature of the cell which is possible due to the thermal stability of the ionic liquid.[43,60]

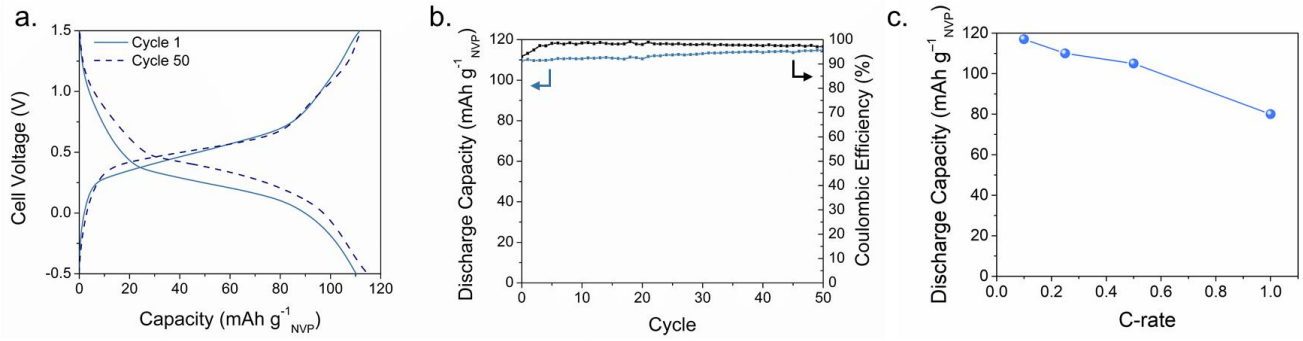

Figure 2.14. **a.** Galvanostatic charge/discharge curves for a rate of 0.25C and **b.** corresponding capacity and Coulombic efficiency for the NVP|IG|AC cell. **c.** Discharge capacity of the NVP|IG|AC cell as a function of C-rate.

To demonstrate a full sodium-ion battery, we pair the NVP cathode with sodium titanium phosphate (NTP) anode and ionogel electrolyte. The results for cycling at a rate of 0.25C are shown in Figure 2.15 and a schematic of this cell is shown in Figure 2.13b. In this cell, the NTP was overloaded by ~10% so that the charge and discharge capacity could be attributed to the NVP alone. The first cycle shows excess capacity associated with structural rearrangement and/or dissolution which is common in NTP electrodes.[68–70] Thereafter, the full-cell device stabilizes to ~85% of its theoretical capacity and exhibits only ~ 10% capacity loss with a Coulombic efficiency of 99% (Figure 2.15b) over 100 cycles. In comparison to another solid-state,

sodium-ion full-cell devices, our ionogel electrolyte demonstrates better capacity and cycling stability. A symmetrical NVP cell with $Na_3Zr_2Si_2PO_{12}$ solid electrolyte only reported 20 mAh g^{-1} at an areal current density of 10 µA cm^{-2} (compared to our 40 µA cm^{-2}).[71] Even when comparing to nonflammable liquid electrolyte, a similar NVP|NTP cell with trimethyl phosphate liquid electrolyte reported a comparable 100 mAh g^{-1} at rate of 0.2C.[69] To the best of our knowledge, this is the first demonstration of a full-cell, sodium-ion device utilizing an ionogel electrolyte. These results establish that Na^+ conducting ionogel electrolyte is a promising nonflammable, solid-state electrolyte for sodium-ion batteries.

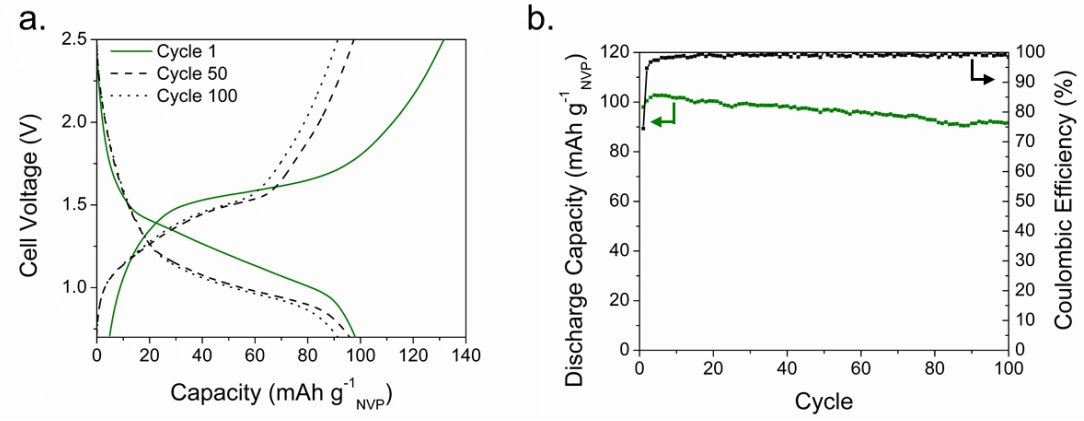

Figure 2.15. a. Galvanostatic charge/discharge curves at a rate of 0.25C and **b.** the corresponding capacity and Coulombic efficiency for the NVP|IG|NTP full-cell device.

2.4. Conclusions

In this work, an ionogel electrolyte (IG) was synthesized through the encapsulation of an ionic liquid within an organically-modified silica matrix. This synthesis approach leads to a pseudosolid electrolyte with a high ionic conductivity (0.7 mS cm^{-1}) a 5V electrochemical stability window and thermal stability up to 150°C. Interfacial reaction with sodium metal was identified as a dominating factor in half cell experiments. The problem was overcome by replacing the sodium metal electrode with an activated carbon electrode. Half-cell experiments with NVP cathode exhibited excellent reversibility and good capacity at rates up to 0.5C. A solid-state sodium ion battery comprised based on the ionogel electrolyte with an NVP cathode and an NTP anode demonstrated appropriate capacity and excellent cycling with only a slight capacity loss over 100 cycles. These results show the promise of ionogels serving as a nonflammable, pseudosolid electrolyte for sodium ion batteries.

2.5. References

1. Dunn, B., Kamath, H. & Tarascon, J.-M. Electrical Energy Storage for the Grid: A Battery of Choices. *Science* **334**, 928–935 (2011).
2. Choudhary, A. & Prasad, E. Lithium-ion Battery Market by Component (Cathode, Anode, Electrolytic Solution, and Others), End-use Industry [Electrical & Electronics (Smartphones &Tablet/PC, UPS, and Others) and Automotive (Cars, Buses, &Trucks; Scooters & Bikes;and Trains & Aircraft), and Industrial (Cranes & Forklift, Mining Equipment, and Smart Grid & Renewable Energy Storage): Global Opportunity Analysis and Industry Forecast, 2019–2027. *Allied Market Research* (2020).
3. Vaalma, C., Buchholz, D., Weil, M. & Passerini, S. A cost and resource analysis of sodium-ion batteries. *Nature Reviews Materials* **3**, 18013 (2018).
4. Palomares, V. *et al.* Na-ion batteries, recent advances and present challenges to become low cost energy storage systems. *Energy Environ. Sci.* **5**, 5884 (2012).
5. Nithya, C. & Gopukumar, S. Sodium ion batteries: a newer electrochemical storage: Sodium ion batteries. *WIREs Energy Environ* **4**, 253–278 (2015).
6. Kalhoff, J., Eshetu, G. G., Bresser, D. & Passerini, S. Safer Electrolytes for Lithium-Ion Batteries: State of the Art and Perspectives. *ChemSusChem* **8**, 2154–2175 (2015).
7. Watanabe, M. *et al.* Application of Ionic Liquids to Energy Storage and Conversion Materials and Devices. *Chem. Rev.* **117**, 7190–7239 (2017).
8. *Electrochemical Aspects of Ionic Liquids: Ohno/Electrochemical Aspects of Ionic Liquids*. (John Wiley & Sons, Inc., 2005). doi:10.1002/0471762512.
9. Galiński, M., Lewandowski, A. & Stępniak, I. Ionic liquids as electrolytes. *Electrochimica Acta* **51**, 5567–5580 (2006).
10. Chen, N., Zhang, H., Li, L., Chen, R. & Guo, S. Ionogel Electrolytes for High-Performance Lithium Batteries: A Review. *Adv. Energy Mater.* **8**, 1702675 (2018).

11. Ueno, K., Hata, K., Katakabe, T., Kondoh, M. & Watanabe, M. Nanocomposite Ion Gels Based on Silica Nanoparticles and an Ionic Liquid: Ionic Transport, Viscoelastic Properties, and Microstructure. *J. Phys. Chem. B* **112**, 9013–9019 (2008).
12. Caimi, S., Wu, H. & Morbidelli, M. PVdF-HFP and Ionic-Liquid-Based, Freestanding Thin Separator for Lithium-Ion Batteries. *ACS Applied Energy Materials* (2018) doi:10.1021/acsaem.8b00860.
13. Singh, V. K., Shalu, S., Chaurasia, S. K. & Singh, R. K. Development of ionic liquid mediated novel polymer electrolyte membranes for application in Na-ion batteries. *RSC Adv.* **6**, 40199–40210 (2016).
14. Rani, M. A. A., Hwang, J., Matsumoto, K. & Hagiwara, R. Poly(vinyl chloride) Ionic Liquid Polymer Electrolyte Based on Bis(fluorosulfonyl)Amide for Sodium Secondary Batteries. *J. Electrochem. Soc.* **164**, H5031–H5035 (2017).
15. Mohd Noor, S. A., Yoon, H., Forsyth, M. & MacFarlane, D. R. Gelled ionic liquid sodium ion conductors for sodium batteries. *Electrochimica Acta* **169**, 376–381 (2015).
16. Fdz De Anastro, A. *et al.* UV-Cross-Linked Ionogels for All-Solid-State Rechargeable Sodium Batteries. *ACS Appl. Energy Mater.* **2**, 6960–6966 (2019).
17. Kumar, D. & Hashmi, S. A. Ionic liquid based sodium ion conducting gel polymer electrolytes. *Solid State Ionics* **181**, 416–423 (2010).
18. Hashmi, S. A. *et al.* Ionic liquid-based sodium ion-conducting composite gel polymer electrolytes: effect of active and passive fillers. *J Solid State Electrochem* **20**, 2817–2826 (2016).
19. Mendes, T. C. *et al.* Supported Ionic Liquid Gel Membrane Electrolytes for a Safe and Flexible Sodium Metal Battery. *ACS Sustainable Chemistry & Engineering* (2019) doi:10.1021/acssuschemeng.8b06212.

20. Ashby, D. S., DeBlock, R. H., Lai, C.-H., Choi, C. S. & Dunn, B. S. Patternable, Solution-Processed Ionogels for Thin-Film Lithium-Ion Electrolytes. *Joule* **1**, 344–358 (2017).
21. Coltrain, B. K. & Kelts, L. W. The Chemistry of Hydrolysis and Condensation of Silica Sol—Gel Precursors. in *The Colloid Chemistry of Silica* (ed. Bergna, H. E.) vol. 234 403–418 (American Chemical Society, 1994).
22. Wang, S. *et al.* Comparative studies on electrochemical cycling behavior of two different silica-based ionogels. *Journal of Power Sources* **301**, 299–305 (2016).
23. Wan, X. *et al.* Carbon Nanolayer-Coated $Na_3V_2(PO_4)_3$ Nanocrystals Embedded in Conductive Carbon Matrix as High-Performance Cathode for Sodium-Ion Batteries. *ChemElectroChem* **5**, 2630–2635 (2018).
24. Munteshari, O., Lau, J., Krishnan, A., Dunn, B. & Pilon, L. Isothermal calorimeter for measurements of time-dependent heat generation rate in individual supercapacitor electrodes. *Journal of Power Sources* **374**, 257–268 (2018).
25. Müller, A., Wapler, M. C. & Wallrabe, U. A quick and accurate method to determine the Poisson's ratio and the coefficient of thermal expansion of PDMS. *Soft Matter* **15**, 779–784 (2019).
26. Venkateswara Rao, A., Bhagat, S. D., Hirashima, H. & Pajonk, G. M. Synthesis of flexible silica aerogels using methyltrimethoxysilane (MTMS) precursor. *Journal of Colloid and Interface Science* **300**, 279–285 (2006).
27. Horowitz, A. I. & Panzer, M. J. Poly(dimethylsiloxane)-Supported Ionogels with a High Ionic Liquid Loading. *Angew. Chem. Int. Ed.* **53**, 9780–9783 (2014).
28. Stein, M., Chen, C.-F., Robles, D. J., Rhodes, C. & Mukherjee, P. P. Non-aqueous Electrode Processing and Construction of Lithium-ion Coin Cells. *JoVE* 53490 (2016) doi:10.3791/53490.

29. Ong, S. P., Andreussi, O., Wu, Y., Marzari, N. & Ceder, G. Electrochemical Windows of Room-Temperature Ionic Liquids from Molecular Dynamics and Density Functional Theory Calculations. *Chem. Mater.* **23**, 2979–2986 (2011).
30. Hosokawa, T. *et al.* Stability of Ionic Liquids against Sodium Metal: A Comparative Study of 1-Ethyl-3-methylimidazolium Ionic Liquids with Bis(fluorosulfonyl)amide and Bis(trifluoromethylsulfonyl)amide. *The Journal of Physical Chemistry C* **120**, 9628–9636 (2016).
31. Zheng, J. *et al.* Extremely Stable Sodium Metal Batteries Enabled by Localized High-Concentration Electrolytes. *ACS Energy Letters* **3**, 315–321 (2018).
32. Kumar, H., Detsi, E., Abraham, D. P. & Shenoy, V. B. Fundamental Mechanisms of Solvent Decomposition Involved in Solid-Electrolyte Interphase Formation in Sodium Ion Batteries. *Chem. Mater.* **28**, 8930–8941 (2016).
33. Eshetu, G. G. *et al.* Comprehensive Insights into the Reactivity of Electrolytes Based on Sodium Ions. *ChemSusChem* **9**, 462–471 (2016).
34. Qi, X. *et al.* Sodium Bis(fluorosulfonyl)imide/Poly(ethylene oxide) Polymer Electrolytes for Sodium-Ion Batteries. *ChemElectroChem* **3**, 1741–1745 (2016).
35. Hilder, M. *et al.* Small quaternary alkyl phosphonium bis(fluorosulfonyl)imide ionic liquid electrolytes for sodium-ion batteries with P2- and O3-Na 2/3 [Fe 2/3 Mn 1/3]O 2 cathode material. *Journal of Power Sources* **349**, 45–51 (2017).
36. Liu, Y. R. One-pot route to synthesize ordered mesoporous polymer/silica and carbon/silica nanocomposites using poly(dimethylsiloxane)–poly(ethylene oxide) (PDMS–PEO) as co-template. *Microporous and Mesoporous Materials* **124**, 190–196 (2009).
37. Nádherná, M., Reiter, J., Moškon, J. & Dominko, R. Lithium bis(fluorosulfonyl)imide–PYR14TFSI ionic liquid electrolyte compatible with graphite. *Journal of Power Sources* **196**, 7700–7706 (2011).

38. Chagas, L. G., Jeong, S., Hasa, I. & Passerini, S. Ionic Liquid-Based Electrolytes for Sodium-Ion Batteries: Tuning Properties To Enhance the Electrochemical Performance of Manganese-Based Layered Oxide Cathode. *ACS Appl. Mater. Interfaces* **11**, 22278–22289 (2019).
39. Chinnam, P. R. *et al.* Multi-ionic lithium salts increase lithium ion transference numbers in ionic liquid gel separators. *J. Mater. Chem. A* **4**, 14380–14391 (2016).
40. Ul Haq, E. *et al.* Hydrophobic silica aerogel glass-fibre composite with higher strength and thermal insulation based on methyltrimethoxysilane (MTMS) precursor. *Energy and Buildings* **151**, 494–500 (2017).
41. Mejri, R. *et al.* Effect of ionic liquid anion and cation on the physico-chemical properties of poly(vinylidene fluoride)/ionic liquid blends. *European Polymer Journal* **71**, 304–313 (2015).
42. Ramesh, S., Winie, T. & Arof, A. K. Mechanical studies on poly(vinyl chloride)–poly(methyl methacrylate)-based polymer electrolytes. *J Mater Sci* **45**, 1280–1283 (2010).
43. Negre, L., Daffos, B., Turq, V., Taberna, P. L. & Simon, P. Ionogel-based solid-state supercapacitor operating over a wide range of temperature. *Electrochimica Acta* **206**, 490–495 (2016).
44. Rolison, D. R. & Dunn, B. Electrically conductive oxide aerogels: new materials in electrochemistry. *J. Mater. Chem.* **11**, 963–980 (2001).
45. Kim, J.-J., Yoon, K., Park, I. & Kang, K. Progress in the Development of Sodium-Ion Solid Electrolytes. *Small Methods* **1**, 1700219 (2017).
46. Banerjee, A. *et al.* Na_3SbS_4: A Solution Processable Sodium Superionic Conductor for All-Solid-State Sodium-Ion Batteries. *Angew. Chem. Int. Ed.* **55**, 9634–9638 (2016).
47. Zhang, Z. *et al.* $Na_{11}Sn_2PS_{12}$: a new solid state sodium superionic conductor. *Energy Environ. Sci.* **11**, 87–93 (2018).

48. Park, H., Jung, K., Nezafati, M., Kim, C.-S. & Kang, B. Sodium Ion Diffusion in Nasicon ($Na_3Zr_2Si_2PO_{12}$) Solid Electrolytes: Effects of Excess Sodium. *ACS Appl. Mater. Interfaces* **8**, 27814–27824 (2016).
49. Brutti, S. *et al.* Ionic liquid electrolytes for room temperature sodium battery systems. *Electrochimica Acta* **306**, 317–326 (2019).
50. Hasa, I., Passerini, S. & Hassoun, J. Characteristics of an ionic liquid electrolyte for sodium-ion batteries. *Journal of Power Sources* **303**, 203–207 (2016).
51. Zhang, X. *et al.* $Na_3V_2(PO_4)_3$: an advanced cathode for sodium-ion batteries. *Nanoscale* **11**, 2556–2576 (2019).
52. Manohar, C. V. *et al.* Stability enhancing ionic liquid hybrid electrolyte for NVP@C cathode based sodium batteries. *Sustainable Energy Fuels* **2**, 566–576 (2018).
53. Manohar, C. V. *et al.* Ionic liquid electrolytes supporting high energy density in sodium-ion batteries based on sodium vanadium phosphate composites. *Chem. Commun.* **54**, 3500–3503 (2018).
54. Seh, Z. W., Sun, J., Sun, Y. & Cui, Y. A Highly Reversible Room-Temperature Sodium Metal Anode. *ACS Central Science* **1**, 449–455 (2015).
55. Iermakova, D. I., Dugas, R., Palacín, M. R. & Ponrouch, A. On the Comparative Stability of Li and Na Metal Anode Interfaces in Conventional Alkyl Carbonate Electrolytes. *Journal of The Electrochemical Society* **162**, A7060–A7066 (2015).
56. Hwang, J., Takeuchi, K., Matsumoto, K. & Hagiwara, R. NASICON *vs.* Na metal: a new counter electrode to evaluate electrodes for Na secondary batteries. *J. Mater. Chem. A* **7**, 27057–27065 (2019).
57. Dugas, R., Forero-Saboya, J. D. & Ponrouch, A. Methods and Protocols for Reliable Electrochemical Testing in Post-Li Batteries (Na, K, Mg, and Ca). *Chem. Mater.* **31**, 8613–8628 (2019).

58. Pfeifer, K. *et al.* Can Metallic Sodium Electrodes Affect the Electrochemistry of Sodium-Ion Batteries? Reactivity Issues and Perspectives. *ChemSusChem* **12**, 3312–3319 (2019).
59. Lee, S. E. & Tang, M. H. Reliable Reference Electrodes for Nonaqueous Sodium-Ion Batteries. *J. Electrochem. Soc.* **166**, A3260–A3264 (2019).
60. Vogl, T. *et al.* The use of protic ionic liquids with cathodes for sodium-ion batteries. *J. Mater. Chem. A* **4**, 10472–10478 (2016).
61. Schranzhofer, H. *et al.* Electrochemical impedance spectroscopy study of the SEI formation on graphite and metal electrodes. *Journal of Power Sources* **153**, 391–395 (2006).
62. Zhang, S. Impedance study on the interface of poly electrolyte and metal sodium. *Solid State Ionics* **76**, 127–132 (1995).
63. Do, M. P. *et al.* Effect of Conducting Salts in Ionic Liquid Electrolytes for Enhanced Cyclability of Sodium-Ion Batteries. *ACS Appl. Mater. Interfaces* **11**, 23972–23981 (2019).
64. Do, M. P. *et al.* Investigation of the Electrochemical and Thermal Stability of an Ionic Liquid Based $Na_{0.6}Co_{0.1}Mn_{0.9}O_2$ /$Na_{2.55}V_6O_{16}$ Sodium-Ion Full-Cell. *J. Electrochem. Soc.* **166**, A944–A952 (2019).
65. Howlett, P. C., Brack, N., Hollenkamp, A. F., Forsyth, M. & MacFarlane, D. R. Characterization of the Lithium Surface in N-Methyl-N-alkylpyrrolidinium Bis(trifluoromethanesulfonyl)amide Room-Temperature Ionic Liquid Electrolytes. *J. Electrochem. Soc.* **153**, A595 (2006).
66. Lahiri, A., Olschewski, M., Gustus, R., Borisenko, N. & Endres, F. Surface modification of battery electrodes via electroless deposition with improved performance for Na-ion batteries. *Phys. Chem. Chem. Phys.* **18**, 14782–14786 (2016).
67. Hwang, J., Matsumoto, K. & Hagiwara, R. $Na_3V_2(PO_4)_3$@Carbon Nanofibers: High Mass Loading Electrode Approaching Practical Sodium Secondary Batteries Utilizing Ionic Liquid Electrolytes. *ACS Appl. Energy Mater.* **2**, 2818–2827 (2019).

68. Zhang, Q., Liao, C., Zhai, T. & Li, H. A High Rate 1.2V Aqueous Sodium-ion Battery Based on All NASICON Structured NaTi 2 (PO 4) 3 and Na 3 V 2 (PO 4) 3. *Electrochimica Acta* **196**, 470–478 (2016).
69. Jiang, X. *et al.* An All-Phosphate and Zero-Strain Sodium-Ion Battery Based on $Na_3V_2(PO_4)_3$ Cathode, $NaTi_2(PO_4)_3$ Anode, and Trimethyl Phosphate Electrolyte with Intrinsic Safety and Long Lifespan. *ACS Appl. Mater. Interfaces* **9**, 43733–43738 (2017).
70. Hung, T.-F. *et al.* Hydrothermal Synthesis of Sodium Titanium Phosphate Nanoparticles as Efficient Anode Materials for Aqueous Sodium-Ion Batteries. *ACS Sustainable Chem. Eng.* **4**, 7074–7079 (2016).
71. Noguchi, Y., Kobayashi, E., Plashnitsa, L. S., Okada, S. & Yamaki, J. Fabrication and performances of all solid-state symmetric sodium battery based on NASICON-related compounds. *Electrochimica Acta* **101**, 59–65 (2013).

Chapter 3: Nonflammable, pseudosolid electrolyte with ultralow overpotential for sodium-metal batteries

Solutions of sodium salt in glyme solvent are encapsulated within mesoporous silica matrices for fabrication of pseudosolid, sodium-ion electrolytes. Incorporation of a polymer matrix provides mechanical stability and allows for long-term cycle stability. We demonstrate incredibly low overpotentials for sodium metal plating/stripping and subsequently fabricate energy-dense, sodium-metal batteries with sodium vanadium fluorophosphate (NVOPF) cathode. The devices last over one hundred cycles and show no signs of degradation, even at high current densities.

3.1. Introduction and Background

On the basis of their low-cost and earth-abundant materials, sodium-ion batteries (SIBs) are viable options for next-generation energy storage, especially in the fields of grid storage, electric vehicles, and mobile-power delivery.[1–4] One subset of this technology which has received renewed attention is the sodium-metal battery (SMB).[5] Although similar to the sodium-ion battery, the major distinction in SMBs is the use of pure sodium metal as the low-potential electrode. Sodium metal possesses a high theoretical capacity (1165 mAh g^{-1}) and a low working voltage (0 V vs $Na|Na^{+}$), both of which can increase energy density substantially.[6–8] In fact, SMBs predate the modern lithium-ion battery by at least a decade with the advent of the sodium-sulfur and ZEBRA batteries.[9] In these devices, molten sodium metal anode is surrounded by a β-Al_2O_3 solid electrolyte and either a sulfur or $NiCl_2$ cathode, respectively. Compared to the standard lithium-ion battery anode, graphite, sodium metal has approximately 3x higher capacity, several orders of magnitude higher electronic conductivity, is over 10x cheaper, and has high natural abundance distributed homogenously on a global scale.[10,11]

When compared to common sodium-ion anode materials in Figure 3.1., sodium metal stands out as an ideal candidate for high energy-density batteries. Despite these tremendous characteristics, sodium metal is often considered impractical due to its reactivity and dangerous propensity for dendritic growth.

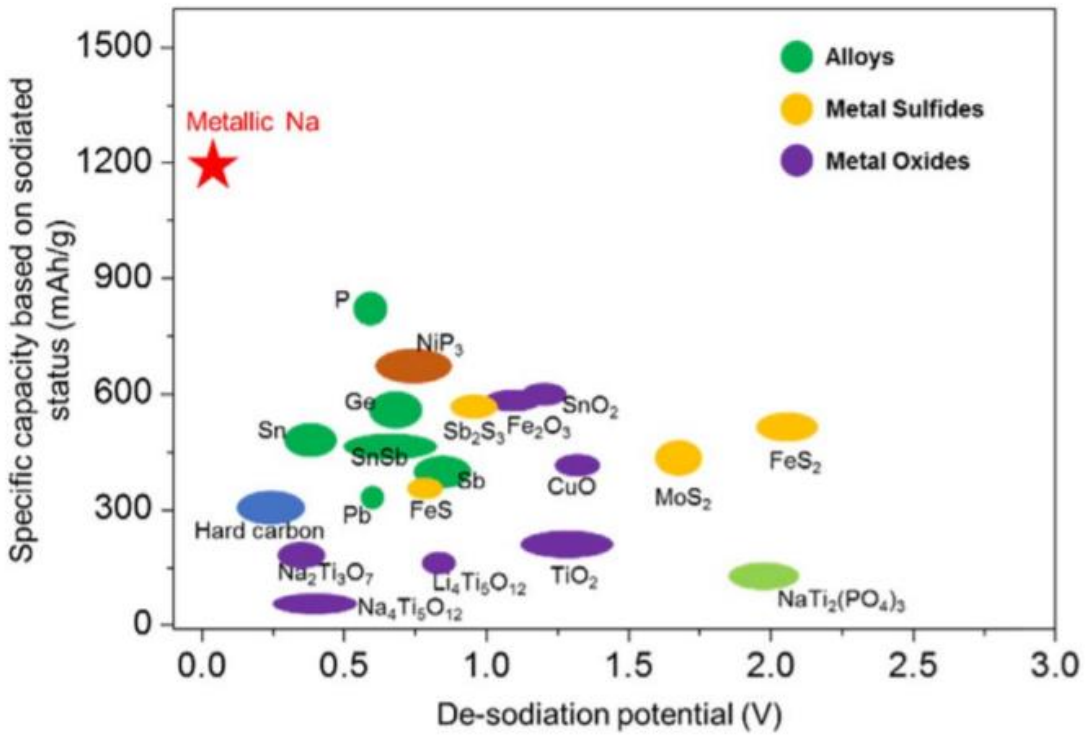

Figure 3.1. Comparison of the theoretical specific capacity and desodiation potential of various anode materials for sodium-ion batteries.[6]

Similar to its lithium metal counterpart, sodium metal experiences nonuniform deposition upon electrochemical plating. Typically, an unstable solid electrolyte interphase (SEI) is formed upon sodium plating which breaks upon repeated cycling. This process exposes fresh sodium metal to the electrolyte which begins the process again, but with an effectively smaller surface area.[12,13] This spatial inhomogeneity leads to local current density amplification which further

drives dendritic growth, leading to separator penetration and ultimately, device failure.[12,14] In contrast to lithium however, sodium metal exhibits instability with commonly-used, carbonate-based electrolytes. Many researchers have questioned the effectiveness of testing with sodium-metal electrodes in such solutions.[15–18] Heritage work on lithium-ion batteries was likely applied to sodium-ion systems without consideration for compatibility and has remained the standard since. As evident in Figure 3.2., sodium is much less reversible in galvanostatic plating/stripping experiments in carbonate electrolyte. Sodium plating/stripping experiments relveal significantly higher overpotentials, less uniform deposition, and a high likelihood to forming short circuits, resulting in a shorter cycle life.

Recently, glyme-based electrolytes, especially 1M $NaPF_6$ in diglyme, have shown outstanding stability in contact with sodium metal and are quickly becoming the new standard for electrode testing in sodium-ion batteries.[19–25] Glymes (or glycol methyl ethers) are hydrocarbon chains with alternating carbon, ether linkages, and end-capped with methyl groups. In contrast to the ionic liquids utilized in Chapter 2, glymes are relatively versatile solvents which are easily accessible, cheap, and used in a variety of common organic syntheses. Low molecular weight glymes (e.g. monoglyme, diglyme) have relatively high vapor pressures and are flammable. However, higher molecular weight glymes (tetraglyme, pentaglyme, and poly(ethylene glycol) dimethyl ether (PEGDME) are nonflammable and show markedly low vapor pressures and high flash points.[26]

In this work, we apply the knowledge obtained from Chapter 2 on ionic-liquid-based electrolytes to glyme solvents in order to make a pseudosolid electrolyte which is stable in contact with sodium metal. The resulting stability enables the fabrication of SMBs with high energy density coupled with a nonflammable, solid electrolyte. We selected sodium tetrafluoroborate in tetraglyme ($NaBF_4$:G4) as the sodium-ion electrolyte for encapsulation within

silica matrix due to its low vapor pressure and recent success in both sodium-ion and sodium-metal batteries.[27,28]

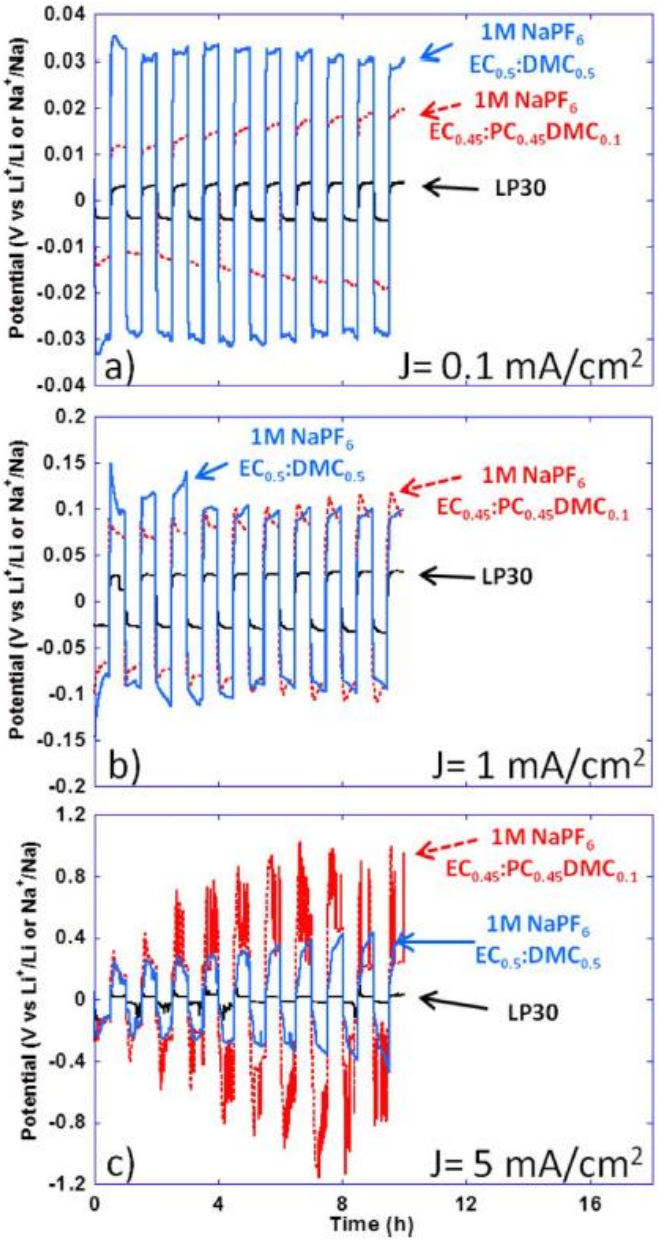

Figure 3.2. Plating/stripping data for symmetric lithium metal and sodium metal cells at **a)** 0.1 mA cm^{-2} **b)** 1 mA cm^{-2} and **c)** 5 mA cm^{-2}. The electrolyte for Li|Li cells is 1M $LiPF_6$ in ethylene carbonate:dimethyl carbonate (1:1, w:w). The electrolyte for Na|Na cells is 1M $NaPF_6$ in either ethylene carbonate:dimethyl carbonate (1:1, w:w) or ethylene carbonate:propylene carbonate:dimethyl carbonate (0.45:0.45:0.1, w:w).[16]

3.2. Experimental

Materials

Tetraethylorthosilicate, formic acid (98%), sodium tetrafluoroborate, poly(vinylidene fluoride-co-hexafluoropropylene) (M_w ~400,000), and all reagents used in the synthesis of NVOPF were purchased from Sigma Aldrich. Tetraethylene glycol dimethyl ether (tetraglyme or G4) was purchased from Acros Chemicals. Carbon-coated aluminum foil was purchased from MTI Corp.

Gel electrolyte synthesis

Poly(vinylidene fluoride-co-hexafluoropropylene) (PVDF-HFP) was first dissolved in acetone at a concentration of 50 mg/mL. Pseudosolid gel electrolytes were synthesized by combining tetraethylorthosilicate (54 µL), PVDF-HFP solution (1 mL), and 1:4 (mol:mol) $NaBF_4$:G4 (150 µL) in a glass vial under stirring. Formic acid (70 µL) was then added to initiate sol formation. This was allowed to stir for 10 minutes at a temperature of 30°C. The solution was subsequently vortex mixed and cast into polypropylene molds of the desired size (typically 2 cm^2). Gelation occurred within 1 hour. Gels were left to dry ambiently for 6 hours followed by 2 hours under vacuum and then overnight under vacuum at 70°C. Electrolytes were then cut to the appropriate size for testing.

Synthesis of (NVOPF@rGO)

Sodium vanadium fluorophosphate ($Na_3(VO)_2(PO_4)_2F$) was synthesized by adapting a previous method.[29] Briefly, 40 mg of freeze-dried graphene oxide (GO) was suspended in water with a sonifier. Then, 2 mmol ammonium vanadate, 3 mmol sodium fluoride, and 2 mmol ammonium dihydrogen phosphate were dissolved sequentially into the GO solution. After 20 minutes

stirring, 20 mL dimethylformamide was added to the mixture and was further stirred for one hour. This solution was then transferred into a Teflon-lined hydrothermal vessel and heated to 180°C for 24 hours. The supernatant of this solution was then removed through centrifugation and washed with water and ethanol multiple times. The resulting powder was dried at 100°C under vacuum before electrode preparation.

Electrode preparation

A slurry was obtained by mixing 85 wt% active material, 10 wt% Ketjen black carbon and 5 wt% PVDF binder in N-methyl-2-pyrrolidone (NMP) and coated onto carbon-coated aluminum foils. The electrodes were dried in a vacuum oven at 120 °C overnight before testing. The mass loading of active material in electrodes was ~1.0 mg cm^{-2}.

Electrochemical characterization

Ionic conductivity was calculated from impedance spectroscopy measured using two polished stainless steel blocking electrodes. An AC voltage of 10 mV was applied with frequencies ranging from 100 mHz to 500 kHz. These same parameters were also used to assess the interfacial resistance of various cells as a function of cycling. The electrochemical stability window of the electrolyte was assessed using linear sweep voltammetry at a sweep rate of 0.1 mV s^{-1} with a carbon-coated aluminum working electrode and a sodium metal counter/reference electrode. Galvanostatic cycling was performed in coin cell format with sodium metal counter/reference electrodes. For experiments involving liquid electrolyte, Celgard 2300 separator was used to prevent electrical shorting.

The transference number was calculated using the Bruce-Vincent method.[30] Briefly, impedance measurements on a symmetric sodium metal cell were taken before and after a 10 mV polarization which lasted until steady state was reached (~4 hours). Equation 3.1 below was used to calculate the transference number:

$$t_{Na^+} = \frac{I_{ss}(\Delta V - I_0 R_0)}{I_0(\Delta V - I_{ss} R_{ss})}$$

Equation 3.1

where I is current, ΔV is the applied polarization potential, and R is the resistance taken from EIS. Subscripts “0” and “SS” indicate the initial and steady state values, respectively.

3.3. Results and Discussion

Various concentrations of glyme-based liquid electrolyte ($NaBF_4$ in tetraglyme) were used in control experiments in order to establish the fundamental properties of this electrolyte. We define the electrolyte in terms of molar ratios (as opposed to molarity) to be accurate when comparing across samples of different volume. Plating/stripping experiments in asymmetric cells were then chosen as a comparison technique. In these experiments (described in Figure 3.3.), we fabricate a cell with sodium metal as the counter/reference electrode and a metal such as copper or aluminum as the working electrode (in this case carbon-coated aluminum). A certain amount of sodium metal plates onto the aluminum for a given time and is stripped off until the voltage rises dramatically, indicating complete sodium metal removal. This technique allows for the efficiency of sodium metal plating/stripping to be calculated as well as for the overpotential to be measured for each cycle.[31–33] In this work, overpotential refers to the additional electrochemical potential needed to drive a reaction past its thermodynamically-determined

value. Because we utilize sodium metal as our reference in these tests, a perfect cell would both plate and strip at 0 V.

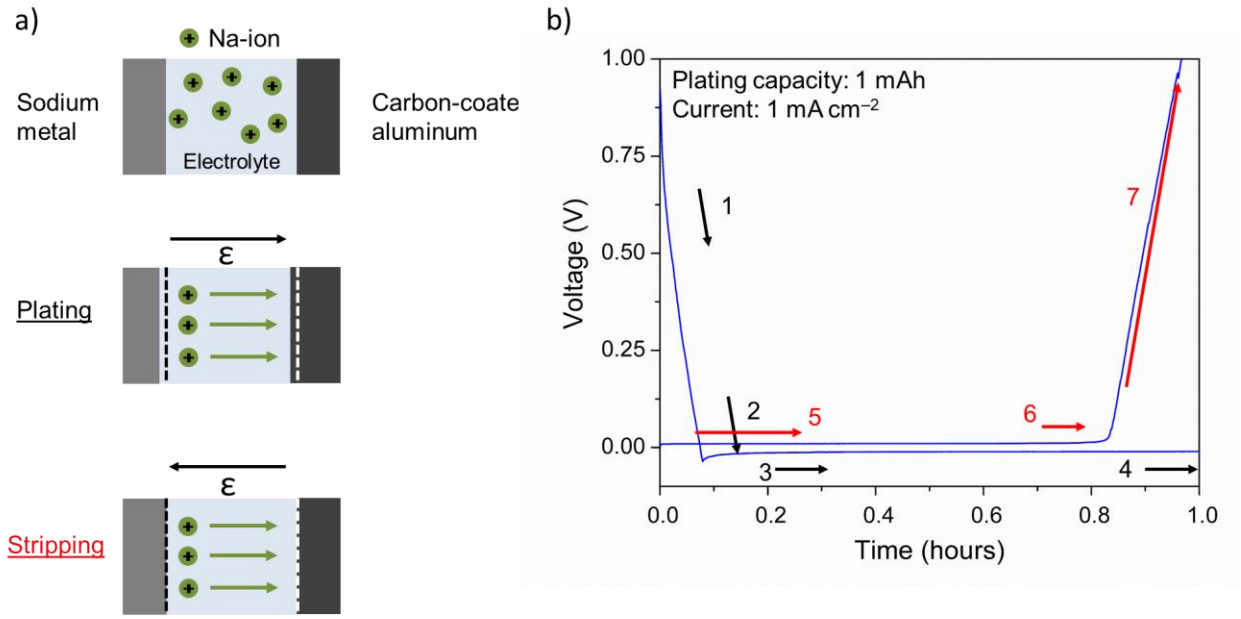

Figure 3.3. a) Schematic representation of the plating/stripping process and **b)** the corresponding response of a constant-current experiment. Step 1: reversible surface reactions with the carbon coating on aluminum foil. Step 2: Nucleation of sodium metal. Step 3: initial growth of sodium metal. Step 4: steady-state growth of sodium metal. Step 5: current reversal and stripping of sodium metal. Step 6: steady-state stripping of sodium-metal. Step 7: stripping of remaining sodium metal and reactions with carbon. A capacity of 1 mAh was plated on each cycle at a current density of 1 mA cm^{-2}.

As can been seen in Figure 3.4., even the initial cycles for 1:4 $NaBF_4$:G4 have an extremely low overpotential of ~11 mV at a moderate current density of 1mA cm^{-2}. This value is among the lowest reported in literature.[25,34–37] At a higher salt concentration of 1:2 $NaBF_4$:G4, the overpotential still remains low, albeit with a slight increase approximately 16 mV. Initial

coulombic efficiency of both cells is incredibly high (>80%) and quickly stabilizes to above 97% within the first few cycles. Long-term cycling for both the 1:2 and 1:4 molar ratio electrolytes is demonstrated in Figure 3.4c,d. We demonstrate 250 cycles without shorting or catastrophic failure while the overpotential and coulombic efficiency (100% after ~cycle 50) remain encouragingly stable. Panels e) and f) of Figure 3.4. track the efficiency and mid-voltage overpotential (measured on the stripping test at the 30-minute point) and demonstrate stabilization in the first tens of cycles.

Based on the stable cycling seen in asymmetric plating/stripping cells, we apply 1:4 NaBF4:G4 in traditional half cells with sodium vanadium fluorophosphate ($Na_3(VO)_2(PO_4)_2F$ (NVOPF)) cathode. This material is known for its two redox plateaus and high-rate capability and is discussed in greater detail later in this chapter.[38–41] Figure 3.5. shows the first cycle of galvanostatic discharge for NVOPF half-cells against sodium metal at a rate of 1C in both 1:4 NaBF4:G4 and standard 1M $NaPF_6$ G2 which is used as the control sample. These data reveal remarkably similar cycling near theoretical capacity for both electrolyte systems. We observe slightly higher polarization for the tetraglyme-based electrolyte which is expected due to its longer chain length and subsequently lower ionic conductivity.[26,42,43]

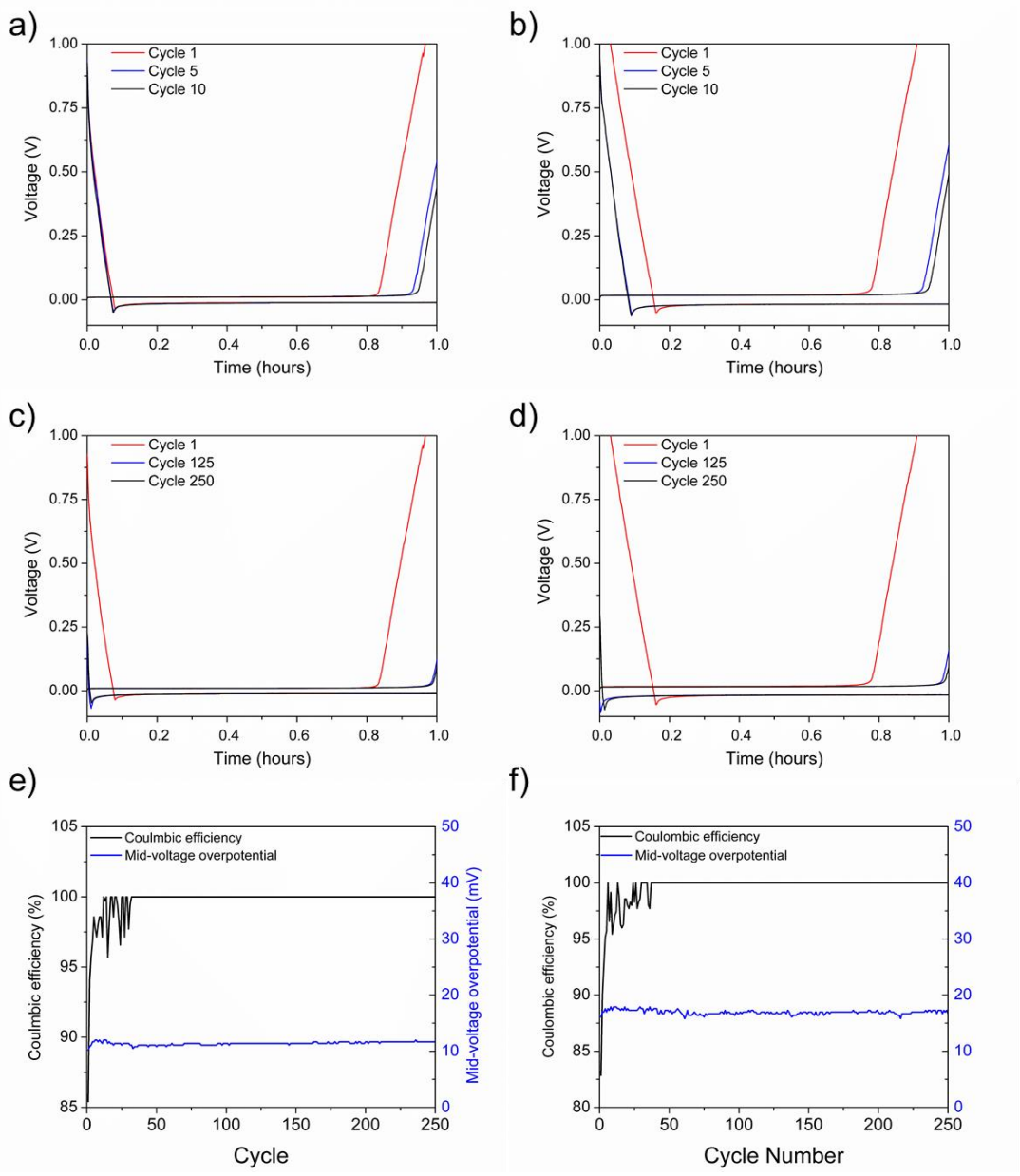

Figure 3.4. a) Selected cycles of plating and stripping experiments with carbon-coated aluminum working and sodium metal counter/reference electrodes at a current density of 1 mA cm^{-2} for a capacity of 1 mAh cm^{-2} for **a,c)** 1:4 $NaBF_4$:G4 and **b,d)** 1:2 $NaBF_4$:G4. Coulombic efficiency and mid-voltage overpotential as a function of cycling for **e)** 1:4 $NaBF_4$:G4 and **f)** 1:2 $NaBF_4$:G4. All tests were one hour of plating and one hour of stripping with a 1V cutoff.

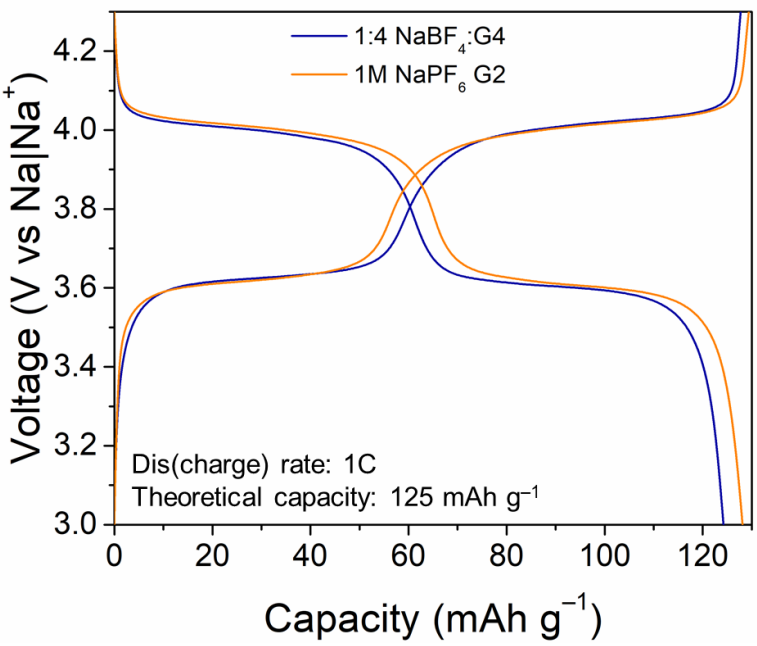

Figure 3.5. First cycle of galvanostatic discharge for NVOPF electrode in 1:4 $NaBF_4$:G4 electrolyte and standard 1M $NaPF_6$ G2 as comparison. The charge/discharge rate is 1C. Testing was performed in half-cell, two-electrode format with NVOPF working electrode and sodium metal counter/reference electrode.

After confirmation of the favorable electrochemical environment for sodium metal in 1:4 $NaBF_4$:G4, we proceeded to incorporating it into a pseudosolid electrolyte. As described previously in Chapter 2 and in literature for ionogels,[44–48] we employ a liquid silica precursor (in this case tetraethyl orthosilicate) in acid-catalyzed, sol-gel synthesis in conjunction with a supporting polymer, poly(vinylidene fluoride-co-hexafluoropropylene) (PVDF-HFP). This polymer is known to provide stability to gel electrolytes for both lithium-ion and sodium-ion batteries.[49–51] After addition of formic acid to catalyze the sol-gel process, we observe gelation within 1–2 hours. We then dry the electrolytes ambiently overnight to allow for complete reaction and then remove by-product solvents (water and methanol) by more aggressive drying at 100°C

under vacuum. As confirmed through thermogravimetric analysis (TGA), these pseudosolid electrolytes are ~60 wt% $NaBF_4$:G4, ~15 wt% PVDF-HFP, and ~15% silica matrix (Figure 3.6.) This ratio of components balances ionic conductivity with mechanical stability.

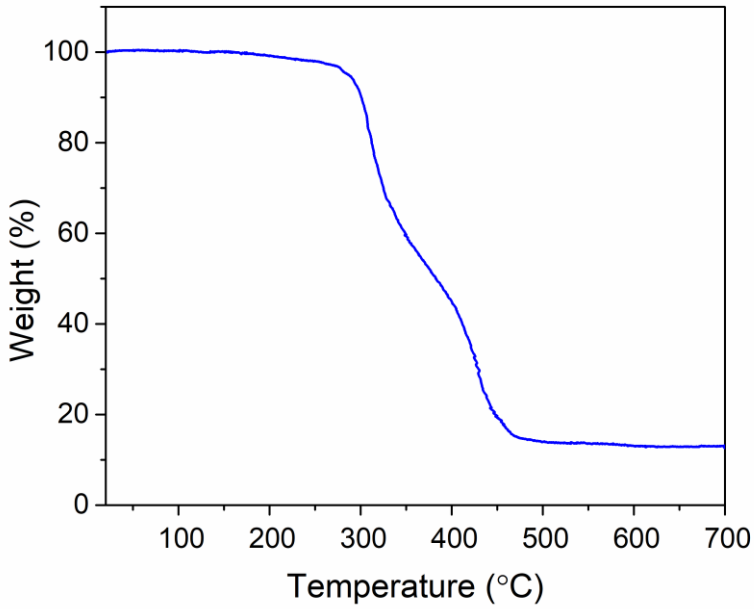

Figure 3.6. Thermogravimetric analysis (TGA) in air of the glyme-based gel electrolyte. Heating rate: 10 °C min^{-1}.

Electrochemical impedance spectroscopy (EIS) probed the ionic conductivity of the $NaBF_4$:G4 pseudosolid electrolyte. As seen in Figure 3.7., we observe a room-temperature ionic conductivity of 0.9 mS cm^{-1} for the glyme-based gel electrolyte which is larger than many solid electrolytes and on par with many liquid electrolytes.[3,52] Additionally, the ionic conductivity of the solid electrolyte is only slightly diminished from that of it liquid counterpart (1.3 mS cm^{-1}). We also determined the electrochemical stability window (ESW) of the electrolyte systems using linear sweep voltammetry (LSV). In this setup, sodium metal acts as both counter and reference

electrode while carbon-coated aluminum acts as the working electrode. The positive sweep (blue) and negative sweep (green) were performed on two different cells to avoid influence of degradation products on the opposite sweep direction. Figure 3.7.b shows a wide ESW of over 4V even at conservative current cutoffs below 100 μA cm^{-2}. This large window enables the use of high-potential electrode materials which can significantly boost the energy density of new SMB devices. In addition, a wide voltage window helps diminish the amount of electrolyte degradation experienced upon cycling which will increase device longevity and cycling stability. On the negative potential sweep, reversible sodium metal plating and stripping is discussed extensively later in this chapter.

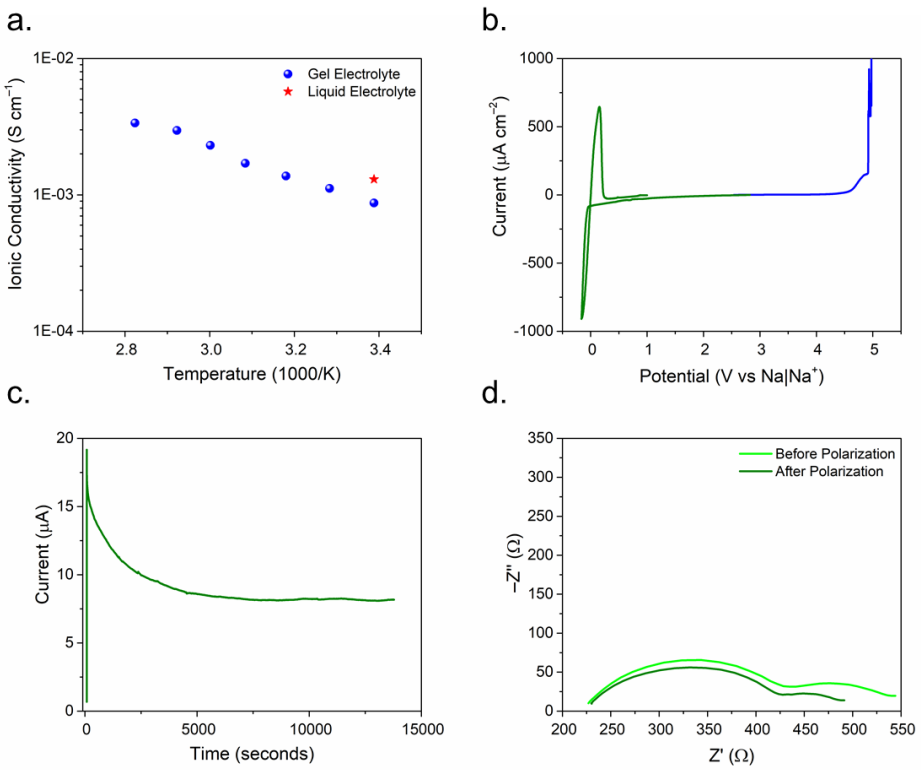

Figure 3.7. a) Ionic conductivity as a function of temperature for the glyme-based gel electrolyte. The liquid electrolyte was included for comparison at room temperature. **b)** Electrochemical stability window tests for the pseudosolid electrolytes. This test was performed with a carbon-coated aluminum working electrode and a sodium metal counter/reference electrode at a sweep rate of 1 mV s^{-1}. Tests for measuring the transference number of the glyme-based pseudosolid electrolyte including the **c)** polarization step and **d)** impedance before/after polarization to extract resistance values.

Another important aspect of an electrolyte for sodium-ion batteries is the transference number which is a measure of the fraction of current delivered by the carrier in question (in this case Na^+). We extract this value utilizing the Bruce-Vincent method which involves measuring the resistance of a symmetrical sodium metal cell using EIS before and after a small potential

hold (Figure 3.7 c,d) . Using Equation 3.1, a transference number of 0.3 was calculated for our glyme-based pseudosolid electrolyte which is on par with many liquid and solid electrolytes in literature.[53–55] A high transference number allows for more rapid ion conduction and helps dissipate concentration gradients more quickly at high rates of charge/discharge.[56]

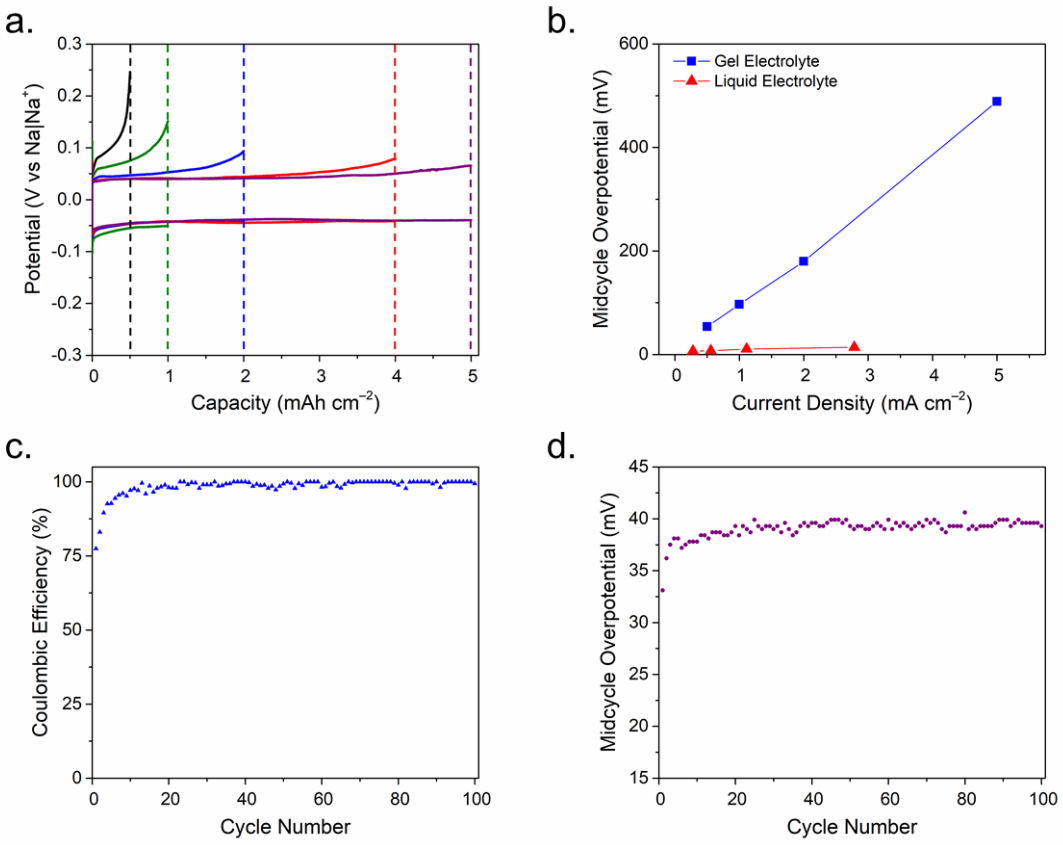

Figure 3.8. Plating/stripping experiments for a cell with a carbon-coated aluminum working electrode, sodium metal counter/reference electrode, and the glyme-based gel electrolyte **a)** Increasing plating capacity from 0.5 mAh cm^{-2} to 5 mAh cm^{-2} at a current density of 0.5 mA cm^{-2}. **b)** Midcycle overpotential taken on the plating cycle as a function of current density with a plating capacity of 1 mAh cm^{-2} for both the liquid and gel electrolyte of 1:4 $NaBF_4$:G4. **c)** Coulombic efficiency and **d)** midcycle overpotential for long-term cycling at a current density of 0.5 mAh cm^{-2}.

Due to the tremendous stability of the liquid electrolyte with sodium metal, we fabricate various cells to probe the plating/stripping behavior of the glyme-based solid electrolyte. In each of these cells, the working electrode is carbon-coated aluminum and the counter/reference electrode is sodium metal. In coin cell format, we investigated our gel electrolyte as a monolith which is sandwiched between the two electrodes. The results for plating/stripping tests with increasing plating capacity can be seen in Figure 3.8a. Even at a high capacity of 5 mAh cm^{-2}, this system can reversibly plate and strip with no apparent degradation or loss in efficiency. This trait is vital for energy-dense batteries which take full advantage of the large capacity of sodium metal. In addition to large capacity, our glyme-based gel electrolyte is able to plate sodium with a relatively low overpotential, even at high current densities. A low overpotential ensures a high energy efficiency and reversibility at high current densities. In Figure 3.8b, an extraordinarily low overpotential (~50 mV) is observed for the gel electrolyte at a current density of 0.5 mA cm^{-2} which only increases to about 500 mV at 5 mA cm^{-2}. Although greater than that of the $NaBF_4$:G4 liquid electrolyte, these values are among the lowest reported for any electrolyte system.[5,12,13] At a current density of 5 mA cm^{-2}, the electrolyte begins to exhibit increased polarization at the end of its plating cycle (Figure 3.9.) which likely points to the onset of dendrite formation. This system is also capable of long-term stability, as evidenced by Figure 3.8c,d which plot the Coulombic efficiency and midcycle overpotential for a current density of 0.5 mA cm^{-2} over 100 cycles. Stability over hundreds of cycles is crucial for battery longevity and reliable performance.

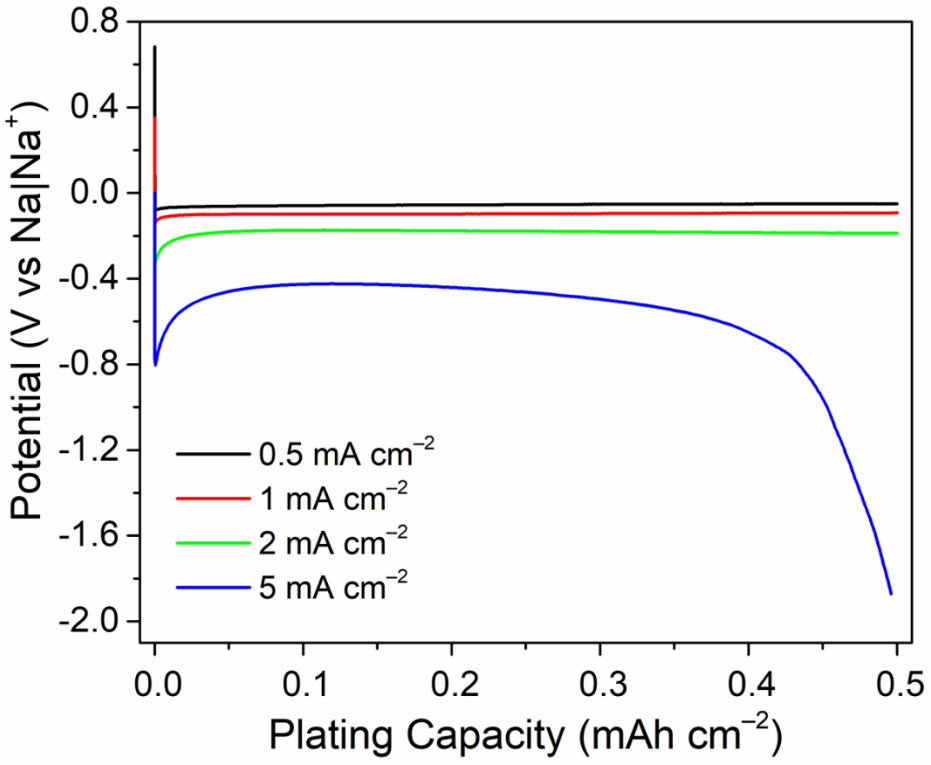

Figure 3.9. Galvanostatic sodium plating curves for various current densities. Carbon-coated aluminum working electrode, sodium metal counter/reference electrode, and glyme-based gel electrolyte.

We probe the interfacial resistance of the sodium metal plating/stripping utilizing EIS as a function of cycling. In this setup, we use a symmetric sodium metal cell and take an EIS measurement after each plating cycle (Figure 3.10). The first cycle demonstrates a significantly larger resistance in Figure 3.9a than the subsequent cycles which can be seen in Figure 3.9b with a smaller data range. After the first cycle, the total resistance of the cell settles around 85 Ohms and remains invariant with further cycling. This is likely due to the removal of surface oxides, hydroxides, etc. on the sodium metal in the first cycle.

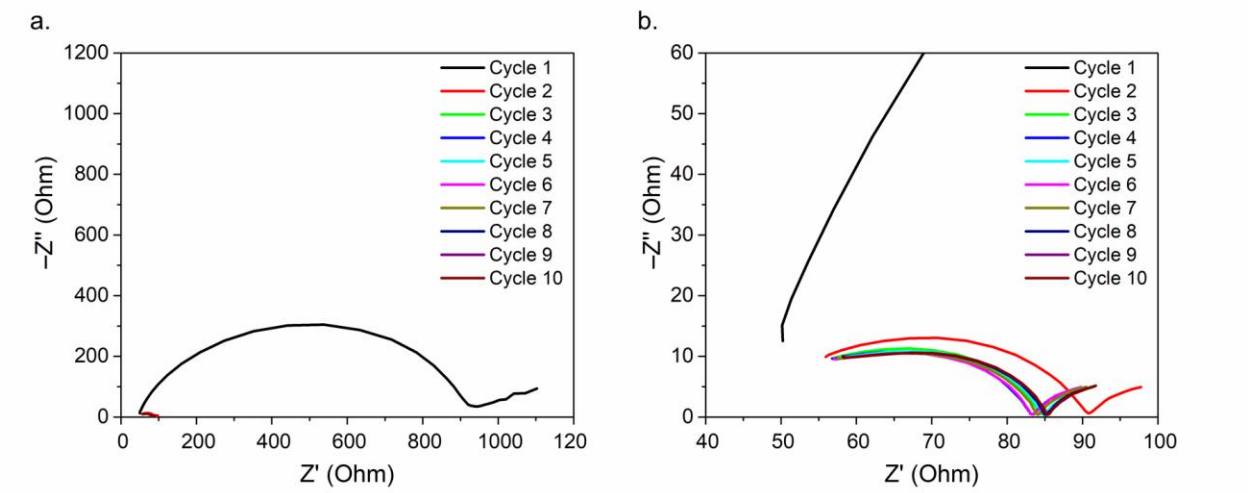

Figure 3.10. Electrochemical impedance spectroscopy (EIS) taken after each plating cycle for a symmetrical sodium sandwiching the glyme-based gel electrolyte. **a)** The full data range and **b)** a reduced range show the decrease in cell resistance after the first cycle.

To demonstrate the full capability of the glyme-based gel electrolyte, we construct a sodium-metal battery with NVOPF cathode. This material is grown onto reduced graphene oxide (rGO) though hydrothermal synthesis. The presence of rGO greatly improves the electronic conductivity and improves rate capability as well as cycle stability. We confirm the phase, amount of rGO, and morphology in Figure 3.11. XRD reveals peak positions which correspond completely to NVOPF[38–41] and no impurity phases. The amount of carbon scaffold was tuned to ~12 wt%, as confirmed by thermogravimetric analysis, which balances conductivity and active material accessibility. Finally, we observe a nanorod morphology with a diameter of ~200nm and a length of ~1 µm in Figure 3.11c,d.

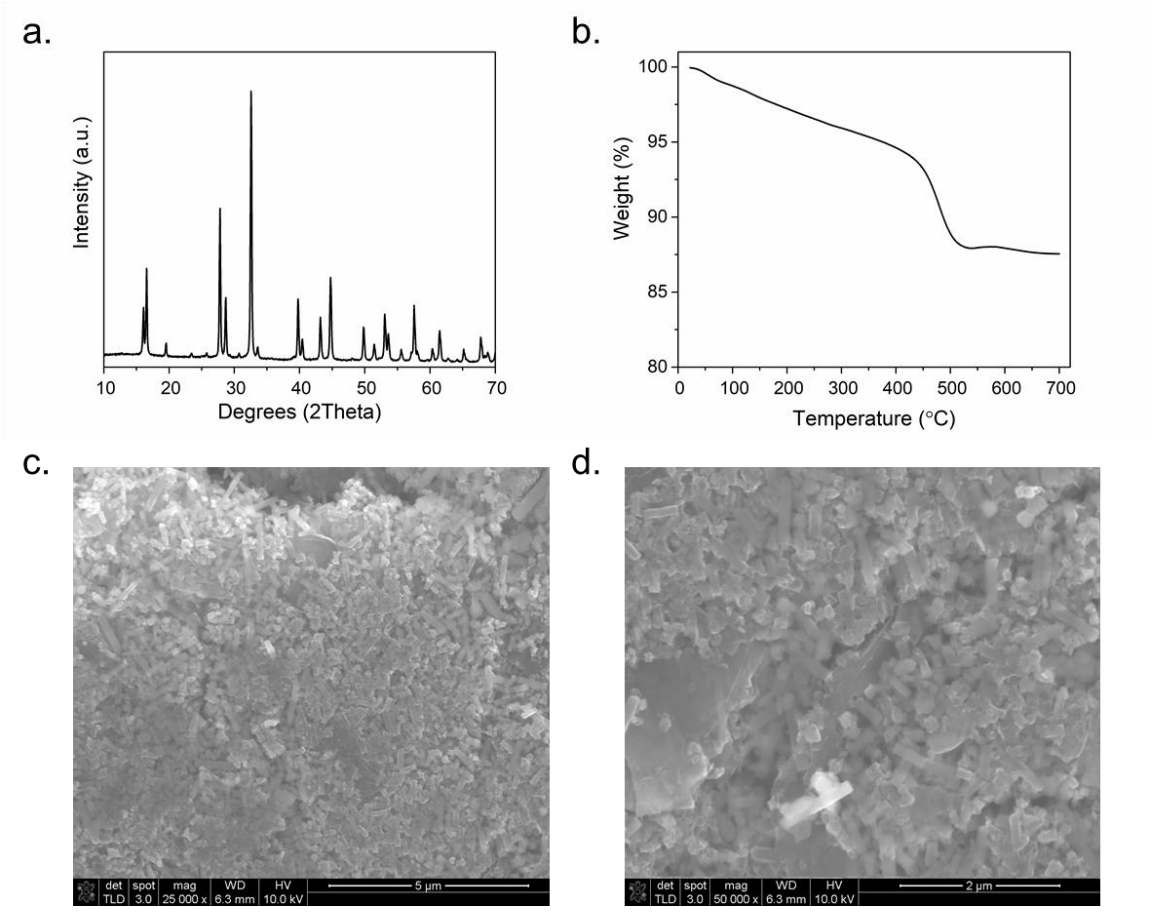

Figure 3.11. a) X-ray diffraction (XRD) **b)** thermogravimetric analysis (TGA) and **c,d)** scanning electron microscopy (SEM) images of the NVOPF@rGO cathode.

Electrochemically, our SMB with glyme-based gel electrolyte and NVOPF cathode demonstrates stable cycling and moderate rate capability. As seen in Figure 3.12a, we achieve near theoretical capacity for the NVOPF (130 mAh g^{-1} based on two electron redox) and two flat redox plateaus at a rate of 0.5C. Even at 1C, (Figure 3.12b), our solid-state SMB still delivers over 100 mAh g^{-1} with capability of supporting high charge/discharge rates. Our outstanding stability with sodium metal is further shown by the reversible cycling seen in Figure 3.12c for 100 cycles at a rate of 0.5C. [57–59] We achieve a specific energy (based on the weight of both

electrodes) of ~500 Wh kg^{-1} at a rate of 0.5C and can also deliver ~200 Wh kg^{-1} at a specific power of ~1900 W kg^{-1}. In addition to being thermally-stable and nonflammable, our SMB is competitive with other solid-state, sodium-ion batteries (Figure 3.12d) and is compatible with sodium-metal anodes. Other solid-state systems utilize polymers soaked in flammable carbonate electrolyte[57,58] or true solid electrolytes[59] with limited rate capability.

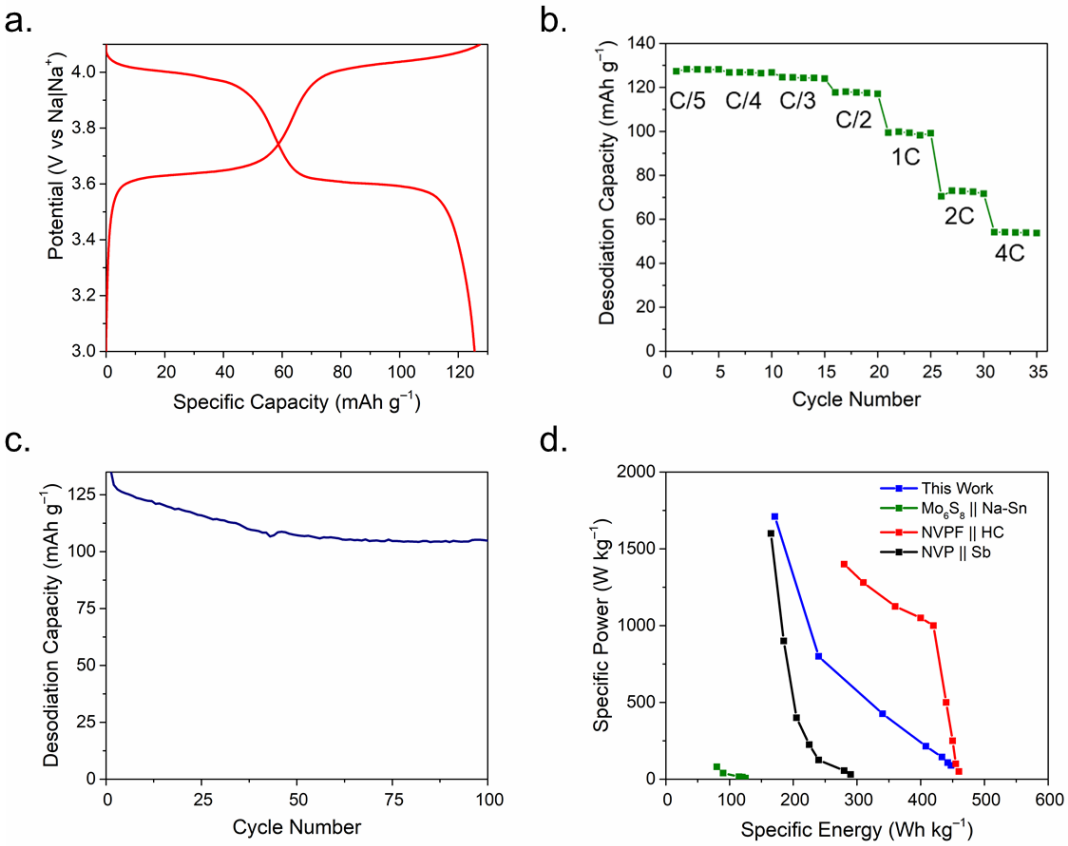

Figure 3.12. Electrochemical results for the NVOPF sodium-metal battery with glyme-based gel electrolyte. **a)** Charge/discharge curve at a rate of 0.5C **b)** Rate retention for C-rates: 0.2C, 0.25C, 0.33C, 0.5C, 1C, 2C, and 4C **c)** long-term cycling at a rate of 0.5C **d)** Ragone plot comparing this work to other full-cell, sodium-based devices.[57–59]

3.4. Conclusions

We demonstrate the synthesis and electrochemical properties of a glyme solvent encapsulated within a silica matrix as a pseudosolid electrolyte for sodium-metal batteries (SMBs). Combinations of sodium tetrafluoroborate in tetraglyme solvent exhibit extremely low overpotentials of ~11 mV which remain invariant with capacity and with cycling. The initial coulombic efficiency is high (>80%) and this quickly stabilizes to above 97% within the first few cycles. Long-term cycling (>200 cycles) was demonstrated without shorting or catastrophic failure. A 1:4 molar ratio of $NaBF_4$:G4 gel electrolyte was also evaluated in two-electrode cells with $Na_3(VO)_2(PO_4)_2F$ (NVOPF) cathode and sodium metal anode, achieving near theoretical capacity and 500 Wh kg^{-1} at a charge/discharge rate of 0.5C.

3.5. References

1. Vaalma, C., Buchholz, D., Weil, M. & Passerini, S. A cost and resource analysis of sodium-ion batteries. *Nature Reviews Materials* **3**, 18013 (2018).
2. Tang, J., Dysart, A. D. & Pol, V. G. Advancement in sodium-ion rechargeable batteries. *Current Opinion in Chemical Engineering* **9**, 34–41 (2015).
3. Kim, J.-J., Yoon, K., Park, I. & Kang, K. Progress in the Development of Sodium-Ion Solid Electrolytes. *Small Methods* **1**, 1700219 (2017).
4. Chen, L. *et al.* Readiness Level of Sodium-Ion Battery Technology: A Materials Review. *Adv. Sustainable Syst.* **2**, 1700153 (2018).
5. Wang, Y. *et al.* Developments and Perspectives on Emerging High-Energy-Density Sodium-Metal Batteries. *Chem* **5**, 2547–2570 (2019).
6. Zheng, X. *et al.* Sodium metal anodes for room-temperature sodium-ion batteries: Applications, challenges and solutions. *Energy Storage Materials* **16**, 6–23 (2019).
7. Ye, H. *et al.* Realizing a Highly Stable Sodium Battery with Dendrite-Free Sodium Metal Composite Anodes and O3-Type Cathodes. *Nano Energy* doi:10.1016/j.nanoen.2018.03.069.
8. Zhao, Y., Adair, K. R. & Sun, X. Recent developments and insights into the understanding of Na metal anodes for Na-metal batteries. *Energy & Environmental Science* **11**, 2673–2695 (2018).
9. Delmas, C. Sodium and Sodium-Ion Batteries: 50 Years of Research. *Adv. Energy Mater.* **8**, 1703137 (2018).
10. Siburian, R. *et al.* Performance of graphite and graphene as electrodes in primary cell battery. *J. Phys.: Conf. Ser.* **1116**, 042034 (2018).
11. Patry, G., Romagny, A., Martinet, S. & Froelich, D. Cost modeling of lithium-ion battery cells for automotive applications. *Energy Sci Eng* **3**, 71–82 (2015).

12. Matios, E., Wang, H., Wang, C. & Li, W. Enabling Safe Sodium Metal Batteries by Solid Electrolyte Interphase Engineering: A Review. *Ind. Eng. Chem. Res.* **58**, 9758–9780 (2019).
13. Lee, B., Paek, E., Mitlin, D. & Lee, S. W. Sodium Metal Anodes: Emerging Solutions to Dendrite Growth. *Chem. Rev.* **119**, 5416–5460 (2019).
14. Peled, E. Advanced Model for Solid Electrolyte Interphase Electrodes in Liquid and Polymer Electrolytes. *J. Electrochem. Soc.* **144**, L208 (1997).
15. Conder, J. & Villevieille, C. How reliable is the Na metal as a counter electrode in Na-ion half cells? *Chem. Commun.* **55**, 1275–1278 (2019).
16. Iermakova, D. I., Dugas, R., Palacín, M. R. & Ponrouch, A. On the Comparative Stability of Li and Na Metal Anode Interfaces in Conventional Alkyl Carbonate Electrolytes. *Journal of The Electrochemical Society* **162**, A7060–A7066 (2015).
17. Zarrabeitia, M., Muñoz-Márquez, M. Á., Nobili, F., Rojo, T. & Casas-Cabanas, M. Influence of Using Metallic Na on the Interfacial and Transport Properties of Na-Ion Batteries. *Batteries* **3**, 16 (2017).
18. Hwang, J., Takeuchi, K., Matsumoto, K. & Hagiwara, R. NASICON *vs.* Na metal: a new counter electrode to evaluate electrodes for Na secondary batteries. *J. Mater. Chem. A* **7**, 27057–27065 (2019).
19. Westman, K. *et al.* Diglyme Based Electrolytes for Sodium-Ion Batteries. *ACS Applied Energy Materials* **1**, 2671–2680 (2018).
20. He, Y., Bai, P., Gao, S. & Xu, Y. Marriage of an Ether-Based Electrolyte with Hard Carbon Anodes Creates Superior Sodium-Ion Batteries with High Mass Loading. *ACS Applied Materials & Interfaces* **10**, 41380–41388 (2018).
21. Zhang, J. *et al.* Achieving superb sodium storage performance on carbon anodes through an ether-derived solid electrolyte interphase. *Energy & Environmental Science* **10**, 370–376 (2017).

22. Pham, D. T. *et al.* A zero fading sodium ion battery: High compatibility microspherical patronite in ether-based electrolyte. *Energy Storage Materials* **19**, 270–280 (2019).
23. Li, K. *et al.* Evolution of the electrochemical interface in sodium ion batteries with ether electrolytes. *Nat Commun* **10**, 725 (2019).
24. Goktas, M. *et al.* Stable and Unstable Diglyme-Based Electrolytes for Batteries with Sodium or Graphite as Electrode. *ACS Appl. Mater. Interfaces* **11**, 32844–32855 (2019).
25. Seh, Z. W., Sun, J., Sun, Y. & Cui, Y. A Highly Reversible Room-Temperature Sodium Metal Anode. *ACS Central Science* **1**, 449–455 (2015).
26. Tang, S. & Zhao, H. Glymes as versatile solvents for chemical reactions and processes: from the laboratory to industry. *RSC Adv.* **4**, 11251 (2014).
27. Rudola, A., Gajjela, S. R. & Balaya, P. High energy density in-situ sodium plated battery with current collector foil as anode. *Electrochemistry Communications* **86**, 157–160 (2018).
28. Rudola, A., Du, K. & Balaya, P. Monoclinic Sodium Iron Hexacyanoferrate Cathode and Non-Flammable Glyme-Based Electrolyte for Inexpensive Sodium-Ion Batteries. *J. Electrochem. Soc.* **164**, A1098–A1109 (2017).
29. Dong, J. *et al.* Intercalation pseudocapacitance of FeVO4·nH2O nanowires anode for high-energy and high-power sodium-ion capacitor. *Nano Energy* **73**, 104838 (2020).
30. Evans, J., Vincent, C. A. & Bruce, P. G. Electrochemical measurement of transference numbers in polymer electrolytes. *Polymer* **28**, 2324–2328 (1987).
31. Adams, B. D., Zheng, J., Ren, X., Xu, W. & Zhang, J.-G. Accurate Determination of Coulombic Efficiency for Lithium Metal Anodes and Lithium Metal Batteries. *Adv. Energy Mater.* **8**, 1702097 (2018).
32. Boyle, D. T. *et al.* Transient Voltammetry with Ultramicroelectrodes Reveals the Electron Transfer Kinetics of Lithium Metal Anodes. *ACS Energy Lett.* **5**, 701–709 (2020).

33. Peng, Z. *et al.* High-Power Lithium Metal Batteries Enabled by High-Concentration Acetonitrile-Based Electrolytes with Vinylene Carbonate Additive. *Adv. Funct. Mater.* 2001285 (2020) doi:10.1002/adfm.202001285.
34. Li, P. *et al.* Highly reversible Na and K metal anodes enabled by carbon paper protection. *Energy Storage Materials* **15**, 8–13 (2018).
35. Lee, J. *et al.* Ultraconcentrated Sodium Bis(fluorosulfonyl)imide-Based Electrolytes for High-Performance Sodium Metal Batteries. *ACS Appl. Mater. Interfaces* **9**, 3723–3732 (2017).
36. Zhao, Y. *et al.* Superior Stable and Long Life Sodium Metal Anodes Achieved by Atomic Layer Deposition. *Adv. Mater.* **29**, 1606663 (2017).
37. Sun, B. *et al.* Dendrite-Free Sodium-Metal Anodes for High-Energy Sodium-Metal Batteries. *Adv. Mater.* **30**, 1801334 (2018).
38. Chao, D. *et al.* Sodium Vanadium Fluorophosphates (NVOPF) Array Cathode Designed for High-Rate Full Sodium Ion Storage Device. *Adv. Energy Mater.* **8**, 1800058 (2018).
39. Deng, G. *et al.* Graphene quantum dots-shielded Na3(VO)2(PO4)2F@C nanocuboids as robust cathode for Na-ion battery. *Energy Storage Materials* **5**, 198–204 (2016).
40. Du, P., Li, T., Jiang, X., Wang, D. & Zheng, X. Improving the electrochemical performance of Na3V2O2(PO4)2F cathode by using a defect-containing TiO2- coating for sodium ion batteries. *Journal of Alloys and Compounds* **814**, 152270 (2020).
41. Yin, Y. *et al.* Robust three-dimensional graphene skeleton encapsulated Na3V2O2(PO4)2F nanoparticles as a high-rate and long-life cathode of sodium-ion batteries. *Nano Energy* **41**, 452–459 (2017).
42. Galle Kankanamge, S. R. *et al.* Mechanism behind the Unusually High Conductivities of High Concentrated Sodium Ion Glyme-Based Electrolytes. *J. Phys. Chem. C* **122**, 25237–25246 (2018).

43. Li, K. *et al.* Predicting Ion Association in Sodium Electrolytes: A Transferrable Model for Investigating Glymes. *J. Phys. Chem. C* **122**, 4747–4756 (2018).
44. Ashby, D. S., DeBlock, R. H., Lai, C.-H., Choi, C. S. & Dunn, B. S. Patternable, Solution-Processed Ionogels for Thin-Film Lithium-Ion Electrolytes. *Joule* **1**, 344–358 (2017).
45. Chen, N. *et al.* Biomimetic ant-nest ionogel electrolyte boosts the performance of dendrite-free lithium batteries. *Energy Environ. Sci.* **10**, 1660–1667 (2017).
46. Wang, S. *et al.* Comparative studies on electrochemical cycling behavior of two different silica-based ionogels. *Journal of Power Sources* **301**, 299–305 (2016).
47. Negre, L., Daffos, B., Turq, V., Taberna, P. L. & Simon, P. Ionogel-based solid-state supercapacitor operating over a wide range of temperature. *Electrochimica Acta* **206**, 490–495 (2016).
48. Wu, F., Chen, N., Chen, R., Wang, L. & Li, L. Organically modified silica-supported ionogels electrolyte for high temperature lithium-ion batteries. *Nano Energy* **31**, 9–18 (2017).
49. Hashmi, S. A. *et al.* Ionic liquid-based sodium ion-conducting composite gel polymer electrolytes: effect of active and passive fillers. *J Solid State Electrochem* **20**, 2817–2826 (2016).
50. Kumar, D. & Hashmi, S. A. Ionic liquid based sodium ion conducting gel polymer electrolytes. *Solid State Ionics* **181**, 416–423 (2010).
51. Mendes, T. C. *et al.* Supported Ionic Liquid Gel Membrane Electrolytes for a Safe and Flexible Sodium Metal Battery. *ACS Sustainable Chemistry & Engineering* (2019) doi:10.1021/acssuschemeng.8b06212.
52. Ponrouch, A. *et al.* Non-aqueous electrolytes for sodium-ion batteries. *J. Mater. Chem. A* **3**, 22–42 (2015).

53. Thangadurai, V. & Weppner, W. Determination of the Sodium Ion Transference Number of the Dion−Jacobson-Type Layered Perovskite $NaCa_2Nb_3O_{10}$ Using ac Impedance and dc Methods. *Chem. Mater.* **14**, 1136–1143 (2002).
54. Chen, F., Howlett, P. & Forsyth, M. Na-Ion Solvation and High Transference Number in Superconcentrated Ionic Liquid Electrolytes: A Theoretical Approach. *J. Phys. Chem. C* **122**, 105–114 (2018).
55. Forsyth, M. *et al.* Novel Na^+ Ion Diffusion Mechanism in Mixed Organic–Inorganic Ionic Liquid Electrolyte Leading to High Na^+ Transference Number and Stable, High Rate Electrochemical Cycling of Sodium Cells. *The Journal of Physical Chemistry C* **120**, 4276–4286 (2016).
56. Doyle, M., Fuller, T. F. & Newman, J. The importance of the lithium ion transference number in lithium/polymer cells. *Electrochimica Acta* **39**, 2073–2081 (1994).
57. Guo, J.-Z. *et al.* Quasi-Solid-State Sodium-Ion Full Battery with High-Power/Energy Densities. *ACS Appl. Mater. Interfaces* **10**, 17903–17910 (2018).
58. Gao, H., Zhou, W., Park, K. & Goodenough, J. B. A Sodium-Ion Battery with a Low-Cost Cross-Linked Gel-Polymer Electrolyte. *Adv. Energy Mater.* **6**, 1600467 (2016).
59. Yue, J. *et al.* Long Cycle Life All-Solid-State Sodium Ion Battery. *ACS Appl. Mater. Interfaces* **10**, 39645–39650 (2018).

Chapter 4: Amorphous vanadium dioxide as a high-capacity electrode for sodium-ion batteries

We investigate amorphous vanadium dioxide (a–VO_2), synthesized by a simple precipitation reaction heat treatment, as a host for sodium-ion storage. In contrast to its crystalline form, we observe pseudocapacitive-like properties of a-VO_2. When grown onto graphene foam (explored in Appendix A), this material exhibits extremely fast charges storage and supports ~400 mAh g^{-1}. Based on these results, we expect amorphous materials to be more seriously investigated as charge-storage hosts for a variety of alkali ions.

4.1. Introduction and Background

Traditional electrochemically-active materials in rocking-chair type batteries have layered- or tunnel-type structures which can reversibly intercalate/deintercalate lithium ions.[1] When investigating new materials for lithium-ion storage, researchers often focus on interlayer spacing and available crystallographic space for lithium insertion as a route towards improving both rate and cyclability.[2–4] As a consequence of the larger cationic size of sodium, there are generally fewer host materials for sodium-ion insertion compared to lithium-ion insertion.[5–7]

Amorphous materials, as a consequence of their disordered structure, are one route towards combating this issue and researchers have recently investigated their advantages over crystalline materials for electronic applications.[8–10] Amorphous metal oxides in particular are potential candidates in electrochemical systems and have shown promise as supercapacitor materials.[11,12] Due to their random arrangement of metal-oxygen bonds and lack of long-range order, amorphous oxides can have significantly different properties from their crystalline analogues.[13,14] Generally, amorphous oxides have higher surface area, higher tensile strength,

and better chemical stability than crystalline oxides.[15] From an electrochemical perspective, amorphous oxides have several desirable features (depicted in Figure 4.1.):

- *Accommodation of volume change*

  Due to their extra free volume, amorphous materials are better equipped to handle the volumetric changes associated with ion intercalation.[16] This feature leads to lower mechanical stress upon cycling which increases cycle life and Coulombic efficiency.[17,18] In fact, strain values near 1% have been observed for the common lithium-ion battery material $LiNi_{0.33}Mn_{0.33}Co_{0.33}O_2$ (NMC) upon intercalation/deintercaltion.[19] Although lithium-ion storage is possible in many materials, larger ions such as sodium and potassium are much more difficult to insert. Figure 4.2. depicts the differences in ion storage for various crystalline materials compared with amorphous iron phosphate. Especially for large ions such as potassium, many crystalline lattices do not have sufficient room for intercalation.[20]

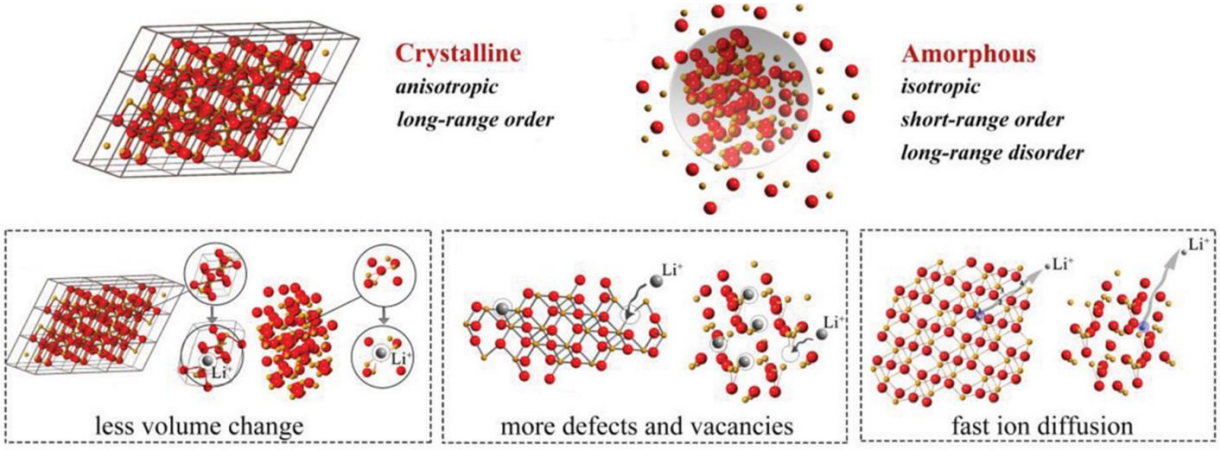

Figure 4.1. Differentiation of crystalline and amorphous materials. Bottom tiles depict the potential advantages of amorphous materials for energy storage.[15]

- *Isotropic electronic properties*

  Although materials with layered or tunnel structures provide pathways for ion diffusion, they are also generally restricted to facile diffusion in limited crystallographic directions. In contrast, amorphous materials are isotropic and do not suffer from asymmetry in properties such as electronic conductivity or active site availability.[21]

- *Improved diffusional kinetics*

  As a consequence of having a homogenous distribution of active sites, amorphous materials tend to have better reaction kinetics.[22,23] In addition, crystalline materials tend to be diffusion-limited by the nucleation and growth of new phases when undergoing lithiation/delithiation.[24] Amorphous materials, on the other hand, have no such limitations and undergo substantially faster redox.[16]

Despite the overwhelming benefits of amorphous materials for energy storage they are somewhat difficult to characterize structurally with commonplace laboratory equipment. The simplest and quickest method to assess the structure of a material is with X-ray diffraction (XRD). Although powerful, this technique provides limited to no information on amorphous materials due to their lack of long-range order. To accurately probe the local structure of amorphous materials, X-ray absorption techniques such as X-ray absorption near-edge structure (XANES) and X-ray absorption fine structure (XAFS) are generally required.[25] These techniques have been successfully employed to characterize amorphous battery materials and are becoming increasingly popular.[26–28]

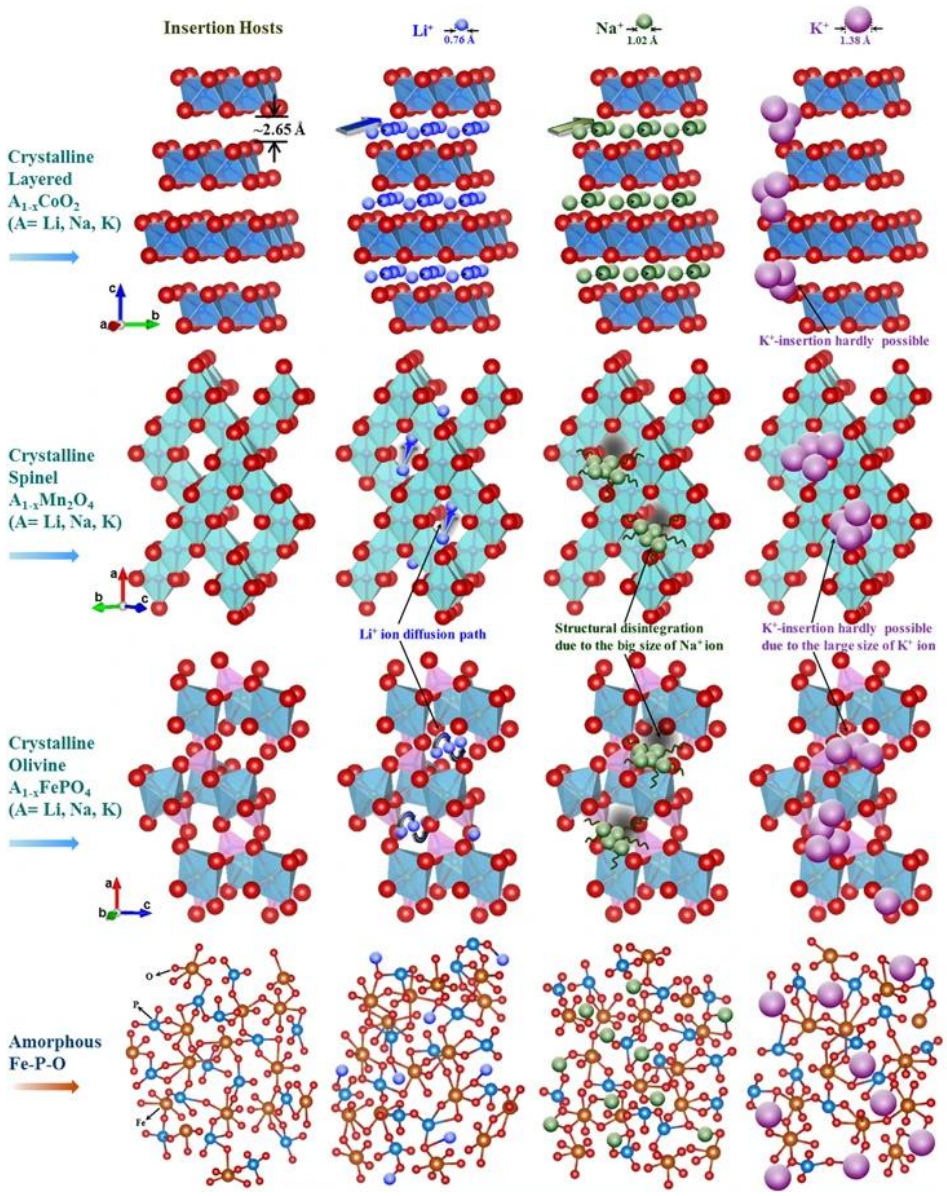

Figure 4.2. Schematic of alkali-ion charge storage in both crystalline materials (cobalt oxides, manganese oxides, and iron phosphate) and amorphous iron phosphate. For large ions such as potassium, many crystalline hosts cannot provide adequate space for insertion, but the extra free volume in amorphous materials makes it a possibility.[20]

Recently, work on amorphous vanadium pentoxide has shown promising results for lithium-ion batteries. For example, Chae et. al demonstrated that amorphous V_2O_5 stored nearly four times more capacity than crystalline V_2O_5 in nonaqueous lithium electrolyte.[29] Uchaker et. al similarly demonstrated a significant increase in capacity when utilizing amorphous V_2O_5 in sodium electrolyte.[18] In an aqueous LiCl solution, amorphous VO_x of mixed-valence demonstrated over 100,000 cycles with minimal capacitive decay.[17] Thus far, amorphous vanadium dioxide (a–VO_2) has been fairly unexplored as an energy storage material for sodium-ion batteries. Because crystalline VO_2 offers significantly higher electronic conductivity and a unique metal-insulator phase transition, we hypothesized that VO_2 would experience even greater benefits than V_2O_5 upon amorphization. Herein, we describe the synthesis and characterization of a–VO_2 as a sodium-ion storage material.

4.2. Experimental

Synthesis

The synthesis pathway is summarized in Figure 4.3. Specifically, 526 mg $VOSO_4 \cdot xH_2O$ (Sigma Aldrich) was stirred into 5 mL DI water at room temperature. Separately, 543 mg of NH_4HCO_3 was dissolved into 5 mL DI water at room temperature. After complete dissolution, the ammonium bicarbonate solution was slowly added dropwise over 15 minutes to the vanadium sulfate solution. This mixture stirred for 1 hour and an amorphous, brown precipitate of $VO(OH)_2$ formed.

The precipitate was separated by centrifugation and washed repeatedly with water and then ethanol (three times each). Following washing, the precipitate was dried at 75°C on a

Schlenk line overnight. For conversion to amorphous VO_2, the $VO(OH)_2$ was heat treated at 275°C for 3 hours in flowing argon atmosphere.

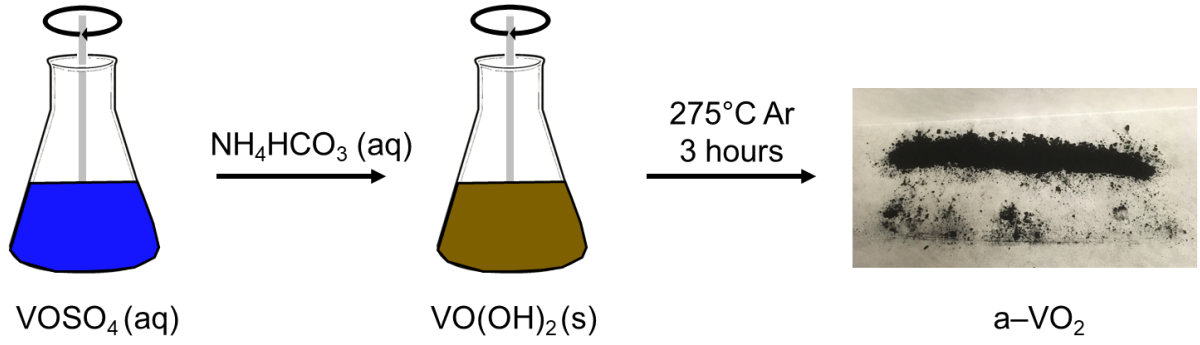

Figure 4.3. Schematic of the synthesis for amorphous VO_2.

Crystalline VO_2(B) was synthesized through a hydrothermal method. Briefly, 5mmol of vanadium pentoxide (Sigma Aldrich) was dispersed in a mixture of 35 mL DI water and 2 mL methanol using a sonication probe for 5 minutes. This mixture was then transferred into a Teflon-lined autoclave and heated to 200°C for 24 hours. The resulting blue powder was washed thoroughly with water followed by ethanol (three times each). Following washing, the precipitate was dried at 75°C on a Schleck line overnight.

Structural and chemical characterization

Transmission electron microscopy (TEM) and electron diffraction were performed on an FEI T12 Cryo-electron microscope. X-ray photoelectron spectroscopy (XPS) was performed on

a Kratos Axis Ultra with a monochromatic aluminum X-ray source. X-ray diffraction (XRD) was performed on a PANalytical X'Pert Pro using a Cu Kα (λ = 1.5418 Å) source.

Electrochemical characterization

Electrochemical measurements were taken on a Biologic VMP3 potentiostat. Both cyclic voltammetry and galvanostatic discharge were conducted in two-terminal, coin-cell format. a–VO_2 electrodes were fabricated by mixing a–VO_2, Super P carbon black (Alfa Aesar), and PVDF binder (Kynar Flex) in an 80:10:10 ratio in N-methyl-2-pyrrolidone (NMP) solvent. This slurry was cast onto an aluminum foil current collector and dried at 120°C under vacuum overnight before testing. The electrolyte used for testing was 1M $NaPF_6$ solvated in a mixture of ethylene carbonate − diethyl carbonate − fluoroethylene carbonate (1:1:0.03 in volume). All testing utilized a glass fiber separator (Whatman GF/D) and a counter/reference electrode of thoroughly cleaned sodium metal (Sigma Aldrich). The mass loading of active material was 1 mg cm^{-2}. All coin cell assembly was performed inside an argon glovebox with both moisture and oxygen levels below 0.5 ppm.

4.3. Results and Discussion

Nanoparticles of vanadium dioxide can be produced through a variety of synthesis techniques including chemical and physical vapor deposition, sol-gel, sputtering, and pulsed-lased deposition.[30] In this work, we utilize a simple precipitation route from aqueous $VOSO_4$ solution to control the oxidation state of vanadium (Figure 4.3.). We found that by beginning with a precursor of V^{4+} and utilizing a low-temperature synthesis that we could suppress the formation of V^{5+}. After dissolution of $VOSO_4 \cdot xH_2O$ in water, ammonium bicarbonate was added as a pH control agent to stabilize the formation of amorphous vanadium oxyhydroxide (Figure

4.4).[31–33] We confirm the lack of structure using X-ray diffraction (XRD) in Figure 4.4b as well as the oxidation state of the vanadium using X-ray photoelectron spectroscopy (XPS) in Figure 4.4c. The peaks in XPS at 516.4 eV and 523.7 eV correspond to the $V2p_{3/2}$ and $V2p_{1/2}$ peaks for V^{4+}, respectively.[34] Additionally, the peaks at 530 eV and 531 eV correspond to vanadium–oxygen and vanadium–hydroxide bonds, respectively.[34–36] In agreement with previous literature (Figure 4.5), heat treatment at 275°C in argon atmosphere subsequently produced a–VO_2. Careful consideration should be taken for the heat-treatment temperature and atmosphere as VO_2 crystallizes around 400°C, will oxidize in air above 300°C, and will not decompose from $VO(OH)_2$ until at least 250°C.[32,37,38]

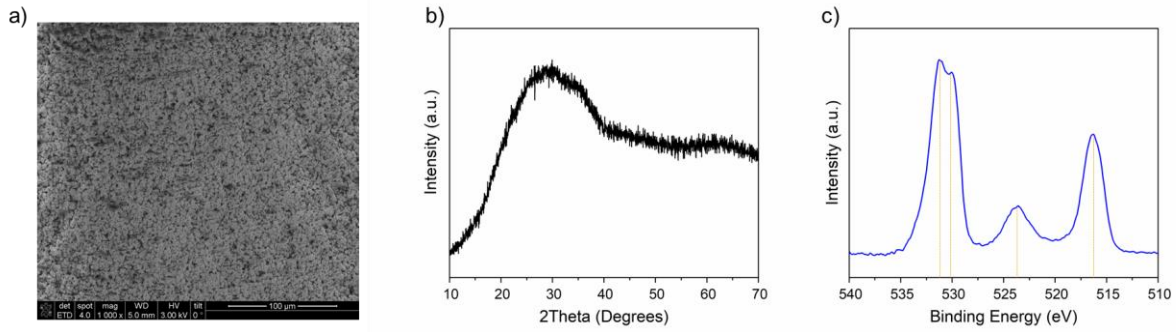

Figure 4.4. a) Scanning electron microscopy (SEM) **b)** X-ray diffraction (XRD) and **c)** X-ray photoelectron spectroscopy (XPS) of amorphous $VO(OH)_2$ powder.

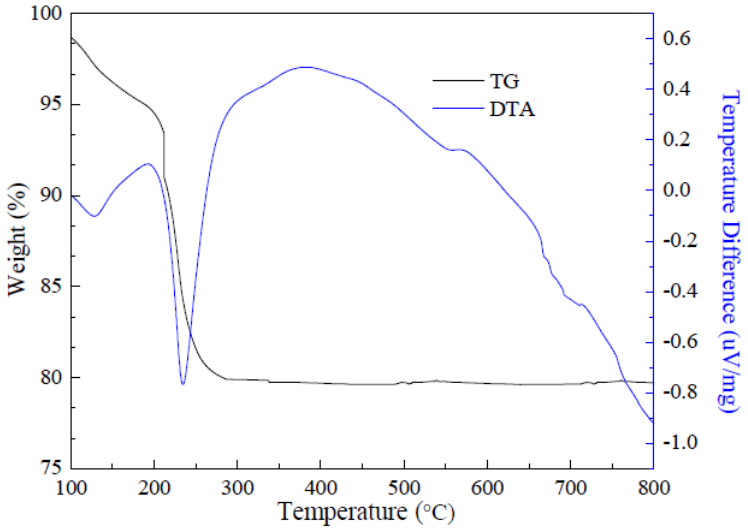

Figure 4.5. Thermogravimetric analysis (TG) and differential thermal analysis (DTA) of amorphous $VO(OH)_2$ in argon atmosphere.[32]

The XRD results for a–VO_2 can be seen in Figure 4.6.a) and display only broad peaks corresponding to the sample holder. For comparison, the XRD results for commercial vanadium pentoxide and hydrothermally-synthesized, crystalline VO_2(B) are included in panels b) and c). All samples were compared with nonnormalized intensity in panel d). Based on these data, we can confirm that a–VO2 is amorphous.

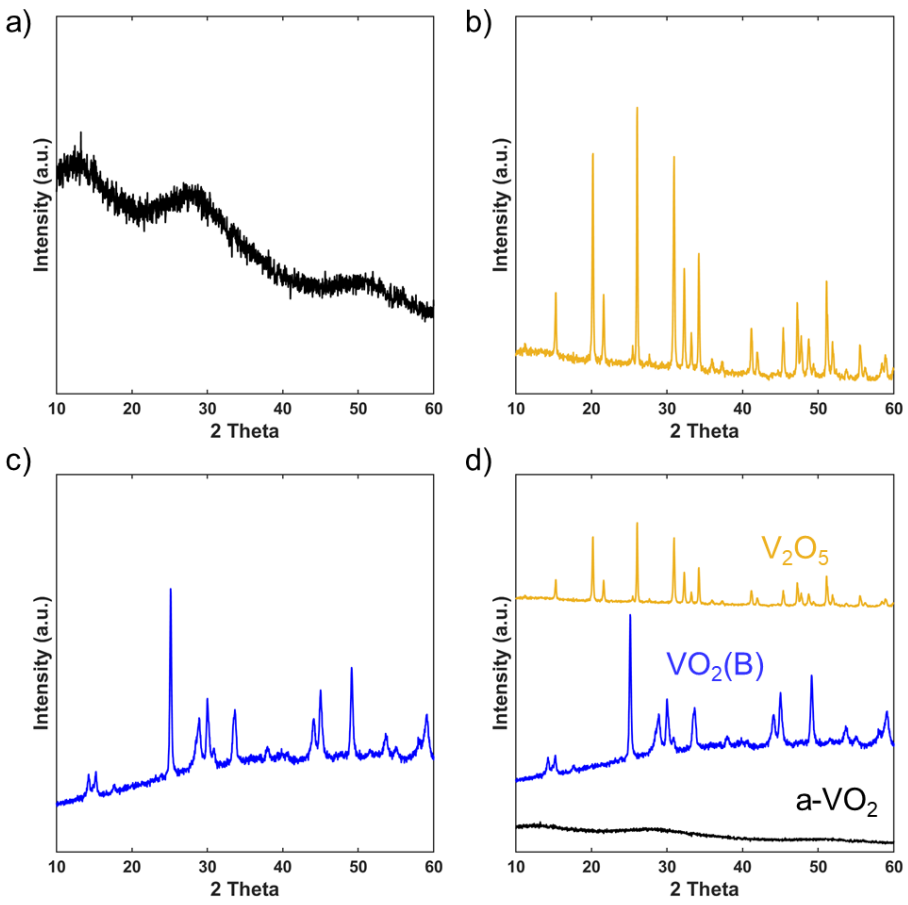

Figure 4.6. X-ray diffraction data for **a)** amorphous vanadium dioxide **b)** commercial vanadium pentoxide **c)** hydrothermally-synthesized VO_2(B) **d)** and all three samples VO_x for intensity comparison.

We investigate the oxidation state of vanadium in a–VO_2 using XPS in Figure 4.7. Careful procedures were taken to process the XPS data properly including measuring the V2p and O1s spectra simultaneously, calibrating peak position to the O 1s peak at 530 eV as opposed to adventitious carbon at 284.8 eV, and using peak separation as well as position to determine the identity of vanadium oxidation.[34] Scanning electron microscopy (SEM) and transmission electron microscopy (TEM) evaluate the morphology of a–VO_2 in Figure 4.4. b), c)

and reveal a primary particle size of approximately 100 nm and plate-like morphology. Electron diffraction measurements taken with TEM exhibit show broad, diffuse diffraction rings which further confirm the amorphous nature of a–VO_2.[39]

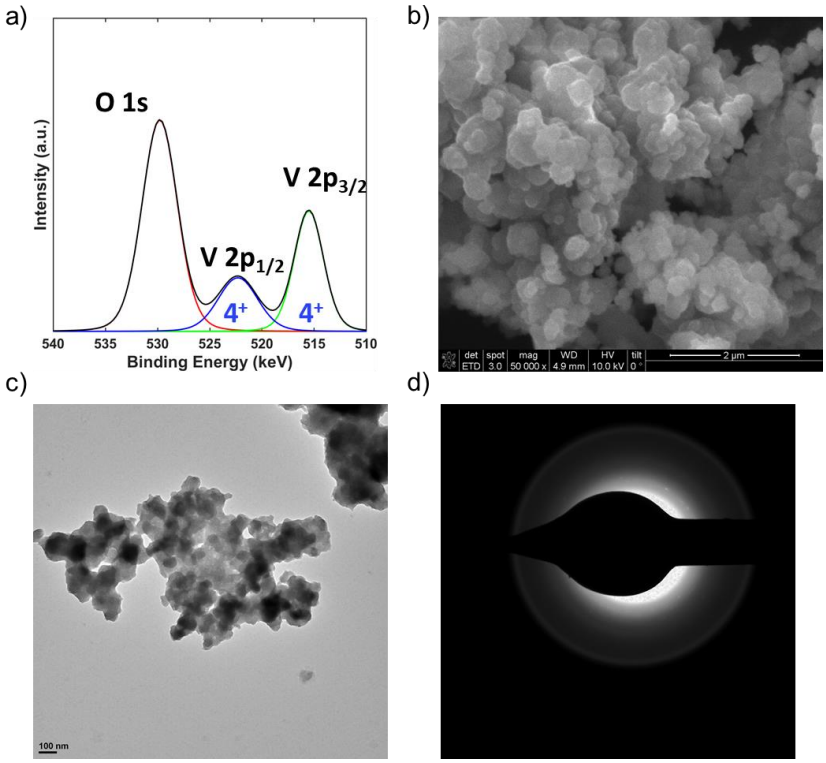

Figure 4.7. Chemical and structural analysis of a-VO_2. **a)** Overlapping V2p and O1s regions of X-ray photoelectron spectroscopy **b)** scanning electron microscopy (scale bar 2 µm) **c)** transmission electron microscopy (scale bar 100 nm) and **d)** electron diffraction.

Both galvanostatic discharge and cyclic voltammetry (CV) measurements were utilized to assess the charge-storage properties of a–VO_2 (Figure 4.8.). a–VO_2 stored an impressively high 275 mAh g^{-1} of sodium at a slow current rate of 40 mA g^{-1}. Based on the quasi box-like shape of the voltammograms (Figure 4.8b), we also investigated the pseudocapacitive nature of a–VO_2.

The current response (*i*) in a cyclic voltammetry experiment can be described as a power-law function of the sweep rate (v) where a is *a* constant and *b* is the power-law exponent:[24,40]

$$i(v) = av^b$$ **Equation 4.1.**

Here, the b-value is used to describe the charge-storage mechanism in materials and is extracted from plots of log(*i*) vs log(v). Redox reactions which are diffusion-limited follow the Randles-Sevcik equation and their current is proportional to the square root of sweep rate, providing a b-value of 0.5.[41,42] In contrast, materials which store charge purely capacitively will exhibit a b-value of 1. Pseudocapacitive materials will similarly show b-values near 1 because their Faradaic reactions are limited to the surface or near surface of the material and are not diffusionally-limited.[43] In this case, we observe a b-value of 0.68 and 0.70 for the oxidation and reduction peaks, respectively which suggests a mixture of diffusion-controlled and surface-controlled reactions.[44,45]

Appendix A details a parallel investigation of a–VO_2 which has been grown onto a graphene foam scaffold through hydrothermal synthesis. In this work, we observe unprecedented capacity and rate retention for a–VO_2 due to a combination of the reduced nanosheet dimensions and the pseudocapacitive charge storage mechanism. Interestingly, the

a–VO_2 grown on graphene foams exhibits a more symmetrical CV (Figure A.3.) as well as a b-value of 0.93.

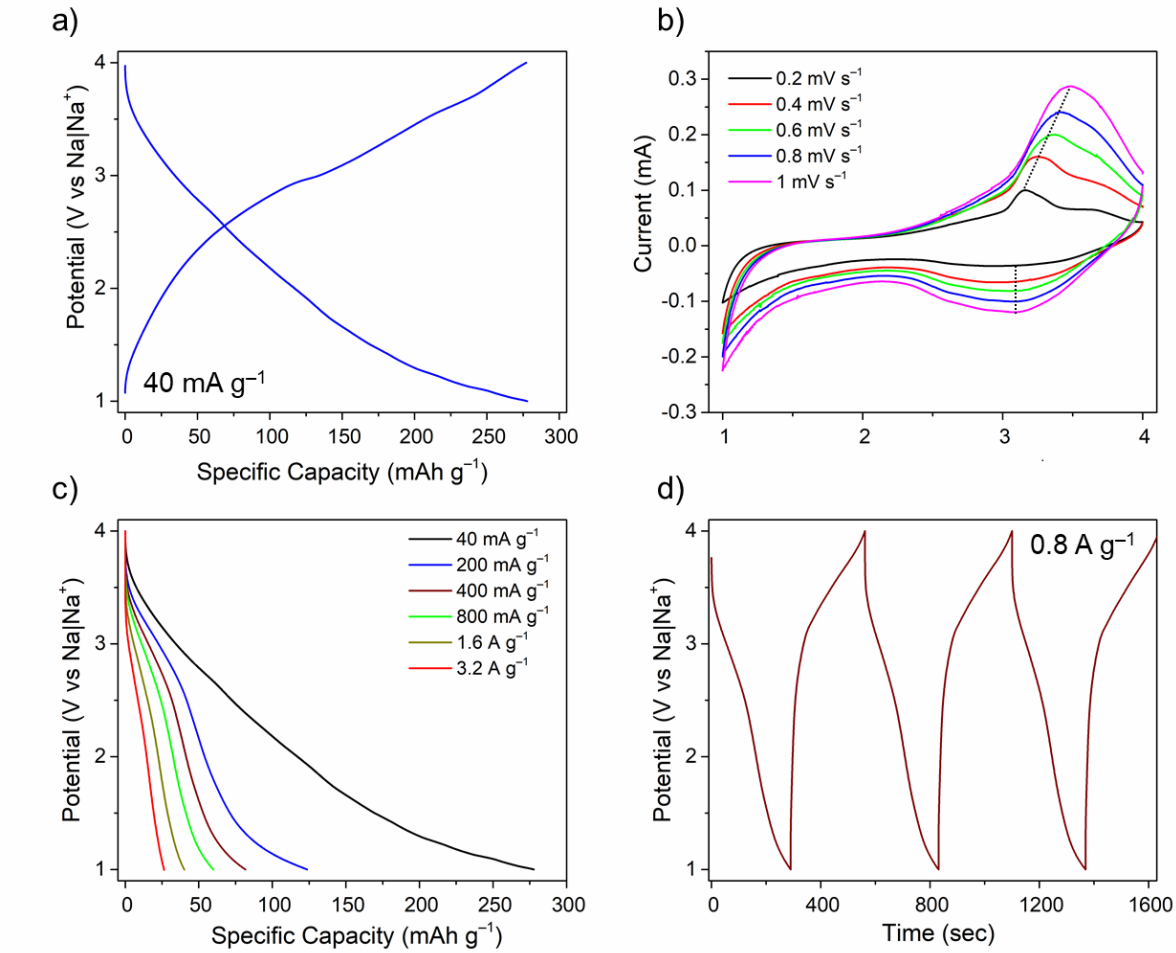

Figure 4.8. Electrochemical performance of a–VO_2 as a sodium-ion battery electrode. **a)** Slow galvanostatic charging/discharging at 40 mA g^{-1} **b)** cyclic voltammetry for b-value analysis **c)** rate retention and **d)** voltage–time curves at 800 mA g^{-1}.

The rate retention of pristine a–VO_2 (Figure 4.8c) shows a sharp decrease in discharge capacity with increasing current density. At the slowest rate (40 mA g^{-1}), a–VO_2 can store nearly 300 mAh g^{-1} in roughly seven hours, but this reduces dramatically to under 100 mAh g^{-1} at 400

mA g^{-1}. These data suggest that the decreased dimension of the a–VO_2 nanosheets in Appendix A store not only more charge than their pristine counterpart here, but also that kinetics are surface-controlled. This becomes more pronounced when comparing the rate retention for a–VO_2 grown on graphene (Figure A.3e,f) and pristine a–VO_2 (Figure 4.9) in both cathodic and anodic windows. Both windows can support ~70 mAh g^{-1} in pristine a–VO_2 which is nearly tripled for the same rate when grown onto graphene foam.

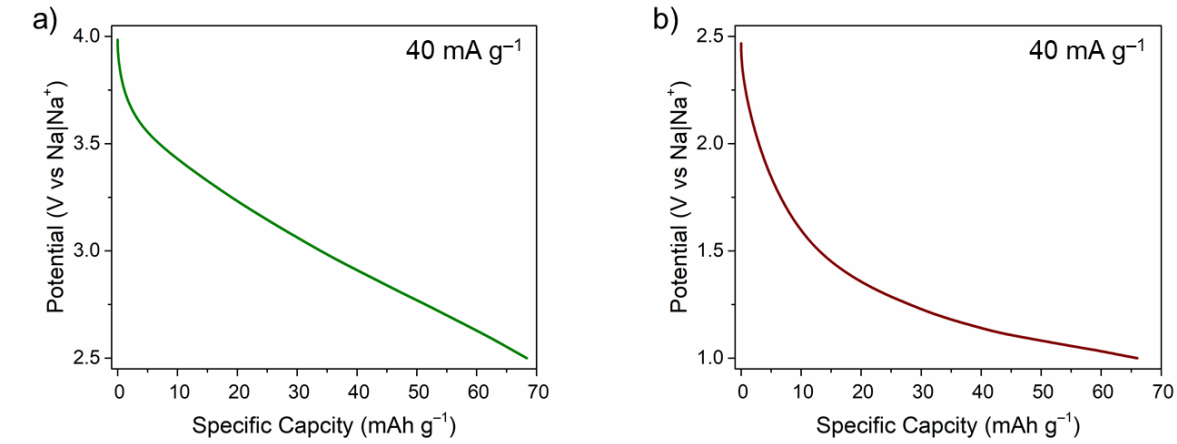

Figure 4.9. Slow galvanostatic cycling for a–VO_2 in its **a)** high-voltage regime (4V–2.5V vs $Na|Na^+$) and **b)** low voltage regime (2.5V–1V vs $Na|Na^+$).

As a proof-of-concept, solid-state device, we employ the glyme-based pseudosolid electrolyte from Chapter 3 of this dissertation with a–VO_2 cathode and sodium metal anode. As demonstrated in Figure 4.10, a-VO_2 only stores about 100 mAh g^{-1} at a low current density of 40 mA g^{-1}. This may be due to wettability issues with the solid electrolyte or, more likely, due to dissolution of vanadium from the active material. This has been found to be an issue with other

vanadium-based compounds in glyme electrolyte[46] and is further substantiated by the consistent fade in capacity seen between cycle 1 and cycle 30.

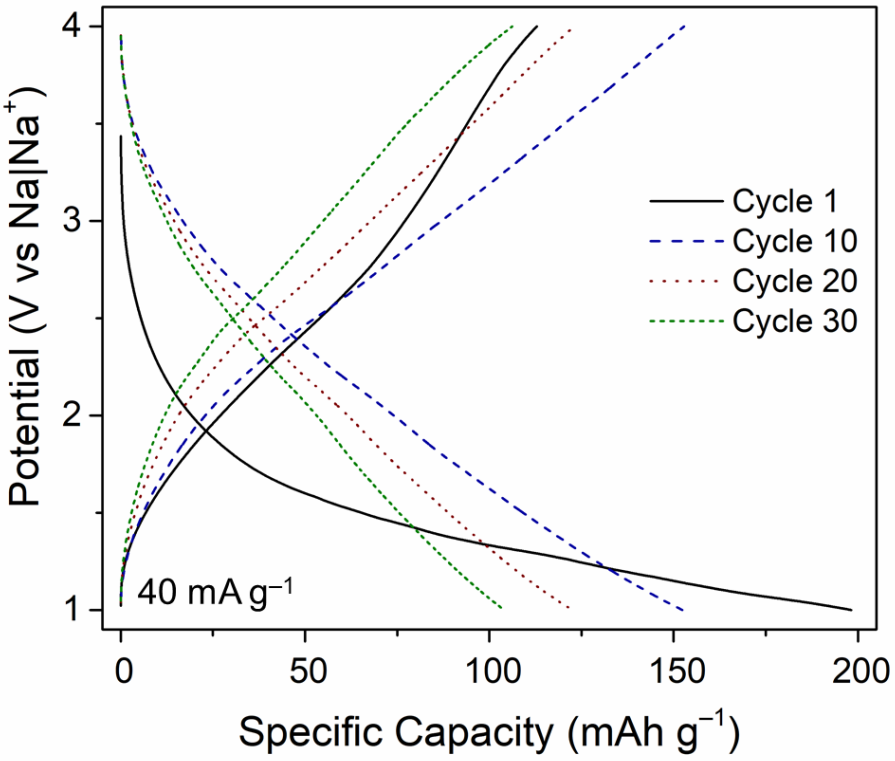

Figure 4.10. Slow galvanostatic cycling (40 mA g^{-1}) of a–VO_2 with glyme-based gel electrolyte and sodium metal counter/reference electrode.

Table 4.1 compares our work to other vanadium dioxide materials for sodium-ion batteries in literature. Through utilization of the wide 4V window of a–VO_2 grown on graphene foam (Appendix A) as two separate cathodic and anodic electrodes, we fabricate a symmetric battery which is capable of an outstanding 63 Wh kg^{-1} at a power density of 3.3 kW kg^{-1}. In

addition, the device is capable of severe overcharging and electrode inversion which could be a significant safety feature in a full-cell device.

Table 4.1. Comparison of sodium-ion storage in vanadium dioxide materials.

Phase	Current density: capacity	Voltage range (vs $Na\|Na^+$)	Loading (mg cm^{-2})	Reference
Amorphous VO_2	40 mA g^{-1}: 275 mAh g^{-1}	1-4 V	1.0	This work
Amorphous VO_2	40 mA g^{-1}: 400 mAh g^{-1}	1-4 V	0.8	Appendix A
VO_2(A)	50 mA g^{-1}: 125 mAh g^{-1}	1-4 V	0.42	47
VO_2(B)	65 mA g^{-1}: 325 mAh g^{-1}	1.5-3.5 V	2.5	48
VO_2(B)	100 mA g^{-1}: 300 mAh g^{-1}	1.5-3.5 V	0.6	49
VO_2(B)	50 mA g^{-1}: 150 mAh g^{-1}	1.5-4 V	N/A	50
VO_2(B)	60 mA g^{-1}: 250 mAh g^{-1}	0.25-3 V	N/A	51
VO_2(B)	100 mA g^{-1}:	0-3 V	N/A	52

	350 mAh g^{-1}			
VO_2(B)	140 mA g^{-1}: 175 mAh g^{-1}	1-3.8 V	N/A	[53]
VO_2(B)	50 mA g^{-1}: 250 mAh g^{-1}	1.5-3.5V	0.3-1	[54]

4.4. Conclusions

Amorphous VO_2 (a–VO_2) was explored as an electrode material for sodium-ion batteries. A low-temperature, facile process produces a-VO_2 with no impurities or V^{5+} surface oxide. Galvanostatic discharges tests exhibit a high capacity of 275 mAh g^{-1} at 40 mA g^{-1}. We analyze the electrochemical properties of pristine a-VO_2 and compare it to a–VO_2 grown on graphene foam (demonstrated in Appendix A). The promising features of amorphous vanadium dioxide showcase the potential of disordered materials for both sodium-ion storage and ion-storage in general.

4.5. References

1. Dunn, B., Kamath, H. & Tarascon, J.-M. Electrical Energy Storage for the Grid: A Battery of Choices. *Science* **334**, 928–935 (2011).
2. Luo, J. *et al.* Pillared Structure Design of MXene with Ultralarge Interlayer Spacing for High-Performance Lithium-Ion Capacitors. *ACS Nano* **11**, 2459–2469 (2017).
3. Cheng, Q. *et al.* Graphene-Like-Graphite as Fast-Chargeable and High-Capacity Anode Materials for Lithium Ion Batteries. *Sci Rep* **7**, 14782 (2017).
4. Peng, L., Zhu, Y., Chen, D., Ruoff, R. S. & Yu, G. Two-Dimensional Materials for Beyond-Lithium-Ion Batteries. *Adv. Energy Mater.* **6**, 1600025 (2016).
5. Chayambuka, K., Mulder, G., Danilov, D. L. & Notten, P. H. L. Sodium-Ion Battery Materials and Electrochemical Properties Reviewed. *Adv. Energy Mater.* **8**, 1800079 (2018).
6. Sawicki, M. & Shaw, L. L. Advances and challenges of sodium ion batteries as post lithium ion batteries. *RSC Adv.* **5**, 53129–53154 (2015).
7. Chen, L. *et al.* Readiness Level of Sodium-Ion Battery Technology: A Materials Review. *Adv. Sustainable Syst.* **2**, 1700153 (2018).
8. Robertson, J. Properties and doping limits of amorphous oxide semiconductors. *Journal of Non-Crystalline Solids* **358**, 2437–2442 (2012).
9. Leenheer, A. J. *et al.* General mobility and carrier concentration relationship in transparent amorphous indium zinc oxide films. *Phys. Rev. B* **77**, 115215 (2008).
10. Nomura, K. *et al.* Amorphous Oxide Semiconductors for High-Performance Flexible Thin-Film Transistors. *Jpn. J. Appl. Phys.* **45**, 4303–4308 (2006).
11. Li, H. B. *et al.* Amorphous nickel hydroxide nanospheres with ultrahigh capacitance and energy density as electrochemical pseudocapacitor materials. *Nat Commun* **4**, 1894 (2013).

12. Li, H., Gao, Y., Wang, C. & Yang, G. A Simple Electrochemical Route to Access Amorphous Mixed-Metal Hydroxides for Supercapacitor Electrode Materials. *Adv. Energy Mater.* **5**, 1401767 (2015).

13. *Physical Properties of Amorphous Materials*. (Springer US, 1985). doi:10.1007/978-1-4899-2260-1.

14. Electronic Properties of Materials. in *Electronic Materials Science* 229–267 (John Wiley & Sons, Inc., 2005). doi:10.1002/0471711640.ch10.

15. Yan, S. *et al.* Research Advances of Amorphous Metal Oxides in Electrochemical Energy Storage and Conversion. *Small* 1804371 (2018) doi:10.1002/smll.201804371.

16. Huang, H. *et al.* Nano-Sized Structurally Disordered Metal Oxide Composite Aerogels as High-Power Anodes in Hybrid Supercapacitors. *ACS Nano* **12**, 2753–2763 (2018).

17. Song, Y. *et al.* Amorphous Mixed-Valence Vanadium Oxide/Exfoliated Carbon Cloth Structure Shows a Record High Cycling Stability. *Small* **13**, 1700067 (2017).

18. Uchaker, E. *et al.* Better than crystalline: amorphous vanadium oxide for sodium-ion batteries. *J. Mater. Chem. A* **2**, 18208–18214 (2014).

19. Sauerteig, D., Ivanov, S., Reinshagen, H. & Bund, A. Reversible and irreversible dilation of lithium-ion battery electrodes investigated by in-situ dilatometry. *Journal of Power Sources* **342**, 939–946 (2017).

20. Mathew, V. *et al.* Amorphous iron phosphate: potential host for various charge carrier ions. *NPG Asia Materials* **6**, e138–e138 (2014).

21. Wang, D., Liu, L., Sun, X. & Sham, T.-K. Observation of lithiation-induced structural variations in TiO_2 nanotube arrays by X-ray absorption fine structure. *J. Mater. Chem. A* **3**, 412–419 (2015).

22. Wang, Z., Wang, Z., Liu, W., Xiao, W. & Lou, X. W. (David). Amorphous $CoSnO_3$ @C nanoboxes with superior lithium storage capability. *Energy Environ. Sci.* **6**, 87–91 (2013).

23. Nai, J. *et al.* Efficient Electrocatalytic Water Oxidation by Using Amorphous Ni-Co Double Hydroxides Nanocages. *Adv. Energy Mater.* **5**, 1401880 (2015).

24. Choi, C. *et al.* Achieving high energy density and high power density with pseudocapacitive materials. *Nat Rev Mater* **5**, 5–19 (2020).

25. Giorgetti, M. & Stievano, L. X-Ray Absorption Spectroscopy Study of Battery Materials. in *X-ray Characterization of Nanostructured Energy Materials by Synchrotron Radiation* (eds. Khodaei, M. & Petaccia, L.) (InTech, 2017). doi:10.5772/66868.

26. Matsuyama, T. *et al.* Structure analyses using X-ray photoelectron spectroscopy and X-ray absorption near edge structure for amorphous MS3 (M: Ti, Mo) electrodes in all-solid-state lithium batteries. *Journal of Power Sources* **313**, 104–111 (2016).

27. Wang, H., Isobe, J., Matsumura, D. & Yoshikawa, H. In situ X-ray absorption fine structure studies of amorphous and crystalline polyoxovanadate cluster cathodes for lithium batteries. *J Solid State Electrochem* **22**, 2067–2071 (2018).

28. Xiong, H., Slater, M. D., Balasubramanian, M., Johnson, C. S. & Rajh, T. Amorphous TiO_2 Nanotube Anode for Rechargeable Sodium Ion Batteries. *J. Phys. Chem. Lett.* **2**, 2560–2565 (2011).

29. Chae, O. B. *et al.* Reversible Lithium Storage at Highly Populated Vacant Sites in an Amorphous Vanadium Pentoxide Electrode. *Chemistry of Materials* **26**, 5874–5881 (2014).

30. Nag, J. & Haglund Jr, R. F. Synthesis of vanadium dioxide thin films and nanoparticles. *J. Phys.: Condens. Matter* **20**, 264016 (2008).

31. Shi, J., Zhou, S., You, B. & Wu, L. Preparation and thermochromic property of tungsten-doped vanadium dioxide particles. *Solar Energy Materials and Solar Cells* **91**, 1856–1862 (2007).

32. Ma, Y. *et al.* Preparation of Vanadium Oxides from a Vanadium (IV) Strip Liquor Extracted from Vanadium-Bearing Shale Using an Eco-Friendly Method. *Metals* **8**, 994 (2018).

33. Chen, M. *et al.* PVP-assisted hydrothermal synthesis of VO(OH)2 nanorods for supercapacitor electrode with excellent pseudocapacitance. *Materials Letters* **227**, 217–220 (2018).

34. Mendialdua, J., Casanova, R. & Barbaux, Y. XPS studies of V2O5, V6O13, VO2 and V2O3. *Journal of Electron Spectroscopy and Related Phenomena* **71**, 249–261 (1995).

35. Demeter, M., Neumann, M. & Reichelt, W. Mixed-valence vanadium oxides studied by XPS. *Surface Science* **454–456**, 41–44 (2000).

36. Rameshan, C., Ng, M. L., Shavorskiy, A., Newberg, J. T. & Bluhm, H. Water adsorption on polycrystalline vanadium from ultra-high vacuum to ambient relative humidity. *Surface Science* **641**, 141–147 (2015).

37. Baudrin, E., Sudant, G., Larcher, D., Dunn, B. & Tarascon, J.-M. Preparation of Nanotextured VO_2 [B] from Vanadium Oxide Aerogels. *Chem. Mater.* **18**, 4369–4374 (2006).

38. Fu, G., Polity, A., Volbers, N. & Meyer, B. K. Annealing effects on VO2 thin films deposited by reactive sputtering. *Thin Solid Films* **515**, 2519–2522 (2006).

39. Wu, H., Li, M., Zhong, L., Luo, Y. Y. & Li, G. H. Electrochemical Synthesis of Amorphous VO_2 Colloids and Their Rapid Thermal Transforming to VO_2 (M) Nanoparticles with Good Thermochromic Performance. *Chem. Eur. J.* **22**, 17627–17634 (2016).

40. Lindström, H. *et al.* Li^+ Ion Insertion in TiO_2 (Anatase). 1. Chronoamperometry on CVD Films and Nanoporous Films. *J. Phys. Chem. B* **101**, 7710–7716 (1997).

41. Randles, J. E. B. A cathode ray polarograph. Part II.—The current-voltage curves. *Trans. Faraday Soc.* **44**, 327–338 (1948).

42. Ševčík, A. Oscillographic polarography with periodical triangular voltage. *Collection of Czechoslovak Chemical Communications* **13**, 349–377 (1948).

43. Brousse, T., Bélanger, D. & Long, J. W. To Be or Not To Be Pseudocapacitive? *J. Electrochem. Soc.* **162**, A5185–A5189 (2015).

44. Lai, C. (Matt) *et al.* Designing the Charge Storage Properties of Li-Exchanged Sodium Vanadium Fluorophosphate for Powering Implantable Biomedical Devices. *Adv. Energy Mater.* **9**, 1900226 (2019).

45. Lesel, B. K., Cook, J. B., Yan, Y., Lin, T. C. & Tolbert, S. H. Using Nanoscale Domain Size To Control Charge Storage Kinetics in Pseudocapacitive Nanoporous $LiMn_2O_4$ Powders. *ACS Energy Letters* **2**, 2293–2298 (2017).

46. Westman, K. Diglyme as an electrolyte solvent for sodium-ion batteries. (2016).

47. Hu, X. *et al.* VO2 (A)/graphene nanostructure: Stand up to Na ion intercalation/deintercalation for enhanced electrochemical performance as a Na-ion battery cathode. *Electrochimica Acta* **293**, 97–104 (2019).

48. Balogun, M.-S. *et al.* Carbon Quantum Dot Surface-Engineered VO_2 Interwoven Nanowires: A Flexible Cathode Material for Lithium and Sodium Ion Batteries. *ACS Appl. Mater. Interfaces* **8**, 9733–9744 (2016).

49. Chao, D. *et al.* Graphene Quantum Dots Coated VO_2 Arrays for Highly Durable Electrodes for Li and Na Ion Batteries. *Nano Lett.* **15**, 565–573 (2015).

50. Wang, W. *et al.* Single crystalline VO2 nanosheets: A cathode material for sodium-ion batteries with high rate cycling performance. *Journal of Power Sources* **250**, 181–187 (2014).

51. He, G., Li, L. & Manthiram, A. VO_2 /rGO nanorods as a potential anode for sodium- and lithium-ion batteries. *J. Mater. Chem. A* **3**, 14750–14758 (2015).

52. Yan, B. *et al.* Superior sodium storage of novel VO_2 nano-microspheres encapsulated into crumpled reduced graphene oxide. *J. Mater. Chem. A* **5**, 4850–4860 (2017).

53. Mahadi, N. B. *et al.* Vanadium dioxide – Reduced graphene oxide composite as cathode materials for rechargeable Li and Na batteries. *Journal of Power Sources* **326**, 522–532 (2016).

54. Wei, T., Li, Q., Yang, G. & Wang, C. Towards highly stable Li/Na-ion batteries based on vertically aligned VO2 nanobelt arrays. *Journal of Alloys and Compounds* **827**, 154276 (2020).

Chapter 5: Summary and Future Direction

The sodium-ion battery (SIB), due to its lower cost and more abundant components, is a promising alternative technology to the well-known lithium-ion battery (LIB). Although LIBs and SIBs are similar in their chemistry, sodium-ion batteries face unique challenges which require appropriately-tailored solutions. This dissertation details various approaches to address these issues through the introduction and implementation of novel electrolyte and electrode systems.

Flammability of common electrolyte materials remains a large issue for the continued commercialization of energy-dense battery systems into consumer products. To meet this need for nonflammable electrolytes, we synthesize and characterize sol-gel-derived, pseudosolid electrolytes. In Chapter 2, we investigate the use of an ionogel electrolyte in which nonvolatile ionic liquid is encapsulated within an organically-modified silica matrix. We establish the cyclability of our ionogel electrolyte with common electrode materials such as activated carbon, sodium vanadium phosphate, and sodium titanium phosphate. In a broader context, this demonstration provides one possible route for utilization of solid electrolytes which are regarded as the next big innovation for batteries. Unlike traditional solid electrolytes which are typically too resistive, we retain liquid-like kinetics in a macroscopic solid through the use of a silica scaffold. In conjunction with our organic modification for durability, ionogel electrolytes are a promising solution which combines the safety of a solid with the dynamics of a liquid. Future progress on reducing the thickness of the ionogel monoliths through spin-coating would enable further increases in energy density.

In Chapter 3, we adapt the ionogel synthesis to instead encapsulate a tetraglyme-based liquid electrolyte which is stable against sodium metal. Not only are they cheap and versatile, glyme solvents of higher molecular weight also exhibit negligible vapor pressure similar to ionic liquid. Due to their outstanding stability and low cycling overpotential with sodium metal, these

glyme-based gel electrolytes allow for the direct use of sodium metal as an anode. Boasting a theoretical capacity over 3x greater than graphite, the utilization of a sodium metal anode can significantly improve the energy density of an SIB. We demonstrate a prototype cell of 450 Wh kg^{-1} with sodium vanadium fluorophosphate cathode, sodium anode, and our nonflammable, glyme-based gel electrolyte. An energy density this high competes with state-of-the art LIB systems which utilize volatile liquid electrolytes. By being both cost-effective and electrochemically-stable, this glyme-based gel electrolytes establishes a scalable direction for nonflammable sodium-ion batteries. To advance this work further, progress should be made in creating thinner electrolytes which will increase both energy density and power density at the cell level.

Due to the larger size of the sodium cation, different materials and architectures must be employed to match or exceed performance of LIBs. To avoid the difficulty of fitting the larger sodium ion between well-defined, crystallographic features (tunnels, layers, etc.), we explore the possibility of using an amorphous material as an ion host. In Chapter 4, amorphous vanadium dioxide (a–VO_2) is presented as a potential sodium-ion electrode. Pristine a–VO_2 demonstrates a high capacity at slow rates and voltammetric features reminiscent of a pseudocapacitive material. When grown on graphene foam in Appendix A, the capacity, rate capability, and contribution from surface-controlled reactions improves dramatically. Although the performance of a–VO_2 is impressive, the important takeaway from this work is possibility for future amorphous electrode materials which could unlock new potential for energy storage materials, especially for larger ions (Na^+, K^+, Ca^{2+}, Zn^{2+}, Al^{3+}, etc.). As X-ray absorption techniques become more available and advanced, the capability of understanding amorphous materials, especially through in-situ experiments, increasing tremendously.

Appendix A: Unleashing the Power of Symmetric Energy Storage with Reborn Pseudocapacitance

***a version of this dissertation appendix is in preparation as a manuscript thanks to work in collaboration with Dongliang Chao, Chun-Han (Matt) Lai, Qiulong Wei, Changrong (Rose) Zhu, Hong Jin Fan, and Bruce Dunn*

Pseudocapacitive charge storage materials is distinguished from other types of electrochemical energy storage by fast charging and high power capabilities. One candidate pseudocapacitive material is monoclinic VO_2 (B), a layered compound with high theoretical capacity and rich chemistry of various vanadium valence states. VO_2 research has thus far focused on the crystalline rather than the amorphous phase, despite the impressive electrochemical properties of the latter, which includes an improved pseudocapacitive behavior due to disorder. Here we demonstrate linear voltage profile over a 3-volt range with high reversible capacity. As a result, a full symmetric battery with both cathodic and anodic pseudocapacitance is constructed showing fast charge/discharge rate in one minute and unleashed energy/power output. This pseudocapacitive based symmetric battery enabled by amorphous material provides new avenues for designing next-generation safer power devices.

A.1. Introduction

Pseudocapacitive materials have emerged as an interesting direction for energy storage materials. While there is some discussion about specific features which distinguish pseudocapacitive materials, there seems to be general agreement that these materials may offer the elusive characteristic of achieving high energy at high rates of operation.[1, 2, 3] The

overwhelming trend for the studies on pseudocapacitive materials has been to investigate Li^+ insertion into crystalline solids. The most common systems operate between 2.5 and 1.0 V vs. Li^+/Li (*ref.* [4, 5, 6]). Finding pseudocapacitive materials at higher voltages has been difficult and only recently researchers seemed to uncover possible materials in the range of 4.0V (*ref.* [7]).

The present paper concerns the electrochemical properties of VO_2. Crystalline VO_2 is one of the most well-studied transition metal oxides, largely because of the metal-semiconductor transition that it goes through at ~70°C (*ref.* [8]). The ion insertion properties of this material, however, have received much less attention. The crystalline form of VO_2 which is of most interest is VO_2 (B), a layered structure formed from edge-sharing VO6 octahedra. The material possesses good room temperature conductivity, rapid ion diffusion, and higher capacity than other vanadium oxides.[9, 10] In Li^+ systems, VO_2 has been studied as both a positive electrode[11, 12, 13] (1.5–3.5 V vs. Li) and a negative electrode[14, 15] (0.01–3.0 V vs. Li). During Li ion insertion, a phase change with obvious discharge plateaus occurs, which limits its rate capability and cycling stability[14]. With Na ions, which have larger ionic sizes than Li ions (1.02 Å for Na^+ *vs.* 0.76 Å for Li^+), lattice accommodation is more diffusion limited, leading to much worse rate performance with limited Na ion insertion. Various approaches have been used to improve the rate performance including forming composites with reduced graphene oxide[16], surface coating by graphene quantum dots[11], and ultrathin nanobelt design[17]. However, the ability to achieve high rate reversibility with Na^+ remains a significant challenge.

In this paper, we show that the Na^+ insertion properties of amorphous VO_2 (a-VO_2) are significantly better than that of VO_2(B). This amorphous material exhibits a linear galvanostatic profile which exists over a wide voltage range (1 to 4V vs. Na/Na^+). This voltage profile is reminiscent of an electrical double layer capacitor (EDLC), except that with VO_2, there are redox reactions which increase the specific capacity significantly. The reversible capacity of over 400

mAh g^{-1} exceeds that of any other Na^+ insertion material, crystalline or amorphous. Because the linear voltage regime encompasses the voltage range for both positive and negative electrodes, this enables us to operate a symmetric sodium-ion battery in which a-VO_2 serves as both the anode and cathode.

A.2. Results and Discussion

Materials Synthesis and Characterization

The two VO_2 materials which are the subject of this study are monoclinic VO_2(B), noted as c-VO_2, and the corresponding amorphous composition (a-VO_2). Both materials are prepared on graphite foam (GF) by solvothermal methods with oxalic acid serving a reducing agent. The synthesis details for both forms of VO_2 are discussed in the Materials and Methods section. While the synthesis methods are similar for both materials, the higher concentration of vanadium precursor leads to a higher nucleation rate and formation of the crystalline VO_2(B). The c-VO_2 tends to form platelets which are about 100 nm thick with a lateral size of 300 to 500 nm (Fig. A.1.a and Supplementary Fig. A.5.). In comparison, the a-VO_2 forms thin sheets which are 5 nm thick with lateral dimensions of 30–60 nm (Fig. A.1.b). The plan view shown in Fig. A.1.a,b underscores the difference in dimensions and shows that both materials are mesoporous. The cross-section of a-VO_2 is shown in Fig. A.1.c a and Supplementary Fig. A.6. The amorphous VO_2 materials grow perpendicular to the graphite foam and form layers in the range of 100 to 150 nm thick. The X-ray diffraction (XRD) patterns in Fig. A.1.d identify the crystalline material as monoclinic VO_2 (B) (JCPDS 31–1438) in combination with the highly crystalline structure of the GF substrate (JCPDS 75–1621). The VO_2 (B) structure is presented in Supplementary Fig. A.5.e. The lattice-resolved HRTEM image shows an interplanar spacing of 2.9 Å for the (400) planes of c-VO_2 (inset in Fig. A.1.d). In addition, the fast Fourier Transform

(FFT) spots reveal the existence of (110) and (200) facets in the [002] zone axis, implying that the layers of c-VO_2 are stacked along the [002] direction[11, 18]. The a-VO_2 material is X-ray amorphous, as only the GF peaks are observed in the XRD (see Fig. A.1.e). The FFT image is consistent with the amorphous structure. X-ray photoelectron spectroscopy (XPS) carried out on the as prepared materials (Fig. A.2.) indicates that in the c-VO_2 all the vanadium is in the +4 state while a-VO_2 has a small amount of V^{3+} present.

The graphite foam serves as both a lightweight three-dimensional porous current collector and a flexible scaffold that maintains structural continuity of the electrode. This electrode enables ion and electron access to the VO_2 active material without the need for binders or conductive additives. The pores facilitate electrolyte penetration to the mesoporous VO_2 layers shown in Fig. A.1. while the GF provides electron conduction. The a-VO_2 loading was 0.8 mg cm^{-2} while that for c-VO2 was 1 mg cm^{-2}.

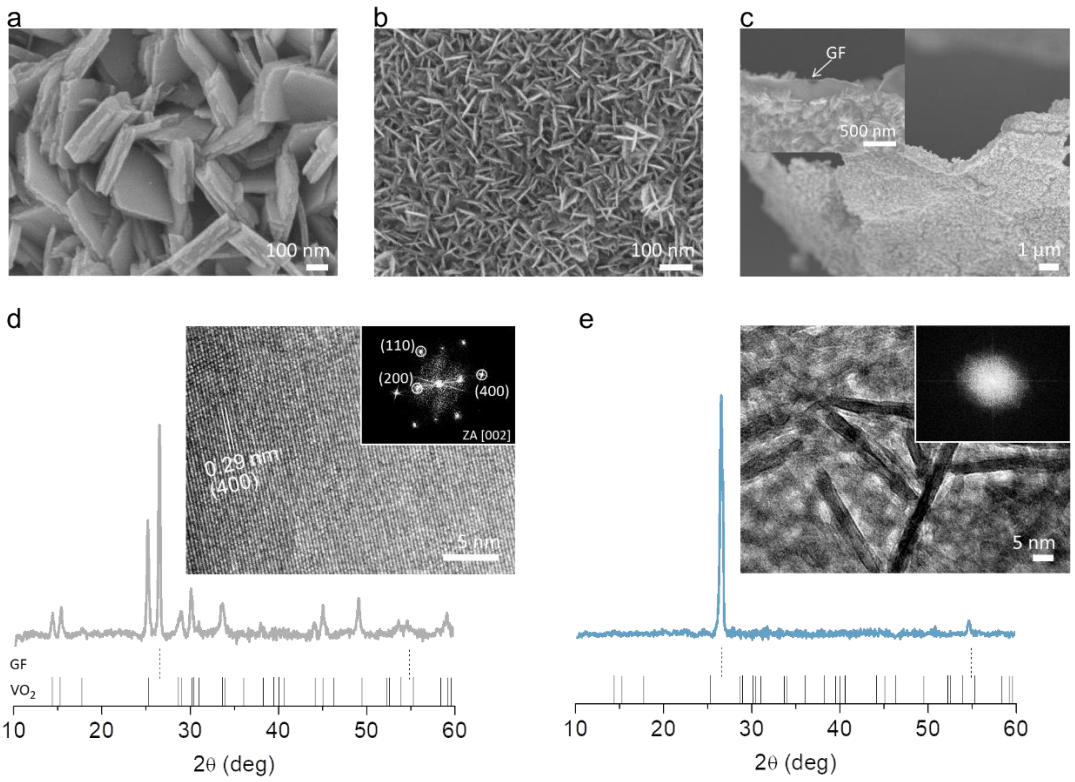

Figure A.1. Structural and morphology characterizations of c-VO_2 and a-VO_2. **a.** Plan view of c-VO_2. **b.** Plan view of a-VO_2. **c**. Cross-section of a-VO_2 on graphite foam. **d.** XRD of c-VO_2 shows that the material corresponds to VO_2 (B). The strong reflection at 26.6^o is from the graphite foam. The inset shows the TEM image with the fast Fourier transform (FFT) pattern. **e.** XRD of a-VO_2 shows only the peaks for the GF. The inset shows the TEM image of the thin plate with the FFT pattern.

Structure and chemistry of Na^+ intercalated VO_2

Reversible Na^+ insertion into both c-VO_2 and a-VO_2 occurs over a wide potential range, from 4.0 to 1.0 V (vs. Na/Na^+). The first three galvanostatic cycles taken at a charge–discharge rate of 0.1 C (40 mA g^{-1}) shows a linear voltage profile with a specific capacity about 400 mAh

g^{-1} (Fig. A.3.a). The slightly greater capacity for the first cycle can likely be attributed to formation of the solid electrolyte interphase (SEI). Since this electrode includes the contribution from graphite, control experiments indicate that between 4.0 and 1.0 V (vs. Na/Na^+), there is only a negligible capacity contribution from the GF (Supplementary Fig. A.7.). To the best of our knowledge, the reversible capacity of over 400 mAh g^{-1} exceeds that for any other Na^+ insertion material. This capacity corresponds to the insertion of ~1.24 Na^+. This value is in good agreement with EDX spectra taken after discharge (Supplementary Fig. A.8.) and is consistent with the Na:V ratio (1.24:1) from XPS results (Fig. A.2.). The XPS measurements upon discharge to 2.5 V indicate a mix of V^{4+} and V^{3+} states, while at 1.0V, only V^{3+} is evident. It should be noted that the XPS measurements were made after the samples had been subjected to Ar etching so that the results are more representative of bulk behavior. Thus, the combination of the EDX and XPS results suggest that Na^+ insertion occurs in the bulk of the material and is not limited to just the surface. Finally, it is important to mention that after 50 cycles, XRD indicates that the amorphous character of a-VO_2 is retained (Supplementary Fig. A.9.).

The c-VO_2 material also undergoes Na^+ insertion over a wide potential range. At the same 0.1C charge-discharge rate, the reversible capacity for the full electrode is ~360 mAh g^{-1} (Supplementary Fig. A.10.). This value is somewhat less than 400 mAh g^{-1} obtained with a-VO_2, but is still quite significant. This capacity implies that the fully charged material has a composition of $Na_{1.10}VO_2$ which is in good agreement with the EDX result (Supplementary Fig. A.8.a). The linear voltage behavior shown in the galvanostatic experiment (Supplementary Fig. A.10.) suggests that there is no phase transition over the 4.0 to 1.0 V range. This is confirmed by *ex situ* XRD measurements for the c-VO_2 over 50 cycles (Supplementary Fig. A.11. and A.12.). The first cycle shows that peak shifts which occur from Na^+ insertion and de-insertion are reversible. The change in lattice parameter between the fully charged and discharged states is ~0.83%, ~0.27%, and ~1.46% expansion for *a*, *b*, and *c*, respectively. This corresponds to a

volume expansion of ~2.1% and establishes that Na^+ insertion and de-insertion are occurring within the bulk material and not at the surface. Although no phase change is observed over 50 cycles, there is a permanent peak shift which can be associated with trapped Na^+, namely, not all Na ions can be extracted after complete cycles (Supplementary Fig. A.11. and A.13.). Based on the lattice parameter shift and the corresponding capacity, we estimate the amount of trapped Na to be ~0.3. This Na trapping is not obvious in the a-VO_2 (absence of Na XPS peak after desodiation in Supplementary Fig. A.13.).

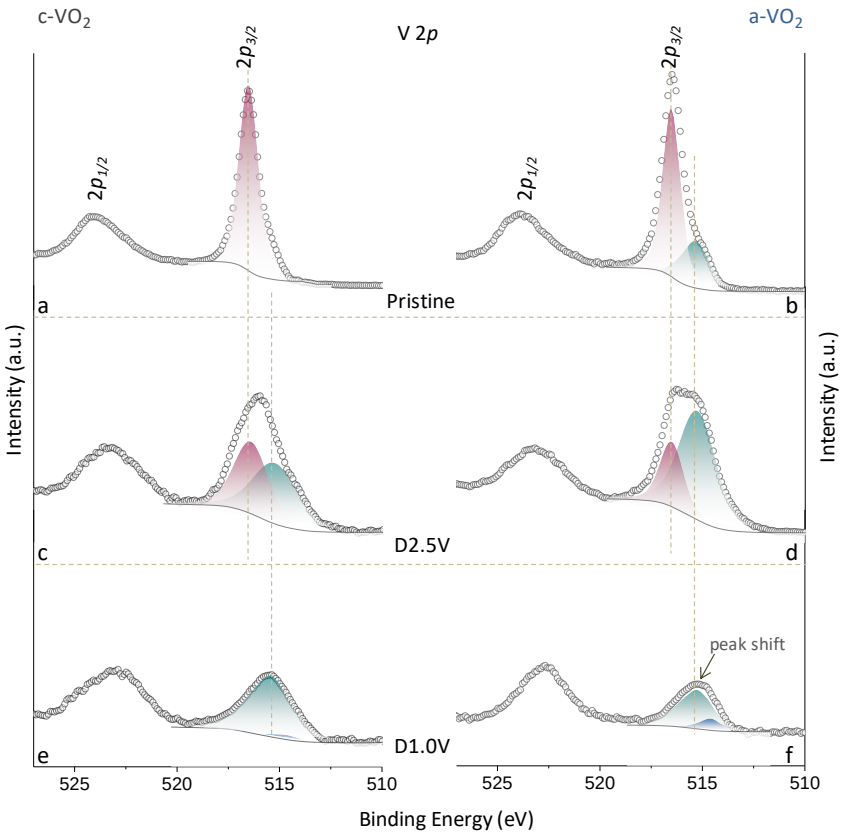

Figure A.2. High-resolution XPS spectra of V *2p* for c-VO_2 and c-VO_2. **a,b)** pristine state of c-VO_2 **(a)** *c*-VO_2 **(b).** c,d) upon discharge to 2.5 V (D2.5 V) of c-VO_2 **(c)** c-VO_2 **(d)**. **e,f)** upon discharge to 1.0 V (D1.0 V) of c-VO_2 **(e)** *c*-VO_2 **(f)**.

Charge storage properties of VO_2

The charge storage properties for both c-VO_2 and a-VO_2 were investigated in the 4.0 to 1.0 V (vs. Na/Na^+) regime as well as in specific voltage regions for positive electrode and negative electrodes. For the 3.0 V voltage span, the quasi-rectangular cyclic voltammetry (CV) curves (Fig. A.3.b) for a-VO_2 are consistent with the linear galvanostatic behavior shown in Fig. A.3.a. These two features are often taken as indications of a pseudocapacitive response[19]. It is significant to note that the triangular voltage-time characteristic for a-VO_2 is analogous to that of

a carbon-based double layer capacitor (Fig. A.3.c). The difference is that energy storage with a-VO_2 arises from redox processes and for a one-minute charge-discharge, the amount is over 10 times greater than that achieved with activated carbon. The current peaks at ~2.0 V in Fig. A.3.b and Supplementary Fig. A.14.a enable one to gain insight regarding the charge storage mechanism as the relationship between peak current (i) and sweep rate (u) is given by a power law relation:

$$i = au^b \quad (1)$$

where a is a constant and b indicates whether the charge storage mechanism is associated with semi-infinite diffusion (b = 0.5) or a surface-controlled or a capacitor-like process (b = 1). The value of b = 0.93 obtained for a-VO_2 below 1 mV s^{-1} suggests that even at slow sweep rates, Na^+ insertion is not controlled by semi-infinite diffusion (Supplementary Fig. A.15.a). An accompanying analysis can be used to determine qualitatively the relative contribution of each charge storage process by considering the current at a given potential to be comprised of each type:

$$i\,(V) = k_1u + k_2u^{1/2} \quad (2)$$

where k_1 and k_2 are the proportionality constants describing the surface or capacitance-controlled currents and diffusion-controlled currents, respectively. This analysis (Fig. A.3.d) indicates that k_1 is ~90% over the entire 3.0 volt range. The corresponding characteristics for c-VO_2 (~60%) indicate that the kinetics have a greater contribution from semi-infinite diffusion processes (Supplementary Fig. A.14.b-d). As a result, the energy storage for a-VO_2 is much greater than that of c-VO_2 at the higher sweep rates (Supplementary Fig. A.15.b). In comparing these results, it is important to note that the high rates of Na^+ insertion are achieved in a system

characterized by lattice disorder and does not depend upon preferred crystallographic pathways.

Two separate series of half-call experiments were carried out with a-VO_2 in order to evaluate this material as both a positive electrode and a negative electrode for sodium-ion batteries. In addition to the high capacity arising from a significant amount of Na^+ insertion, the pseudocapacitor-like behavior shown over the 3.0 volt range suggested that this material might be able to effectively retain its good energy density at high rates of charge and discharge.

The cathodic window (4.0 to 2.5 V vs. Na/Na^+) shows a similar linear voltage response as that in Fig. A.3.a, although this behavior becomes less linear at higher rates. Figure A.3.e shows that the specific capacity is very good at the lower rates (190 mAh g^{-1} at 0.5C), however, this value decreases appreciably to 90 mAh g^{-1} at 60C. At 20C, the slope is quite linear and the capacity of ~125 mAh g^{-1} is retained for some 500 cycles (Supplementary Fig. A.16.a). Similar to the results of Fig. A.3.d, the analysis involved in Eqn. 2 leads to a k_1 value is > 90% for the cathodic window (Supplementary Fig. A.17.). The anodic window (2.5 to 1.0 V vs. Na/Na^+) exhibits comparable behavior (Fig. A.3f) in terms of its linear response at low charge-discharge rates becoming less linear at high rates. The specific energy values range from 210 mAh g^{-1} at 0.5C to ~90 mAh g^{-1} at 60C. Here too, at 20C, the voltage slope is linear and the capacity is ~120 mAh g^{-1} after 500 cycles (Supplementary Fig. A.16.b). The k_1 value is just slightly less than 90%, similar to the results for the cathodic window (Supplementary Fig. A.18). Finally, it is important to note that over 1500 cycles at 60C, the half-cells exhibit only 15% capacity loss (Supplementary Fig. A.19.).

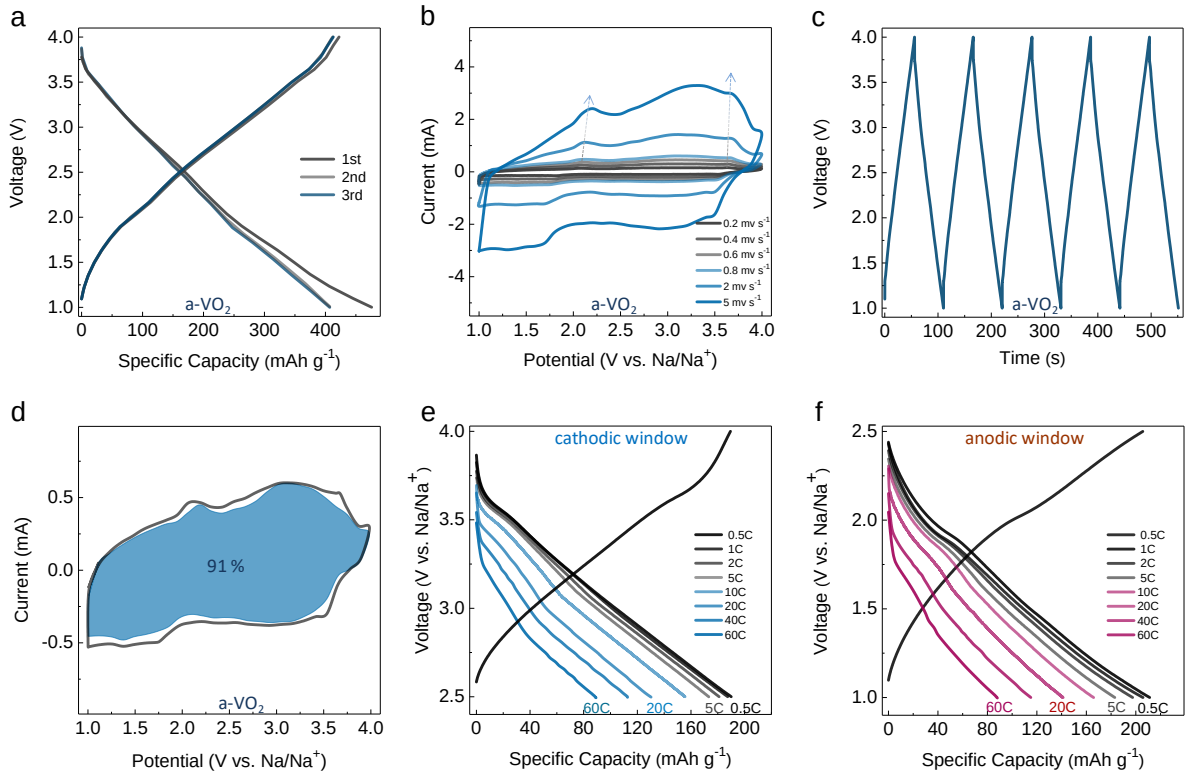

Figure A.3. The charge storage properties for a-VO_2 in the 4.0 to 1.0 V (vs. Na/Na^+) regime as well as in specific voltage regions for positive electrode and negative electrodes. **a)** Initial first three charge/discharge profiles of the a-VO_2 electrode at 0.1C (40 mA g^{-1}). **b)** CV curves at various scan rates from 0.2 to 5 mV s^{-1}. **c)** The triangular charging and discharging over the entire 1 to 4 volt region at 60C and extend for multiple cycles. **d)** Capacitive (shaded area) and diffusion-controlled (cavity area) contribution to charge storage of a-VO_2 at 0.8 mV s^{-1}. e,f) Galvanostatic charge/discharge profiles at different rates from 0.5−60C of a-VO_2 electrode in cathodic **(e)** and anodic **(f)** windows, respectively. 1C is defined as 200 mA g^{-1} in specific cathodic/anodic window.

Symmetric batteries based on amorphous VO_2

Symmetric batteries, where the same active material serves as both anode and cathode, have recently attracted some interest for the following reasons: 1) they can be overcharged and overdischarged to some extent and 2) by using the same material for both electrodes, fabrication costs are expected to be lower[20, 21, 22]. In research to date, symmetric batteries have been based on the bipolar materials having two distinct plateaus, one at high voltage (between 2 and 4 volts vs. the alkali metal of interest) and one at lower voltage (between 0 and 2 volts). The systems reported include $Na_3Ti_2(PO_4)_3$ (*ref.* [22]), $Na_2VTi(PO_4)_3$ (*ref.* [20]), $Na_{0.6}[Cr_{0.6}Ti_{0.4}]O_2$ (*ref.* [23]) and MoS_2 (ref. [24]) which is considered to be 'quasi-symmetric' (*ref.* [24]). Although these systems have demonstrated reversible charge-discharge characteristics, the kinetics are diffusion controlled and the occurrence of phase transitions with these systems often leads to structure changes and poor cycling behavior (see schematics in Fig. A.4.a). The use of a-VO_2 as a bipolar electrode offers a very different approach. The linear response under galvanostatic conditions means that phase changes are avoided, and that charge and discharge are the result of only Na^+ insertion and de-insertion processes. Moreover, the high rate capability associated with the pseudocapacitive nature of these materials can be exploited (Fig. A.4.a).

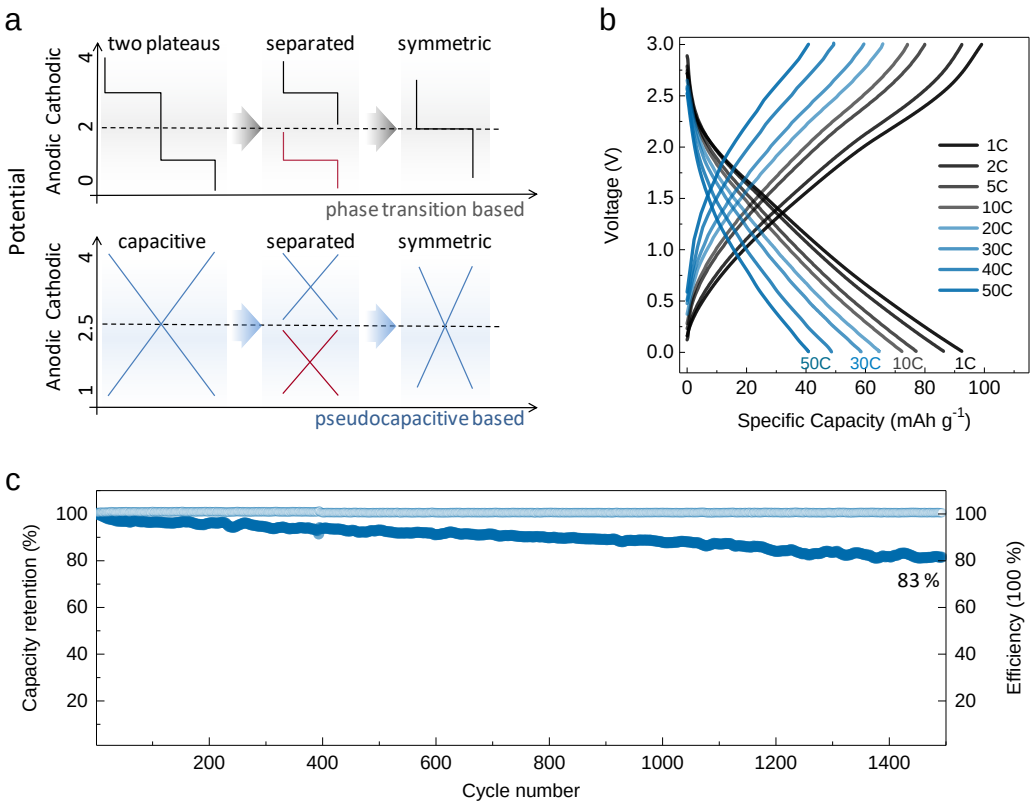

Figure A.4. Symmetric battery based on a-VO_2 with pseudocapacitive behavior. **a)** Schematics of two types of symmetric batteries based on bipolar electrode materials. For the top row, traditional phase transition based symmetric device configuration. The bipolar material with two obvious plateaus in the half-cell. The electrode can be assembled and cycled at both cathodic voltage plateau and anodic voltage plateau. For the bottom row, pseudocapacitance-enabled symmetric devices configuration. Bipolar material shows with wide-window capacitive behavior. **b)** Galvanostatic charge/discharge profiles at different rates from 1−50C. **c)** High-rate long-term cycling stability of a-VO_2 based symmetric device at 50C. A rate of 1C corresponds to 100 mA g^{-1} in the symmetric cell, based on the mass of both the cathode and anode materials.

The a-VO_2 symmetric battery was assembled with two identical electrodes, which was cut from the pre-sodiated a-VO_2 (discharge to 2.5 V) to a composition of $Na_{0.62}VO_2$. As shown in Fig. A.4.b and Supplementary Fig. A.20., the device operates in the 0 to 3 volt window with a linear voltage profile for galvanostatic charge and discharge and at 1C exhibits a reversible capacity of ~93 mAh g^{-1} based on the mass of both electrodes. This capacity is in good agreement with the values of the individual electrodes in half-cell experiments (Fig. A.3.e,f). The device can be operated at substantially higher rates, leading to values of 72 mAh g^{-1} at 10C and ~60 mAh g^{-1} at 30C. The ability to provide good energy density at such high rates can be attributed to the pseudocapacitive nature of the a-VO_2. At 30C, the full cell delivers an energy density of 63 Wh kg^{-1} at a power density of 3.3 kW kg^{-1}. The symmetric VO_2 battery also cycles quite well. At 50C, the specific capacity retained 83% of its initial value over 1500 cycles (Fig. A.4.c). We believe that the capacity loss arises from an increase in electronic resistance which occurs upon the addition of sodium ions in VO_2 (*ref.* [17]).

We also carried out additional safety experiments on overcharging/overdischarging, polarity swap, and self-discharge to further understand the characteristics of the symmetric battery. Preliminary results on overdischarging to −0.3 V and overcharging to 3.3V are described in Supplementary Fig. A.21. Afterwards, we reversed the polarity on a discharged cell at 0V and continued the cycling test. Interestingly, the capacity is retrieved after the polarity swap (see Supplementary Fig. A.22.) In the self-discharge experiments, both the individual electrodes as well as the full cell were investigated. As shown in Supplementary Fig. A.23., the open circuit potentials stabilize within a short period of time for the VO_2//Na cells at both cathodic and anodic windows as well as for the VO_2 symmetric cell. After the initial 10 hours, there is only a very gradual decrease in open circuit voltage. The discharge characteristics of the full cell after standing on open circuit for 100 hours indicate that the device retains 90% of its initial capacity.

A.3. Conclusions

Amorphous materials represent an interesting structure in which to examine charge storage properties. Rather than defined crystallographic pathways, these materials offer an open framework with the possibility of multiple percolation directions which facilitate ion transport and tolerate volumetric changes more uniformly than crystalline materials. The present paper shows that the Na^+ insertion properties of amorphous VO_2 are superior to those of its crystalline counterpart. In galvanostatic experiments, the material exhibits a linear voltage profile over a 3-volt range (4.0 to 1.0 V vs. Na/Na^+) leading to a reversible capacity of 400 mAh g^{-1}. The linear voltage characteristic enables the material to be prepared as both a positive electrode and a negative electrode for Na^+ batteries. Voltammetry studies indicate that the material exhibits pseudocapacitive behavior which lead to stable energy densities in the range of 120–125 mAh g^{-1} at 20C for each electrode. By using a-VO_2 as both the anode and cathode, we fabricated a symmetric Na^+ battery whose energy and power densities exceed the characteristics of other 'quasi-symmetric' batteries which involve phase transitions to retain their bipolar behavior.

A.4. Materials and Methods

Materials

Oxalic acid $H_2C_2O_4$ (≥99.0%), vanadium(V) oxide V_2O_5 (≥99.6%), hydrogen peroxide H_2O_2 (35 wt. %), sodium Na (≥98%), Sodium hexafluorophosphate $NaPF_6$ (≥98%), ethylene carbonate $C_3H_4O_3$ (≥99%), diethyl carbonate $(C_2H_5O)_2CO$ (≥99%), fluoroethylene carbonate $C_3H_3FO_3$ (≥99%), and Whatman glass fiber were purchased from Sigma−Aldrich. All reagents were used without further purification.

Synthesis

3D array of a-VO_2 electrode was prepared by a facile solvothermal method. In general, 2.5 mmol of $H_2C_2O_4$ and 0.75 mmol of V_2O_5 were dissolved in 5 mL of distilled water at 80^oC until the solution turns dark blue color. Then, 0.7 mL of H_2O_2 was added dropwise into the previous dark blue solution to form solution *I*. 35 mL ethanol was mixed with solution I in room temperature to form solution *II*. One piece of substrate (i.e., graphite foam[15] (GF)) was then immersed into the solution *II* in a 50 mL Teflon-lined stainless steel autoclave. The autoclave liner was kept at 180 ^oC for 2 h. The resulting a-VO_2 sample was collected by rinsing with distilled water and ethanol in turn for 3 times and dried in vacuum for 24 h. The c-VO_2 were synthesized with similar method by just increasing the concentration of solution *II* for ~3 times (with 7.5 mmol $H_2C_2O_4$, 2.25 mmol V_2O_5, and 2.1 mL of H_2O_2). The weight of VO_2 can be determined by weighting the GF before and after the solvothermal growth (analytical balance, RADWAG, MYA 21, d = 1 μg). We also checked that the weight of GF remains the same even if we further remove the VO_2 by acid. The areal mass of pure GF is 0.61 mg cm^{-2}. The VO_2 loading was 0.80 mg cm^{-2} for a-VO_2 and 1.00 mg cm^{-2} for c-VO_2 electrode. Herein, strategy of concentration control was employed to facilitate the assembly of preferred VO_2 nanostructures. As the decrease of the precursor concentration, the nucleation rate decreases, thus results in smaller nucleation particle sizes; Moreover, the presence of more electrolytes could promote instant 3D coagulation and aggregation for the growth of direction coordinated structures, thus facilitating the formation of thicker nano-wall c-VO_2 aggregates[25, 26, 27].

Materials characterization

The morphologies of the samples were characterized by field emission scanning electron microscopy (FESEM, JEOL JSM–6700F). The crystallographic structures of the

samples were identified using high-resolution transmission electron microscopy (HRTEM, JEOL 2100F at 200 kV) with an energy dispersive X-ray spectroscopy system. Valence states measurements were performed by X-ray photoelectron spectroscopy (XPS) with a VG ESCALAB 220i-XL system using a monochromatic AlK*a*1 source (1486.6 eV). The Ar^+ beam was rastered on the area of 2 × 3 mm for 60 s. The integrated area and atomic ratios of the peaks were fitted using the Casa-XPS software. The atomic sensitivity factors were from the Kratos library within the Casa software. The XRD patterns were recorded on Bruker-AXS D8 Advance X-ray diffractometer with CuKα radiation (λ = 1.54186 Å) at 40 KV and 40 mA on rotation between the angular range of 10^o to 60^o (2θ), using Ni detector slit and the Lynxeye detector, with a step size of 0.02^o and a time setting of 0.5 second per step. For the *ex situ* XPS and XRD experiments, the a-VO_2 and c-VO_2 working electrodes were sodiated and desodiated to their specific potentials. The cycled working electrodes were removed from the cell, washed with dimethyl carbonate and dried overnight in the argon-filled glovebox. These electrodes were loaded on the XPS/XRD sample holders in the glovebox and sealed in the transfer chambers to prevent exposure to the environment.

Electrochemical measurements

Swagelok cells were assembled in an argon-filled glove box (moisture and oxygen levels < 1 ppm) with the as-fabricated freestanding samples as the working electrode (without using binder or additives), the metallic sodium foil as both the counter and reference electrodes, 1 M $NaPF_6$ in ethylene carbonate − diethyl carbonate − fluoroethylene carbonate (1:1:0.03 in volume) as the electrolyte, and glass fiber as the separator. The galvanostatic charge/discharge, cyclic voltammetry (CV), cycling and electrochemical impedance spectroscopy measurements were carried out using LAND battery cycler (CT2001A) and Bio-

logic potentiostat (VMP3). The symmetric cell was fabricated with just the same mass loading of cathode and anode. Prior to full-cell assembling, one cycle activation of VO_2 in half-cell was performed with cut-off voltage at 2.5 V. CV and galvanostatic cycling were performed using cutoff voltages of 4.0 and 1.0 V vs. Na^+/Na for wide-potential window test, 4.0 and 2.5 V vs. Na^+/Na for cathodic-potential window test, 2.5 and 1.0 V vs. Na^+/Na for anodic-potential window test, and 3.0 and 0 V for symmetric cell test. The sweep rates for the CVs were between 0.2 and 50 mV s^{-1}. The current densities used for galvanostatic cycling ranged from 40 to 12000 mA g^{-1}. The capacities were calculated based on the mass of VO_2 active materials. Full cells were assembled in a soft-packed pouch geometry using the same cathode and anode. The self-discharge measurements were conducted by first charging at a current of 100 mA g^{-1} and then relaxing for 6000 min duration. The open-circuit potentials were recorded during the relax times. The energy and power densities were normalized to the total mass from both anode and cathode materials.

A.5. Supplementary Information

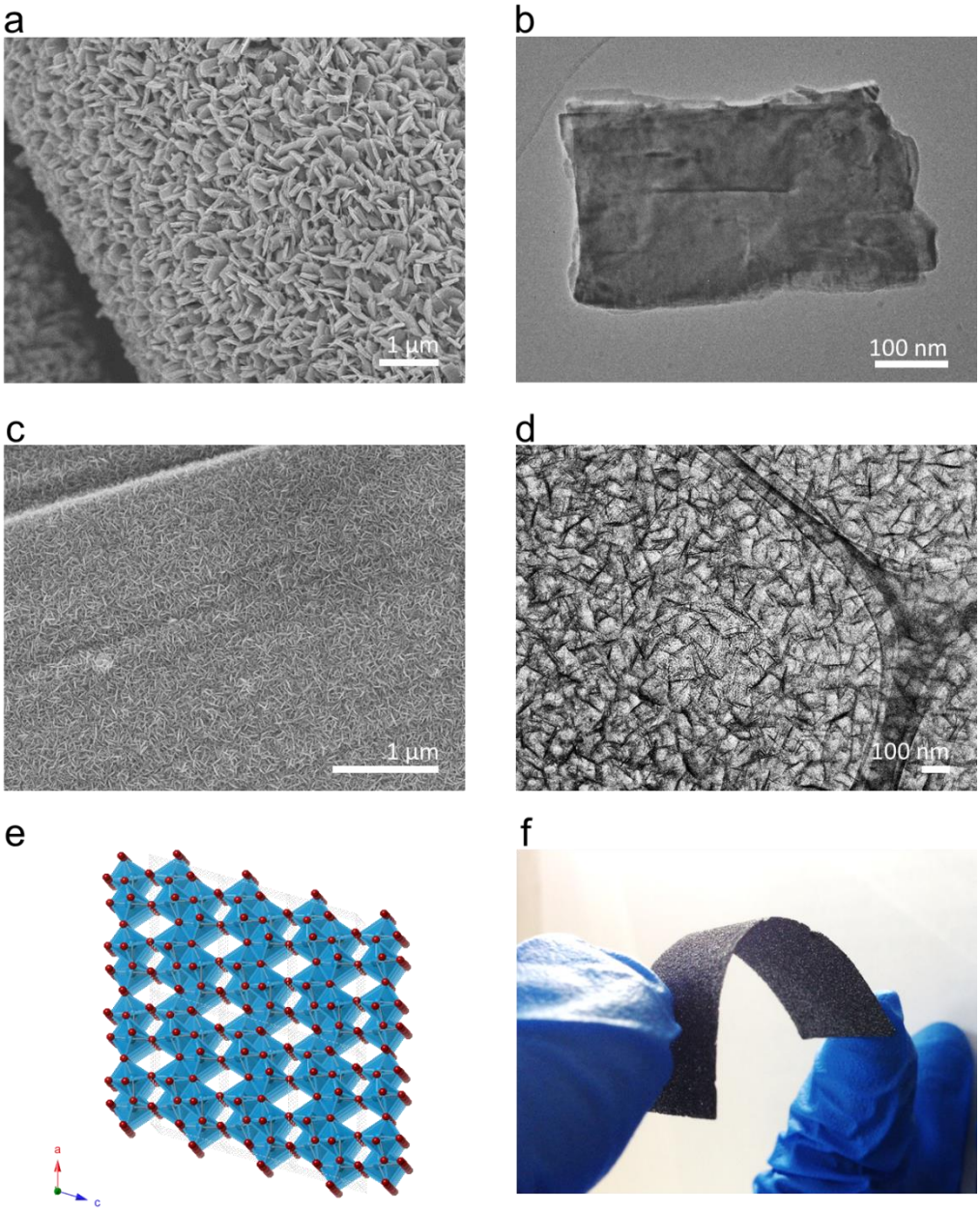

Figure A.5. Morphology and structural characterizations of c-VO_2 and a-VO_2. **a,b)** FESEM and TEM of GF supported c-VO_2 electrodes. **c,d)** FESEM and TEM of GF supported a-VO_2 electrodes. **e)** Crystal structure of monoclinic VO_2 (B) with two different types of square

pyramidal sites at the intervals of the VO_6 octahedra. **f)** Photograph showing the electrode is bent by a small force to demonstrate the flexibility and lightweight.

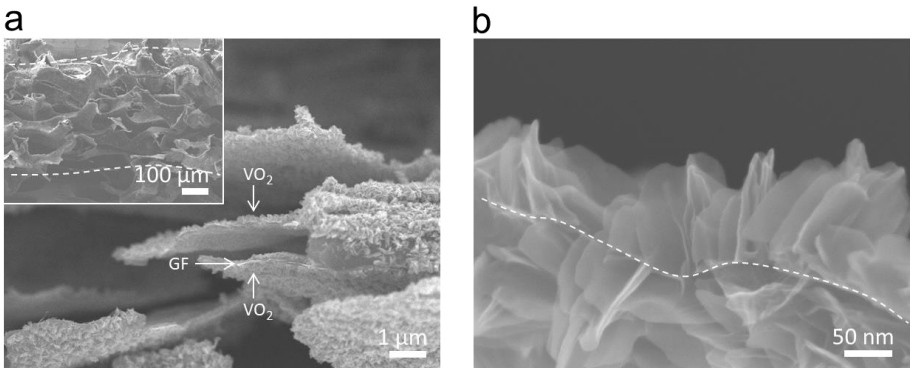

Figure A.6. Cross-section view of GF supported a-VO_2 electrodes at different magnification. The figures show a height of ~100 nm of the a-VO_2 nanosheet and the nanosheets anchor on both the outside and inner wall of the graphene foam.

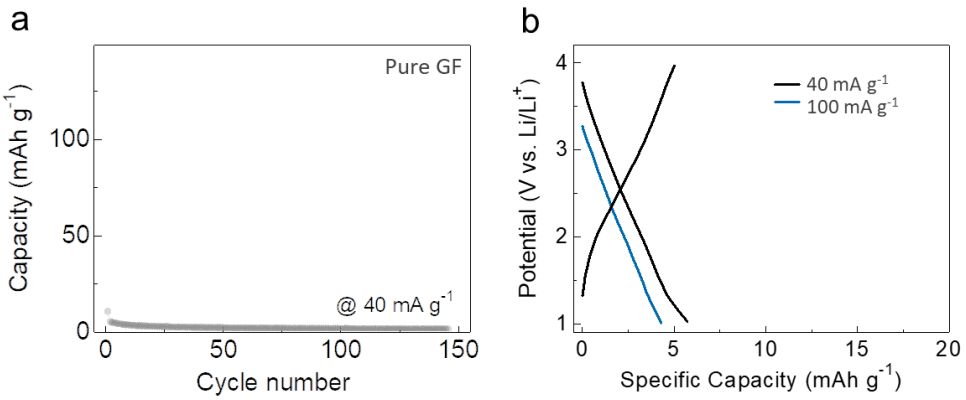

Figure A.7. Galvanostatic charge/discharge performance of pure GF in the voltage window of 4.0 and 1.0 V vs Na/Na^+. The result shows that the capacity contribution from GF in the composites are neglectable.

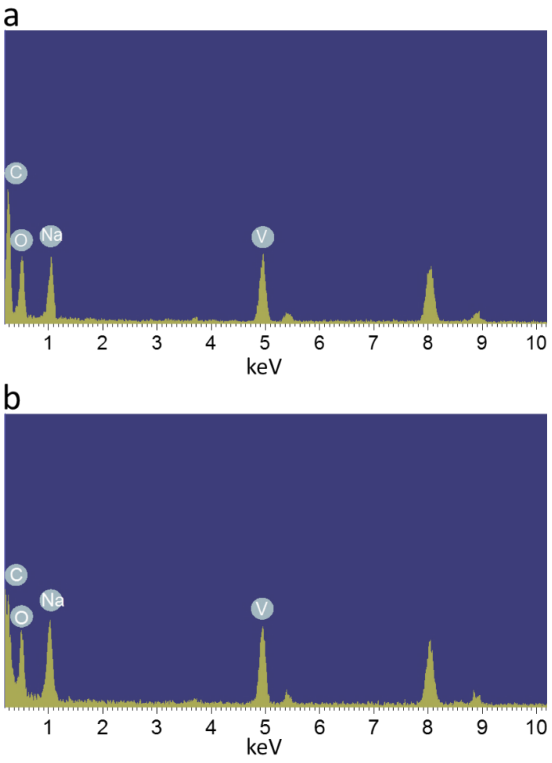

Figure A.8. EDX spectra of c-VO_2 **(a)** and a-VO_2 **(b)** after discharge. The results give Na:V ratio of nearly 1.10:1 for c-VO_2 and 1.22:1 for a-VO_2 electrodes.

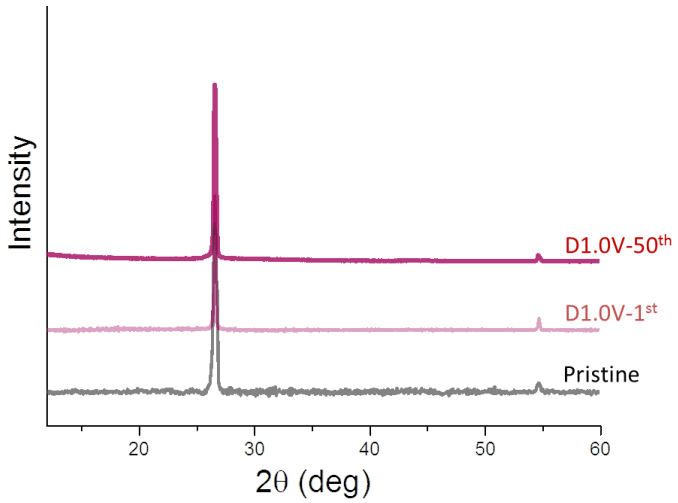

Figure A.9. *Ex situ* XRD patterns of a-VO_2 before and after charge/discharge cycles at 0.1C. The absence of any new peaks confirms the a-VO_2 retains its amorphous state after discharge in following cycles.

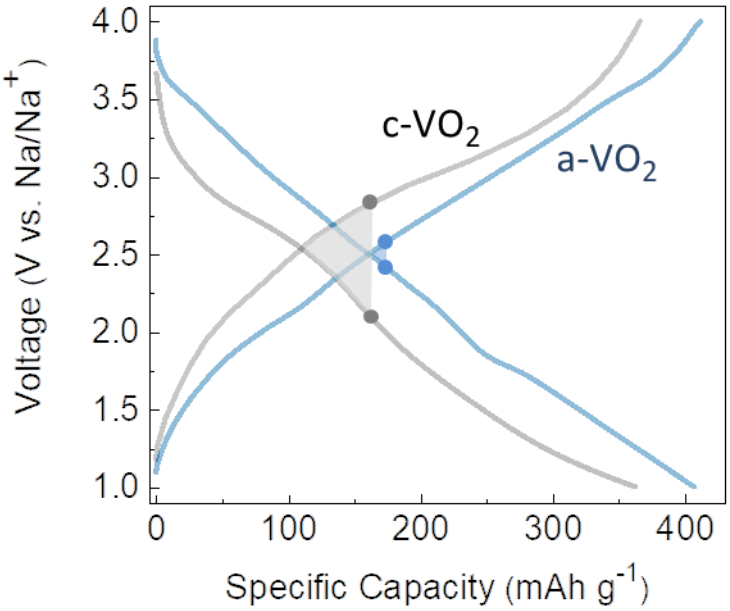

Figure A.10. Galvanostatic charge/discharge profile of c-VO_2 compared with a-VO_2 electrodes after 3 cycles activation at 0.1C. The *a*-VO_2 electrode delivers a specific discharge capacity of ~400 mAh g^{-1} at a slow rate of 0.1C (40 mA g^{-1}), whereas the c-VO_2 electrode shows a lower capacity of ~360 mAh g^{-1}. Notably, a-VO_2 leads to lower polarization (90 mV for the *a*-VO_2) and a sloped galvanostatic profile, suggesting the capability of fast charge storage through pseudocapacitance. In contrast, the galvanostatic profile for c-VO_2 shows a higher overpotential of 680 mV during the charge and discharge process.

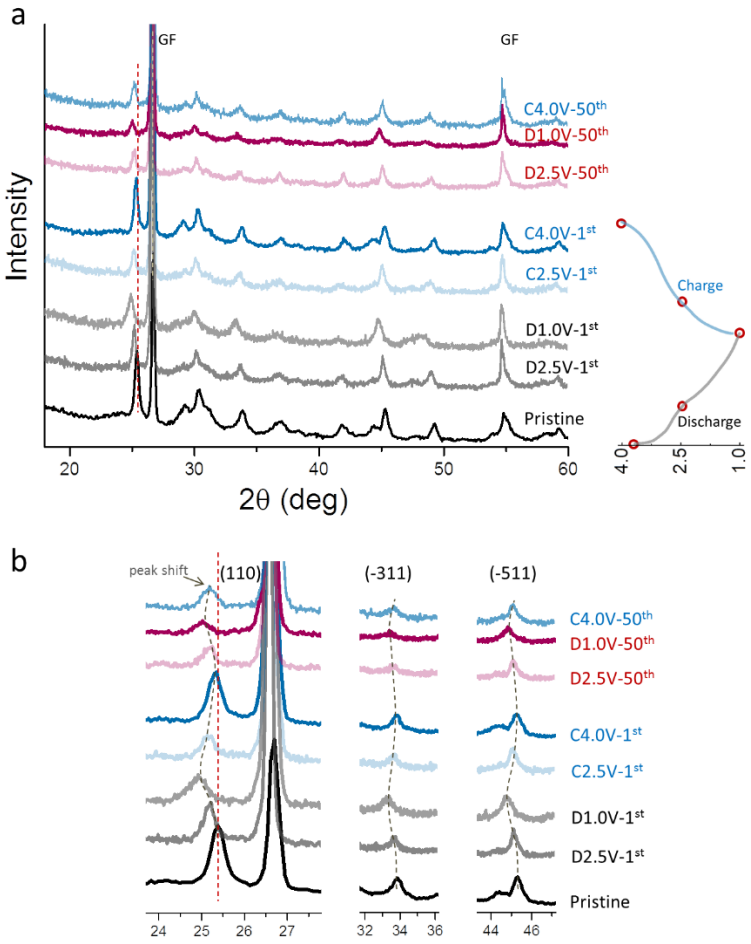

Figure A.11. Structural evolutions of c-VO_2 during cycles. *Ex situ* XRD patterns of c-VO_2 collected over 50 cycles at different discharge–charge voltages. The current density is 0.1C. No phase change occurs but the peaks do shift as Na^+ insertion and de-insertion affect the lattice parameter.

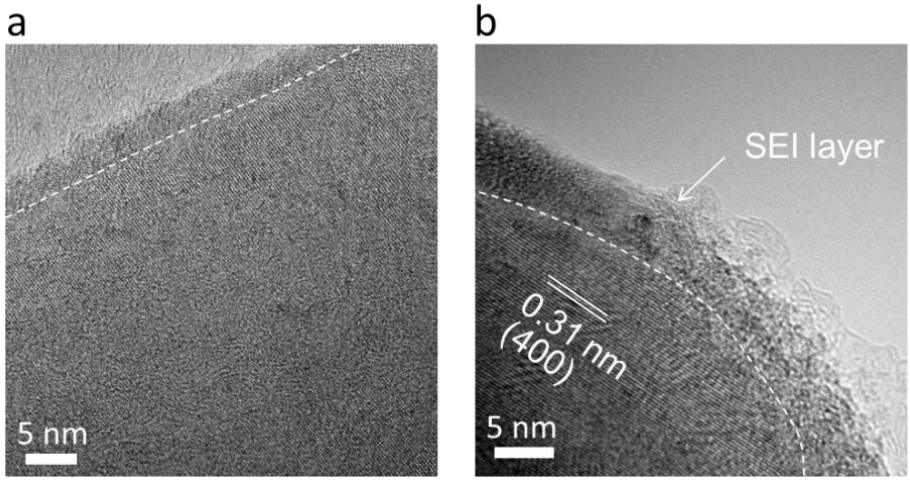

Figure A.12. *Ex situ* HRTEM images of the c-VO_2 collected after discharge at 0.1C. Single crystalline feature reserved after cycle with slight lattice expansion.

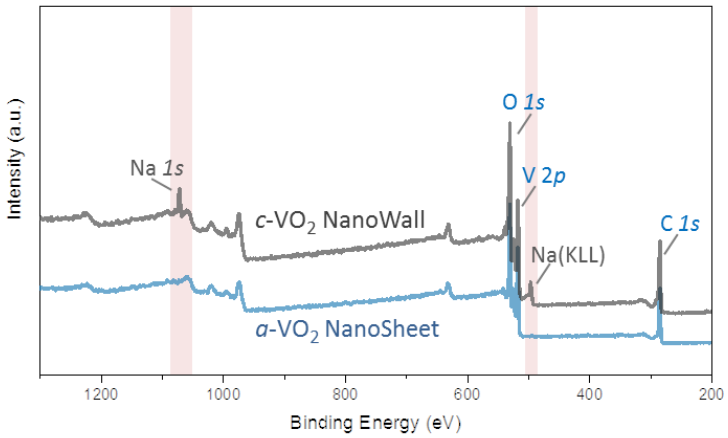

Figure A.13. XPS survey scan for c-VO_2 and a-VO_2 at the desodiated state D4.0V-50th after argon plasma etching to remove the outer surface layer. Note the absence of Na peak in the a-VO_2.

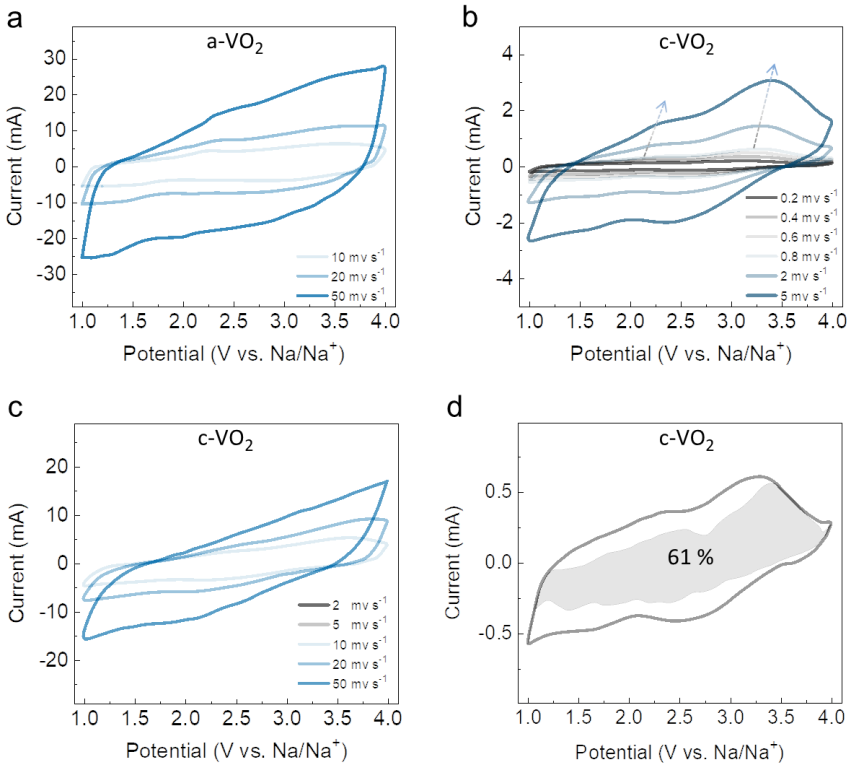

Figure A.14. a) CV curves at various scan rates (10 to 50 mV s^{-1}) for a-VO_2. **b,c)** for c-VO_2 electrodes. **d)** Capacitive (shaded area) and diffusion-controlled (cavity area) contribution to charge storage of c-VO_2 at 0.8 mV s^{-1}.

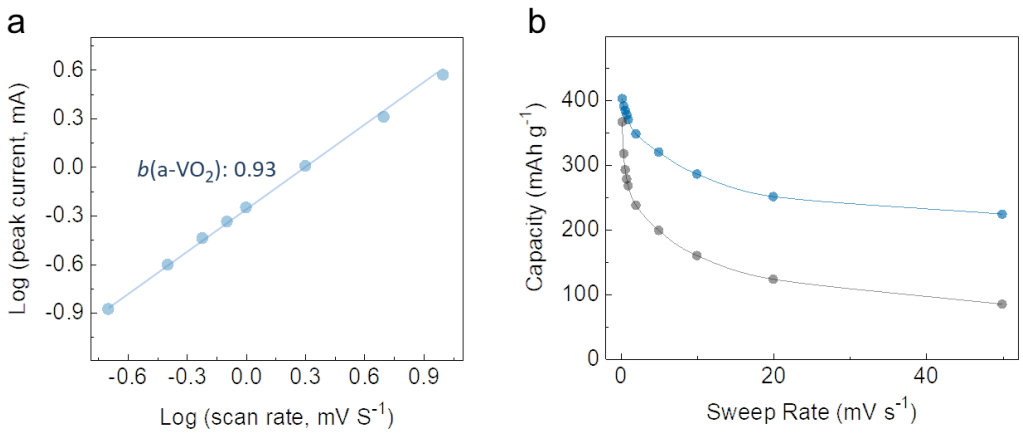

Figure A.15. a) Relationship between logarithm anodic peak current (at ca. 2.0 V) and logarithm scan rate for a-VO_2 from 0.2 to 10 mV s^{-1}. **b)** The mass-normalized capacity as function of sweep rate for a-VO_2 and c-VO_2.

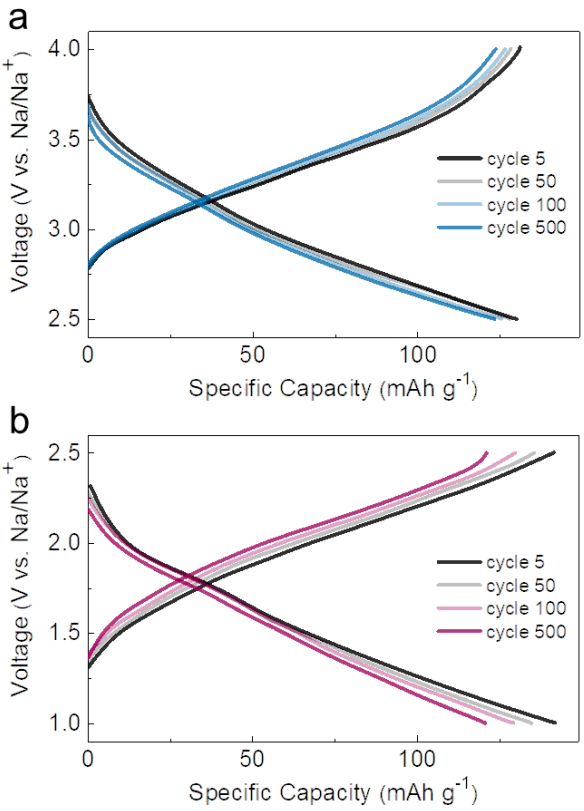

Figure A.16. Galvanostatic charge/discharge profiles of a-VO_2 electrode. Galvanostatic response at 20C for a-VO_2 for 500 cycles in **a)** the cathodic window and **b)** the anodic window.

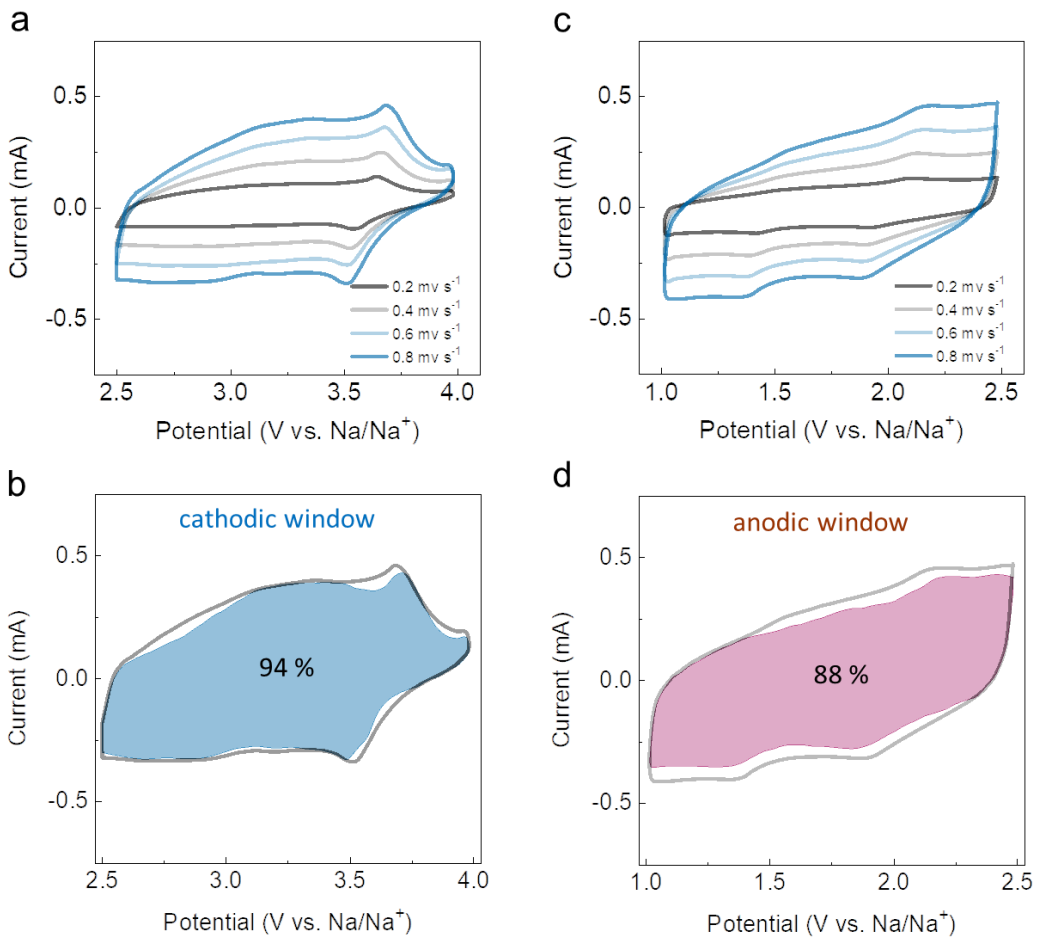

Figure A.17. CV curves at various scan rate for a-VO_2 electrode at specific cathode/anode window. **a,c)** in cathodic and anodic windows, respectively. **b,d)** Capacitive (shaded area) and diffusion-controlled (cavity area) contribution to charge storage of a-VO_2 electrode in cathodic and anodic windows, respectively.

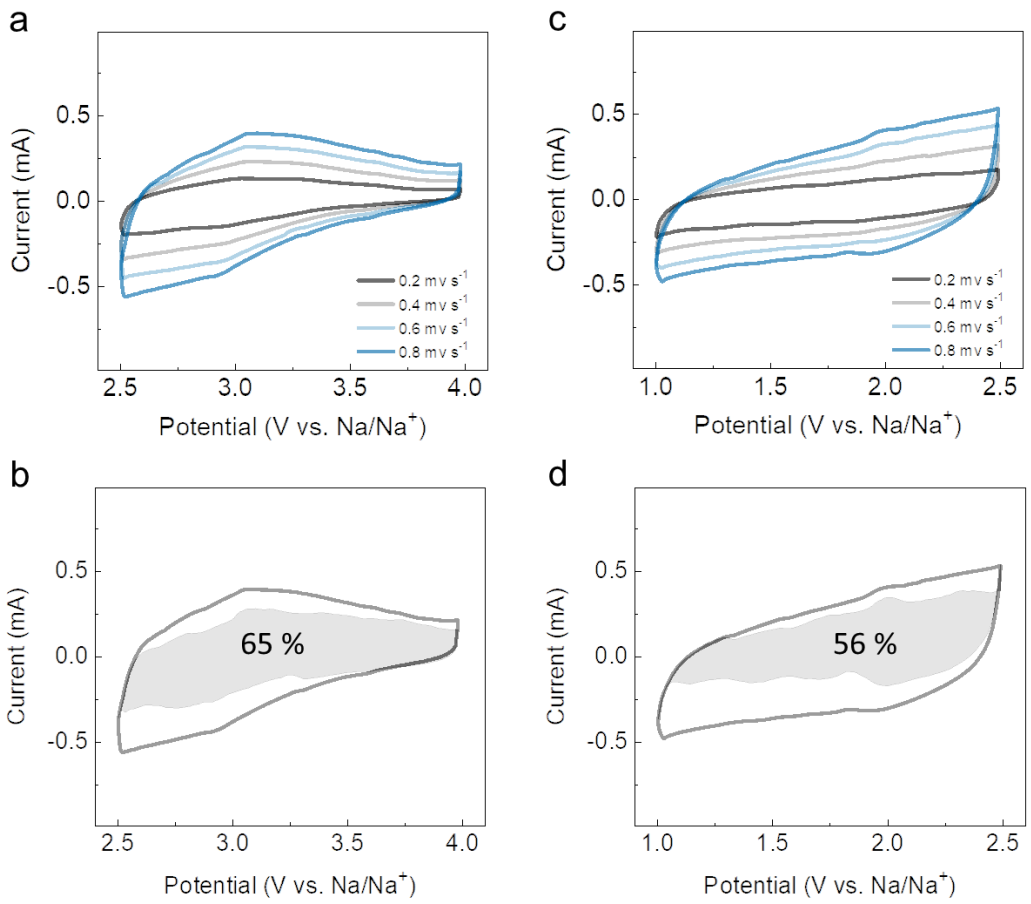

Figure A.18. CV curves at various scan rate for c-VO_2 electrode at specific cathode/anode window. **a,c)** in cathodic and anodic windows, respectively. **b,d)** Capacitive (shaded area) and diffusion-controlled (cavity area) contribution to charge storage of c-VO_2 electrode in cathodic and anodic windows, respectively.

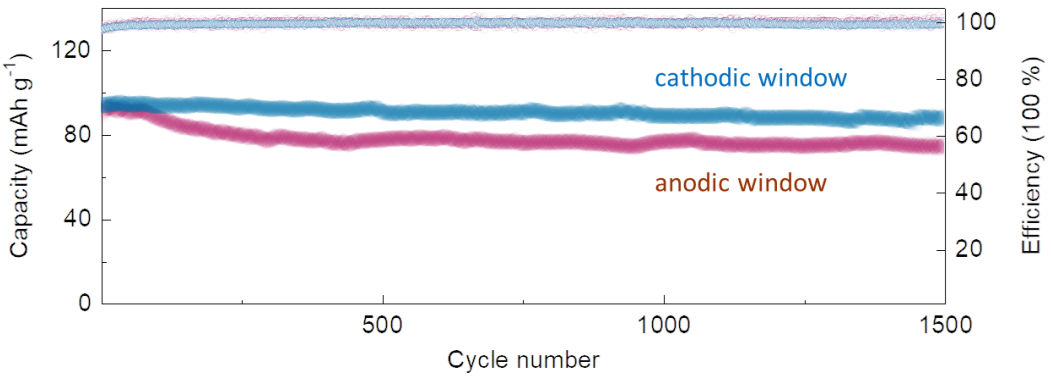

Figure A.19. High-rate long-term cycling stability of a-VO_2 electrode at 60C in both cathodic and anodic windows. A rate of 1C corresponds to 200 mA g^{-1}.

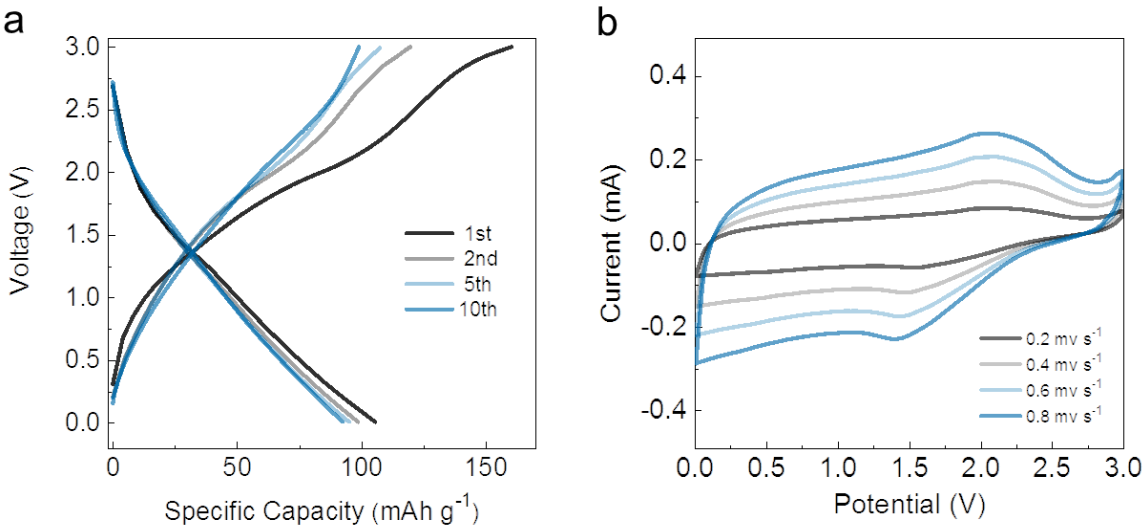

Figure A.20. The electrochemical performance of bipolar a-VO_2 based symmetric device. **a)** First ten cycles activation of a-VO_2 based symmetric device at 1C. **b)** CV curves at various scan rate of 0.2, 0.4, 0.6, 0.8 mV s^{-1} of a-VO_2 symmetric device after activation.

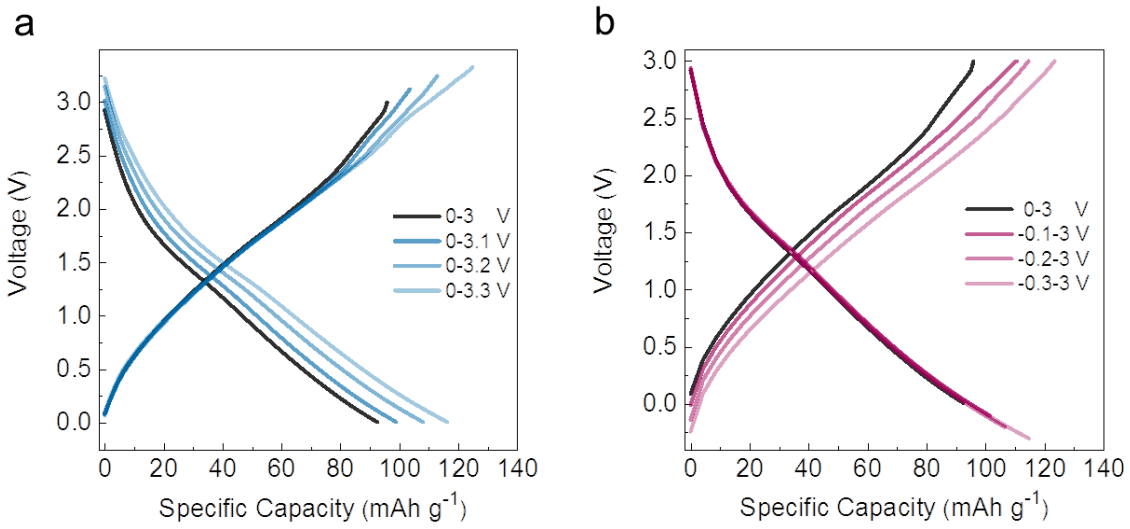

Figure A.21. Overcharging and overdischarging characteristics of the a-VO_2 symmetric cell at 1C. **a)** Over charge performance in the voltage range of 0 to 3.3 V. **b)** Over discharge performance in the voltage range of −0.3 to 3.0 V.

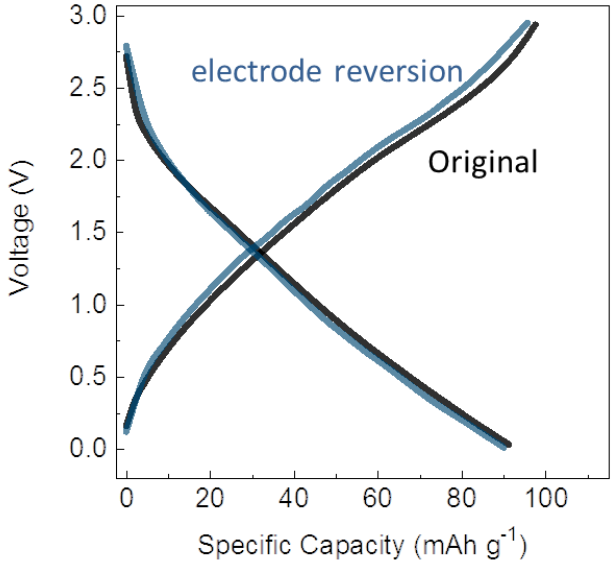

Figure A.22. The polarity swap test of the a-VO_2 symmetric cell. Comparison of discharge profiles at 1C before and after electrode reversion.

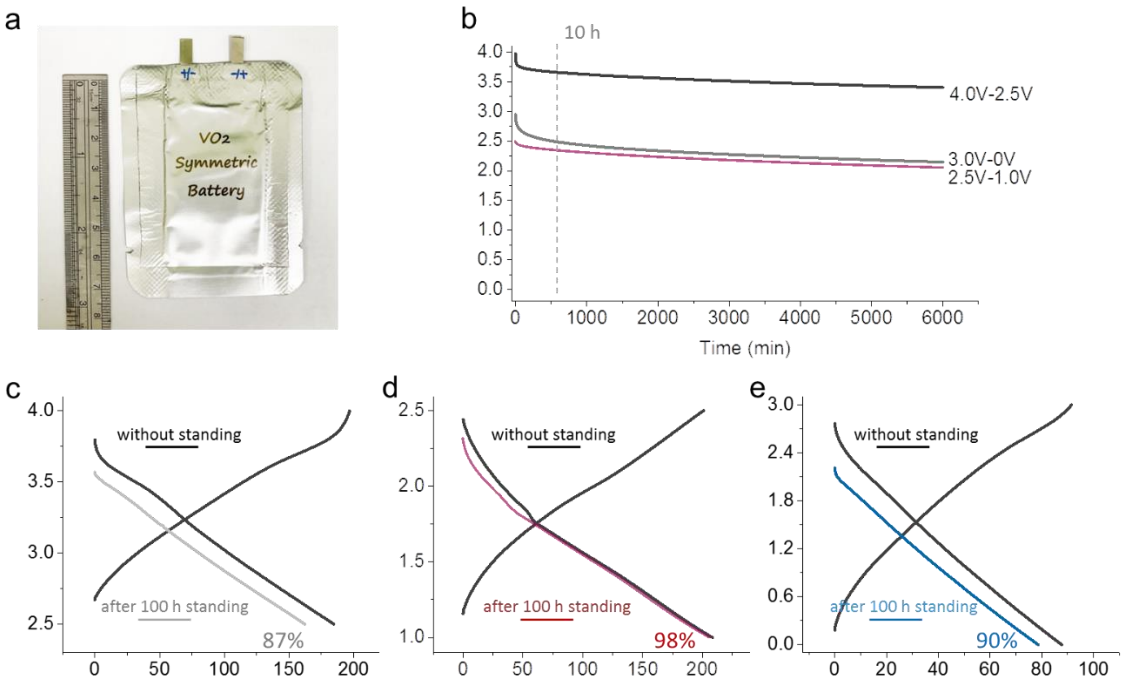

Figure A.23. Self-discharge properties of the individual electrode and the entire device. **a)** Photograph of a soft-packed pouch cell demonstration of a-VO_2 symmetric cell. **b)** The stability of open-circuit potential as a function time. **c-e)** The discharge behavior of the VO_2//Na cell at cathodic window **(c)**, anodic window **(d)**, and VO_2 symmetric cell **(e)** after 100 hours of open circuit, the cell retains nearly 90% of its initial capacity at 2C.

A.6. References

1. Jung S-K, Kim H, Cho MG, Cho S-P, Lee B, Kim H*, et al.* Lithium-free transition metal monoxides for positive electrodes in lithium-ion batteries. *Nature Energy* 2017, 2(2): 16208.

2. Simon P, Gogotsi Y, Dunn B. Where Do Batteries End and Supercapacitors Begin? *Science* 2014, 343(6176): 1210-1211.

3. Brezesinski T, Wang J, Tolbert SH, Dunn B. Ordered mesoporous alpha-MoO3 with iso-oriented nanocrystalline walls for thin-film pseudocapacitors. *Nat Mater* 2010, 9(2): 146-151.

4. Sun H, Mei L, Liang J, Zhao Z, Lee C, Fei H*, et al.* Three-dimensional holey-graphene/niobia composite architectures for ultrahigh-rate energy storage. *Science* 2017, 356(6338): 599-604.

5. Augustyn V, Come J, Lowe MA, Kim JW, Taberna PL, Tolbert SH*, et al.* High-Rate Electrochemical Energy Storage Through Li+ Intercalation Pseudocapacitance. *Nat Mater* 2013, 12(6): 518-522.

6. Acerce M, Voiry D, Chhowalla M. Metallic 1T phase MoS2 nanosheets as supercapacitor electrode materials. *Nat Nanotechnol* 2015, 10(4): 313-318.

7. Lai C-H, Ashby DS, Lin TC, Lau J, Dawson A, Tolbert SH*, et al.* Application of Poly(3-hexylthiophene-2,5-diyl) as a Protective Coating for High Rate Cathode Materials. *Chem Mater* 2018, 30(8): 2589-2599.

8. Wei MD, Sugihara H, Honma I, Ichihara M, Zhou HS. A New Metastable Phase of Crystallized V2O4·0.25H2O Nanowires: Synthesis and Electrochemical Measurements. *Adv Mater* 2005, 17(24): 2964-2969.

9. Lee S, Sun XG, Lubimtsev AA, Gao X, Ganesh P, Ward TZ*, et al.* Persistent Electrochemical Performance in Epitaxial VO2(B). *Nano Lett* 2017.

10. Wu C, Xie Y. Promising vanadium oxide and hydroxide nanostructures: from energy storage to energy saving. *Energy Environ Sci* 2010, 3(9): 1191-1206.

11. Chao D, Zhu C, Xia X, Liu J, Zhang X, Wang J*, et al.* Graphene Quantum Dots Coated VO2 Arrays for Highly Durable Electrodes for Li and Na Ion Batteries. *Nano Lett* 2015, 15(1): 565-573.

12. Mai L, Wei Q, An Q, Tian X, Zhao Y, Xu X*, et al.* Nanoscroll Buffered Hybrid Nanostructural VO (B) Cathodes for High-Rate and Long-Life Lithium Storage. *Adv Mater* 2013, 25(21): 2969-2973.

13. Yang S, Gong Y, Liu Z, Zhan L, Hashim DP, Ma L*, et al.* Bottom-up approach toward single-crystalline VO2-graphene ribbons as cathodes for ultrafast lithium storage. *Nano Lett* 2013, 13(4): 1596-1601.

14. He G, Li L, Manthiram A. VO2/rGO nanorods as a potential anode for sodium- and lithium-ion batteries. *J Mater Chem A* 2015, 3(28): 14750-14758.

15. Chao D, Lai C-HM, Liang P, Wei Q, Wang Y-S, Zhu CR*, et al.* Sodium Vanadium Fluorophosphates (NVOPF) Array Cathode Designed for High-Rate Full Sodium Ion Storage Device. *Adv Energy Mater* 2018, 8(16): 10.1002/aenm.201800058.

16. Mahadi NB, Park J-S, Park J-H, Chung KY, Yi SY, Sun Y-K*, et al.* Vanadium dioxide – Reduced graphene oxide composite as cathode materials for rechargeable Li and Na batteries. *J Power Sources* 2016, 326: 522-532.

17. Wang W, Jiang B, Hu L, Lin Z, Hou J, Jiao S. Single crystalline VO2 nanosheets: A cathode material for sodium-ion batteries with high rate cycling performance. *J Power Sources* 2014, 250: 181-187.

18. Liu J, Li Q, Wang T, Yu D, Li Y. Metastable vanadium dioxide nanobelts: hydrothermal synthesis, electrical transport, and magnetic properties. *Angewandte Chemie* 2004, 43(38): 5048-5052.

19. Brousse T, Belanger D, Long JW. To Be or Not To Be Pseudocapacitive? *J Electrochem Soc* 2015, 162(5): A5185-A5189.

20. Wang D, Bie X, Fu Q, Dixon D, Bramnik N, Hu YS*, et al.* Sodium vanadium titanium phosphate electrode for symmetric sodium-ion batteries with high power and long lifespan. *Nature communications* 2017, 8: 15888.

21. Zhu C, Kopold P, van Aken PA, Maier J, Yu Y. High Power-High Energy Sodium Battery Based on Threefold Interpenetrating Network. *Adv Mater* 2016, 28(12): 2409-2416.

22. Senguttuvan P, Rousse G, Arroyo y de Dompablo ME, Vezin H, Tarascon JM, Palacin MR. Low-potential sodium insertion in a NASICON-type structure through the Ti(III)/Ti(II) redox couple. *J Am Chem Soc* 2013, 135(10): 3897-3903.

23. Wang Y, Xiao R, Hu YS, Avdeev M, Chen L. P2-Na0.6[Cr0.6Ti0.4]O2 cation-disordered electrode for high-rate symmetric rechargeable sodium-ion batteries. *Nature communications* 2015, 6: 6954.

24. Wang Y-Z, Shan X-Y, Wang D-W, Sun Z-H, Cheng H-M, Li F. A Rechargeable Quasi-symmetrical MoS 2 Battery. *Joule* 2018, 2(7): 1278-1286.

25. Gursky JA, Blough SD, Luna C, Gomez C, Luevano AN, Gardner EA. Particle−Particle Interactions Between Layered Double Hydroxide Nanoparticles. *J Am Chem Soc* 2006, 128(26): 8376-8377.

26. Ma JM, Lei DN, Duan XC, Li QH, Wang TH, Cao AM*, et al.* Designable Fabrication of Flower-Like SnS2 Aggregates with Excellent Performance in Lithium-Ion Batteries. *RSC Advances* 2012, 2(9): 3615-3617.

27. Xu ZP, Stevenson G, Lu C-Q, Lu GQ. Dispersion and Size Control of Layered Double Hydroxide Nanoparticles in Aqueous Solutions. *J Phys Chem B* 2006, 110(34): 16923-16929.

Appendix B: Carbon nanofoam paper enables high-rate and high-capacity Na-ion storage

**a version of this dissertation appendix was published in Energy Storage Materials (DOI:10.1016/j.ensm.2019.05.040) in collaboration with Jesse S. Ko, Megan B. Sassin, Ashley N. Hoffmaster, Bruce S. Dunn, Debra R. Rolison, and Jeffrey W. Long*

Carbon nanofoams (CNF) fabricated within carbon-fiber paper are investigated as negative electrodes for electrochemical Na-ion storage. In electrolyte-limited half-cell testing vs. sodium metal, these freestanding, ultraporous electrode architectures deliver specific capacity >200 mA h g_{CNF}^{-1} at a 1C rate and >150 mA h g_{CNF}^{-1} at 10C. The outstanding charge-storage capacity is a consequence of the high defect concentration inherent to the amorphous carbon nanofoam, which maximizes a capacitively controlled sodiation mechanism, while the through-connected pore structure of the CNF facilitates high-rate capability. We also compare the electrochemical performance of two pore–solid architectural variants of CNF paper electrodes.

B.1. Introduction

Sodium-ion batteries (Na-ion; NIBs) have recently emerged as a compelling competitor to lithium-ion batteries[1,2] with the advantages of offering safer operation and using more abundant chemical elements (Na^+ as the charge-compensating cation and Fe- or Mn-based positive electrodes).[3] Despite the chemical similarities and closely related charge-storage mechanisms between sodium and lithium ions, the broader application and commercialization of NIBs has been limited by the lack of a low-cost, reliable negative electrode material that provides performance comparable to graphite in LIBs.[4] Graphite-intercalation compounds have positive energies of formation with sodium, such that electrochemical sodiation of pristine

graphite is problematic[5], thus prompting the search for alternative negative electrodes for Na^+ storage.

Stevens and Dahn first demonstrated that hard carbon (amorphous, non-graphitizable) exhibits reversible Na^+ capacity approaching 300 mA h g^{-1}, although with poor first-cycle coulombic efficiency.[6,7] The electrochemical charge-storage model for Na-ion involves a multi-stage association at carbon defects that dominates at high potentials, followed by intercalation into turbostratic (small, randomly oriented) domains, and ultimately filling micropores (< 2 nm) in the plateau region, ~ 0 V vs. Na/Na^+. This model is corroborated experimentally by *in-situ* Raman scattering[8] and electrochemical measurements of size-tuned turbostratic domains[9], and reinforced by computational studies on the binding energy of Na^+ at defective graphene sheets[10] and amorphous carbon.[11] Such findings have spurred research on a myriad of other types of carbon for Na-ion storage, including soft porous carbon[12,13], graphene[14,15], carbon nanofibers/wires[16,17], and carbon nanospheres.[18,19] Specifically, highly disordered carbon has shown promising sodium-ion storage at challenging current demand.[20,21,22]

The demonstrated benefits of defects and disorder in amorphous carbonaceous materials for Na-ion storage can be captured in a device-ready, binder-free electrode architecture comprising aerogel-like carbon nanofoam supported within the confines of carbon-fiber paper. This electrode design concept was previously developed[23] and validated for such applications as aqueous electrochemical capacitors[24,25], but also exhibits multiple structural characteristics that should be beneficial for Na-ion storage. The sol–gel-derived carbon nanofoam marries an inherently disordered nature and high micropore content to a 3D-wired network of mesopores and/or macropores. The final electrode architecture provides high specific surface area (300–600 m^2 g_{Total}^{-1}) and internal free volume to sustain ion balance during high-rate charge–discharge.[25] This physicochemical expression of electrified interface includes the features necessary for efficient Na-ion insertion and adsorption according to the multistage

model described above. As a freestanding electrode structure, CNF papers also mitigate the need for binder or conductive additives, the latter of which induce undesirable side reactions during Na-ion storage and contribute to low first-cycle Coulombic efficiency.[26]

B.2. Results and Discussion

In this study, we examine two CNF pore–solid structures in which the pore-size distribution is controlled by varying the precursor resorcinol–formaldehyde (RF) formulation: "40/500" and "50/500" CNF papers designate either 40 or 50 wt% RF, with both sol-to-gel reactions catalyzed using a resorcinol to catalyst (Na_2CO_3) molar ratio of 500.[23,25] The key differences, respectively, between the 40/500 and 50/500 CNF papers are specific surface area (~420 vs. ~550 $m^2 g_T^{-1}$), mean pore size (17 vs. 8 nm), and total pore volume (1.2 vs. 0.92 $cm^3 g_T^{-1}$).[25] Scanning electron microscopy (SEM) of 40/500 and 50/500 CNF paper (Figure B.1a,b, respectively) reveals the open porosity and aperiodic architecture of the CNF domains and visually validates why this pore–solid architectured foam promotes rapid mass transport and electrolyte infiltration. The hard-carbon character of these materials is verified by X-ray diffraction (XRD; Figure B.1c) and Raman scattering (Figure B.1d). As expected for sol–gel-derived carbon[27], the XRD peaks at ~25° and ~44° 2θ are broad while the ratio of integrated Raman intensity (I_D/I_G) of the D-band (defective graphite bonds) and G-band (pristine graphite) indicates highly disordered carbon.[28]

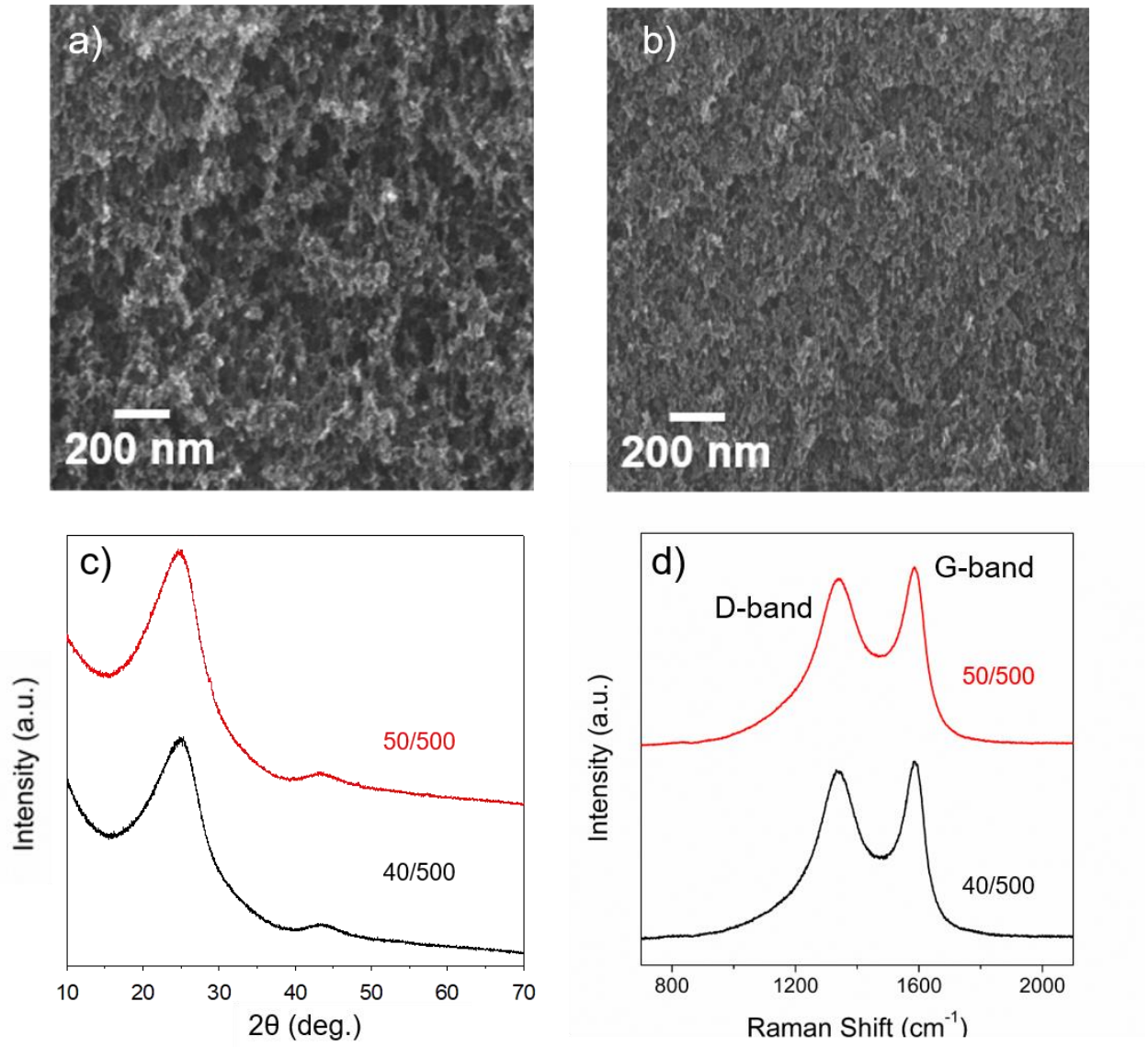

Figure B.1. Structural information on the CNF papers including cross-sectional SEM of the **a)** 40/500 and **b)** 50/500 architectures; **c)** X-ray diffraction; and **d)** Raman spectroscopy.

The CNF electrodes are electrochemically characterized in a two-terminal configuration with sodium metal acting as both counter and reference electrode. We use an electrolyte comprising 1 M $NaPF_6$ in diethylene glycol dimethyl ether (diglyme) to minimize solid electrolyte interphase (SEI) decomposition during cycling observed in conventional carbonate-based

electrolytes.[29-31] Cyclic voltammetry provides an initial assessment of charge-storage dynamics in the CNF electrodes. Representative voltammograms at sweep rates ranging from 0.5 to 5 mV s^{-1} for CNF-containing half-cells are shown in Figure B.2. At slow sweep rates, peak-like features in the 0–0.2 V region dominate, while at fast rates the voltammetric shapes become more capacitor-like, with contributions broadly expressed across a larger voltage range (0–1.4 V). Such trends are similar to those reported for related highly defective carbons in Na-ion electrolytes.[20,21,22]

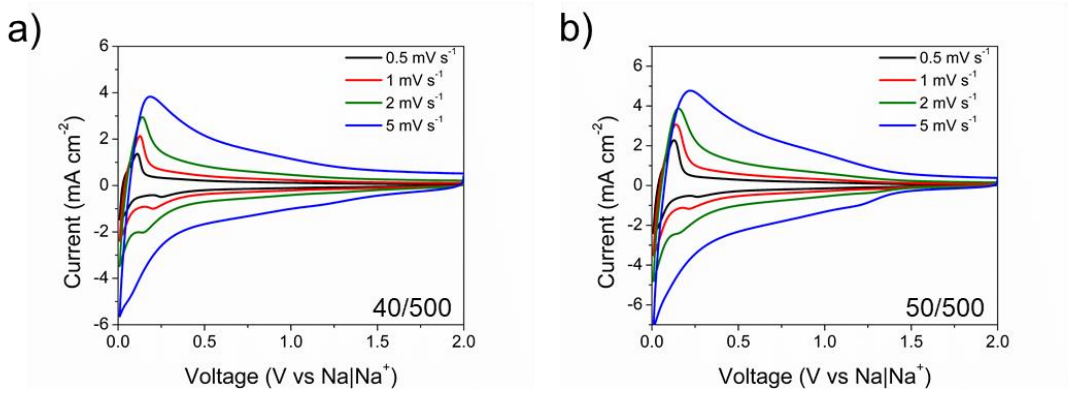

Figure B.2. Cyclic voltammograms at various sweep rates for cells containing **a)** 40/500 and **b)** 50/500 carbon nanofoams.

The first cycle of galvanostatic charge–discharge testing is shown in Figure B.3a for individual CNF||Na cells containing either 40/500 or 50/500 CNF paper. The shape of the discharge curve is typical for a hard carbon, with a sloping region from 2 V to ~0.1 V and finishing with a plateau region below ~0.1 V. The ~80 micron-thick CNF paper electrodes have respective CNF loadings of 2.82 and 3.65 mg_{CNF} cm^{-2} for 40/500 (4.38 mg_T cm^{-2}) and 50/500 (5.21 mg_T cm^{-2}), which are higher active material loadings than the 1–2 mg cm^{-2} typical for powder-composite electrodes of similar thickness.[32-34] Although the mass of both architectures

includes 30–40 wt% carbon fiber, nearly all of the capacity is derived from the amorphous CNF. Galvanostatic measurements on cells using carbon fiber paper (no CNF) provide a reversible capacity < 25 mA h g_T^{-1} (Figure B.4.).

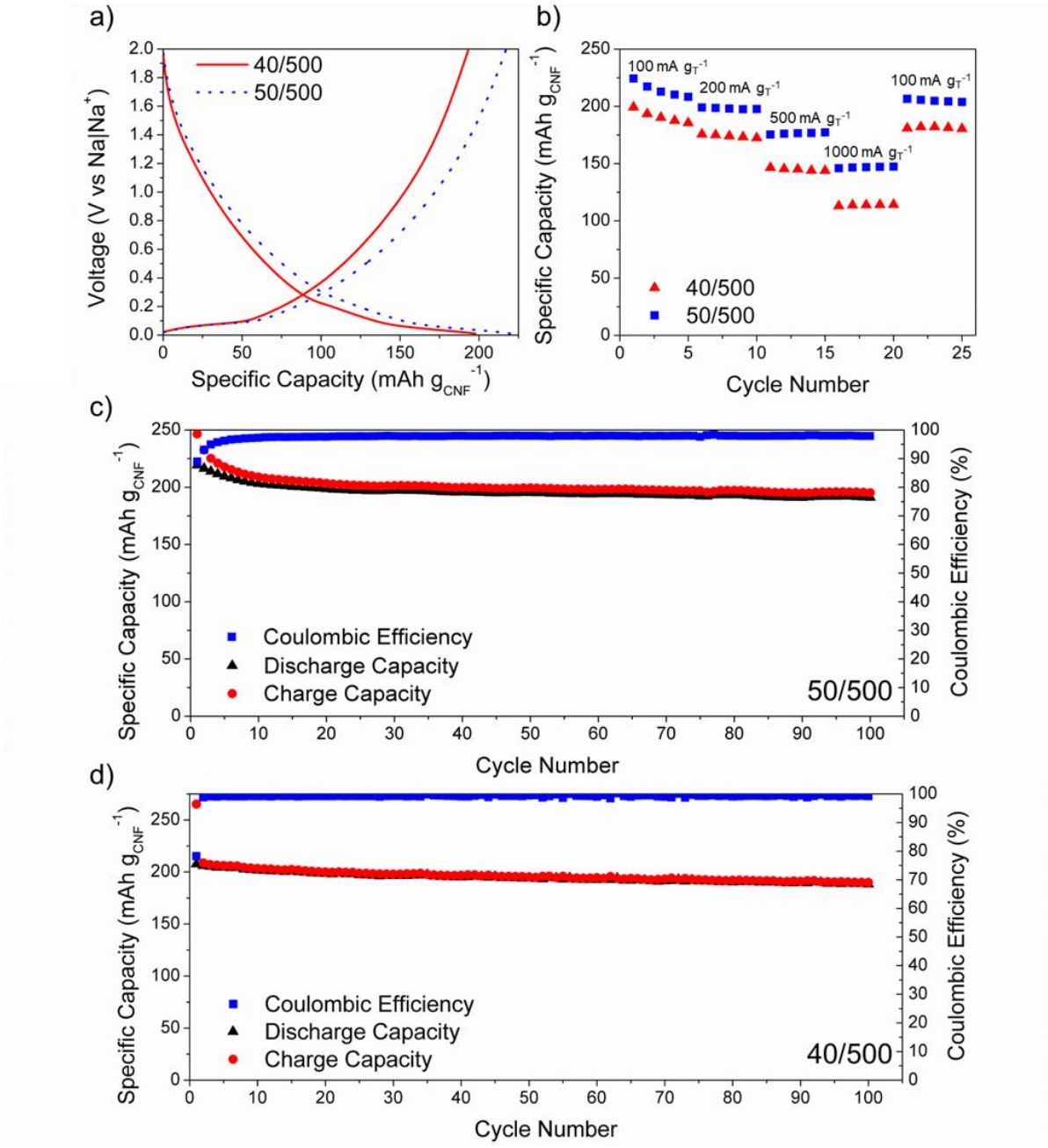

Figure B.3. a) Galvanostatic cycling at a current of 100 mA g_T^{-1}; **b)** galvanostatic rate retention; and long-term cycling of **c)** 50/500 CNF paper and **d)** 40/500 paper at a current density of 100 mA g_T^{-1}.

The initial Coulombic efficiency for cells containing either architecture is an encouraging >80% at 100 mA g_T^{-1} and quickly stabilizes to >98% on subsequent cycles. First-cycle efficiency (FCE) for half cells using hard carbon generally ranges between 60–80% in carbonate electrolytes and can be substantially lower for those high surface–area materials that facilitate formation of SEI in unstable electrolyte.[35,36] Recently, improved FCE has been demonstrated for similar electrode materials in glyme electrolyte.[31,37] Other factors such as choice of binder and conductive carbon may impact coulombic efficiency during half-cell cycling[38]; for example, the presence of “Super P” carbon in composite electrodes has been linked to severe first-cycle capacity losses.[26]

The 50/500 CNF sustains higher capacity than its 40/500 counterpart over all rates (Figure B.3b) and even delivers 150 mA h g_{CNF}^{-1} at 1 A g_T^{-1} or 5 mA cm^{-2} (complete charge or discharge over ~5 min). We attribute the performance difference to the ~30% higher specific surface area of the 50/500 architecture. Higher surface area amplifies the number of defects (thus increasing defect-mediated charge-storage in the sloping region) and subsequently enhances Na^+ capacity—as seen in Figure B.3a.

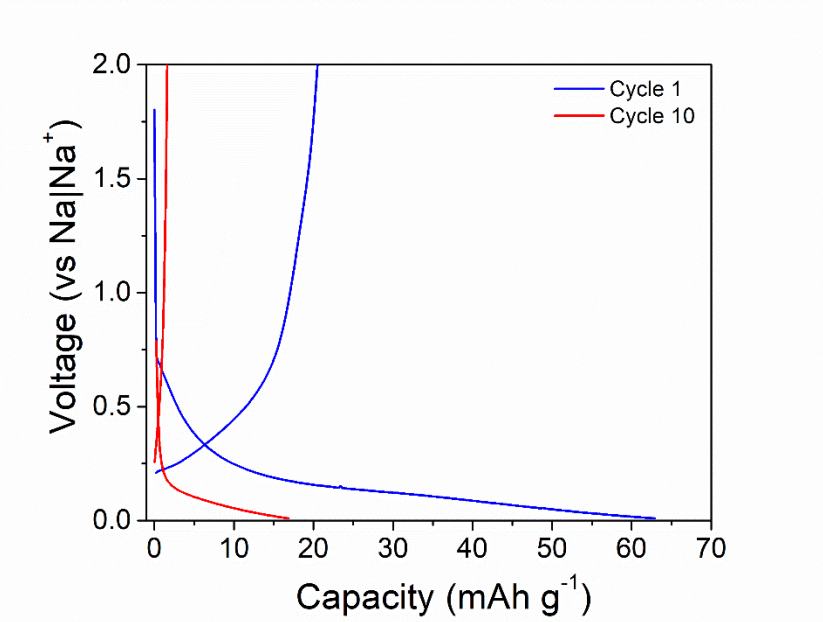

Figure B.4. Galvanostatic cycling (100 mA g^{-1}) of Na-ion half-cell containing Lydall carbon-paper as the cathode.

The capacity for 50/500 CNF paper at 100 mA g_T^{-1} or 0.5 mA cm^{-2} is 222±3 mA h g_{CNF}^{-1}, which is typical for most hard carbon systems (reversible capacity generally between 200–300 mA h g^{-1}).[35,39] When normalized to the entire weight of the CNF paper, the 50/500 architecture provides >140 mA h g_T^{-1} in one hour. For comparison, an industrial LIB graphite anode delivers specific capacity of 210 mA h g_T^{-1} at low rates (including the weight of binder and copper current collector).[40] Graphite LIB anodes are known to fade dramatically with increasing rates[41], whereas the 50/500 CNF paper still delivers >100 mA h g_T^{-1} at a rate of ~10C. This is also significantly higher than other phenol resin-derived, highly-porous carbons tested either as powder composites[42-44] or as monoliths.[45] Long-term cycling performance of the 50/500 and 40/500 electrodes, exercised at 100 mA g_T^{-1}, is shown in Figure B.3c,d respectively; specific capacity remains above 190 mA h g_{CNF}^{-1} after 100 cycles in the 50/500 CNF electrode.

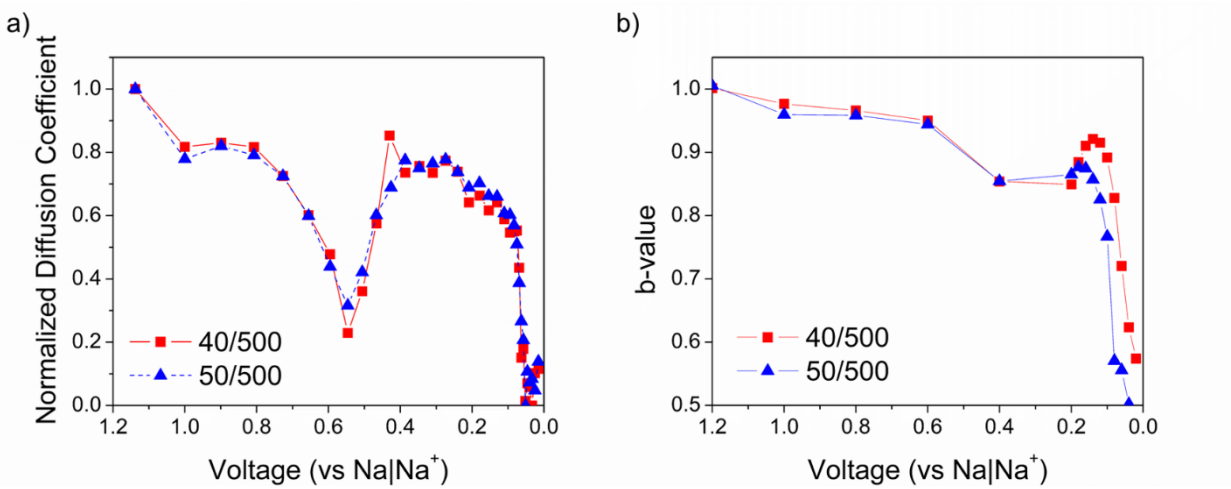

Figure B.5. a) Normalized diffusion coefficient derived from a GITT experiment and **b)** *b*-value analysis to differentiate regimes of differing charge-storage mechanism.

The galvanostatic intermittent titration technique (GITT), in which current pulses and subsequent rest periods are alternated to track the transient voltage response during rest, is used to measure the Na-ion diffusion coefficient at different potentials (Figure B.5a; sodiation curves are shown in Figure B.6). Two minima in diffusivity occur at ~0.55 V and ~0.1 V. The first minimum can be attributed to SEI formation, as previously observed in GITT curves for hard carbon[32,37,46]; the second can be attributed to the shift in storage mechanism from defect-mediated to insertion/micropore-mediated.[47] We also perform *b*-value analysis on voltammetric data (Figure B.2), from which we determine a more precise transition point between these charge-storage regimes (Figure B.5b). The b-value analysis characterizes the charge-storage process as either diffusion-controlled (b = 0.5, current proportional to the square root of sweep rate) or surface-controlled (b = 1, current varies linearly with sweep rate). The slope of log(sweep) rate against log(peak current) provides the b-value, and this analysis can be performed over the entire voltage range.[48] Both the 40/500 and 50/500 CNF electrodes exhibit surface-controlled charge storage from 2 V to 0.15 V, a trend that is verified when voltammetric

currents are normalized linearly for scan rate (Figure B.7). Below 0.15 V the rate of charge storage becomes diffusion-controlled, in agreement with the GITT analysis.

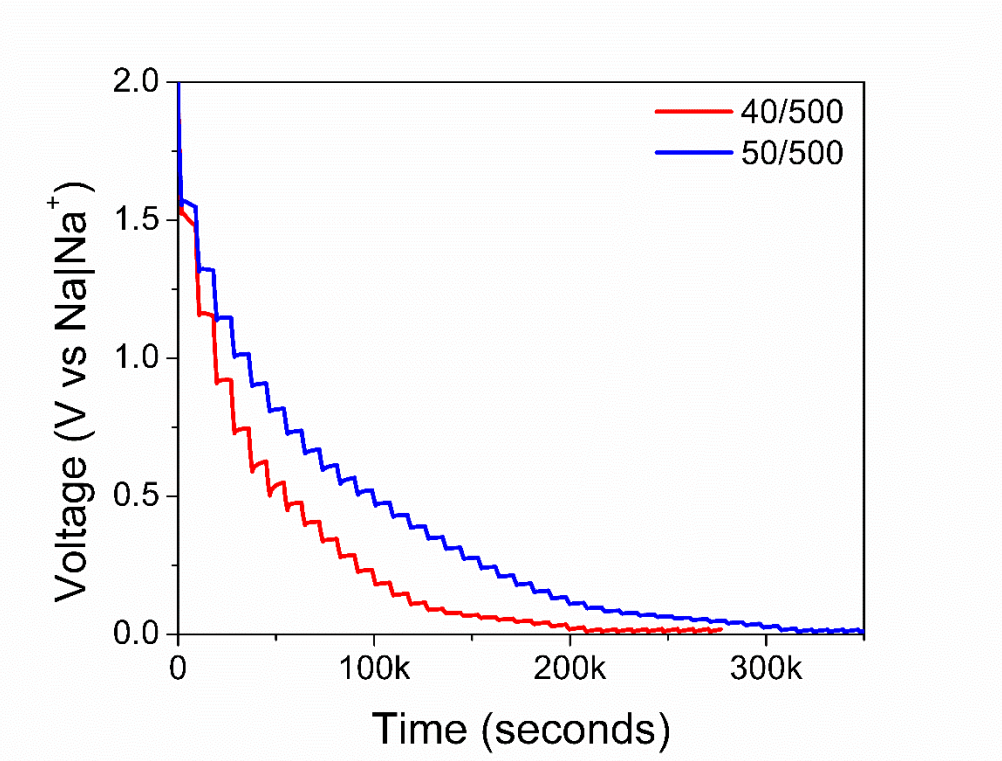

Figure B.6. Galvanostatic sodiation curves for galvanostatic intermittent titration (GITT) tested with a current pulse of 10 mA g_T^{-1} for 30 min followed by a relaxation period of 2 hours.

The following equation was used to calculate diffusivity[9]:

$$\widetilde{D} = \frac{4}{\pi}\left(\frac{m_b V_m}{M_B S}\right)\left(\frac{\Delta E_s}{\Delta E_t}\right)^2$$

Where:

m = mass of sample

V_m = molar volume

M_B = molar mass

S = contact surface area

E_s = the voltage difference between the plateau of each rest period

E_t = the voltage difference between the bottom of initial iR drop and the end voltage during the current pulse period

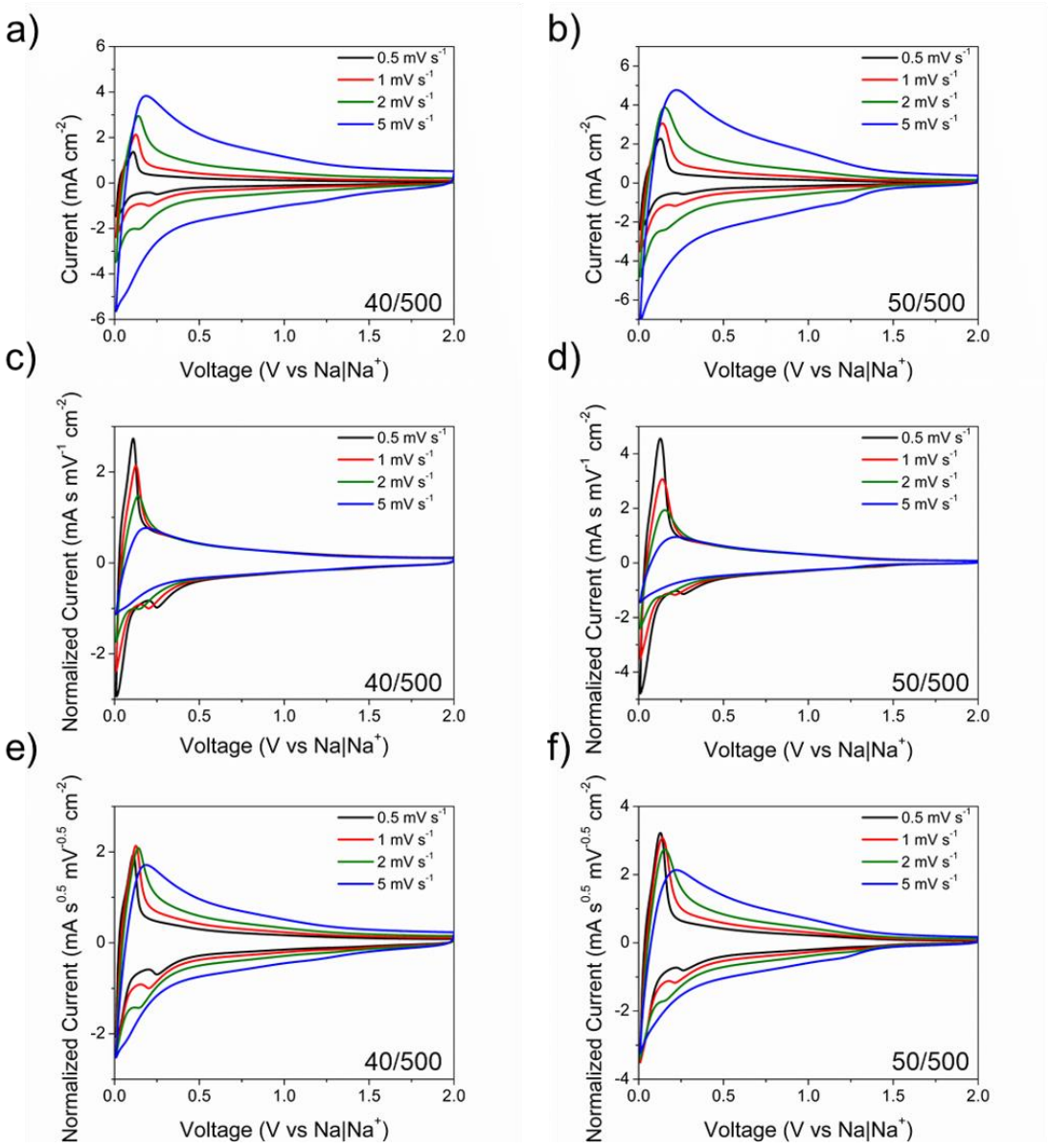

Figure B.7. Cyclic voltammograms of the 40/500 **(a,c,e)** and 50/500 **(b,d,f)** CNF electrodes with **a,b)** current normalized only to area **c,d)** current normalized to area and sweep rate and **e,f)** current normalized to area and the square root of sweep rate.

Using the cut-off voltage determined above (0.15 V), the capacity contributions from the sloping and plateau regions of the discharge can be calculated (Figure B.8). This treatment reveals that even at low current density, the majority of measured capacity (~ 66%) derives from the sloping region (2.0–0.15 V). As the current density increases, the contribution to capacity from the sloping region is essentially constant, consistent with the relatively high diffusion coefficient and *b*-value of 1, while the plateau region continually diminishes to < 10% of total capacity at 1 A g_T^{-1}. For hard carbons, storage within the sloping region is typically attributed to adsorption at defect sites (monovacancies, divacancies, Stone–Wales defects, etc.), whereas turbostratic-domain insertion and micropore clustering dominate in the plateau region.[8,9,49] The high capacity of and rate retention in the defect-mediated voltage range for CNF suggests that increasing the defect density of the carbon nanofoam could boost charge-storage performance even further. Raman scattering indicates a modestly higher I_D/I_G ratio for 50/500 (Figure B.9).

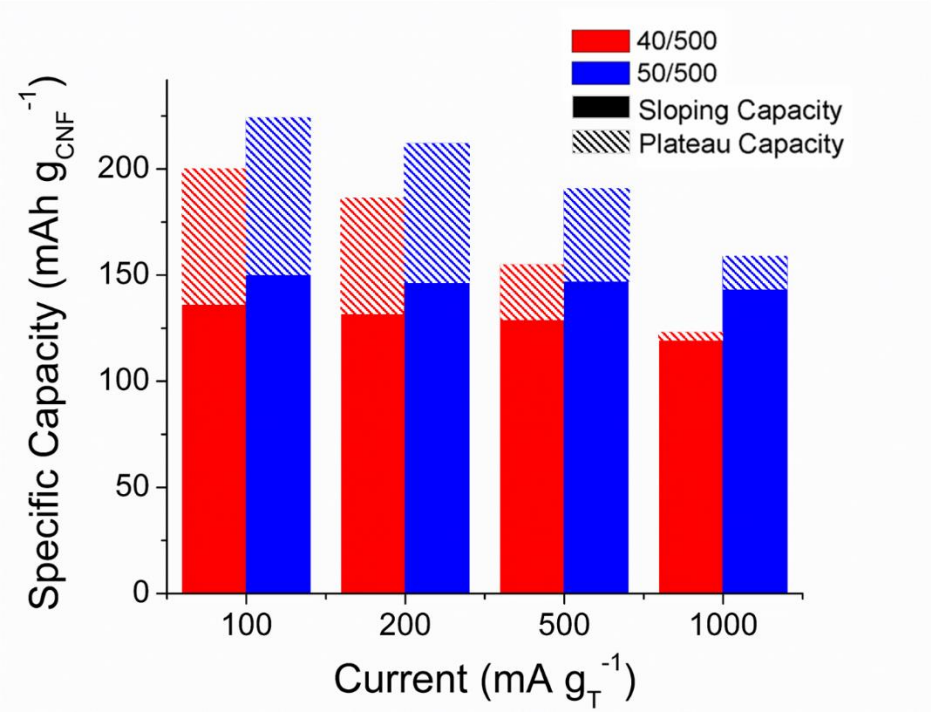

Figure B.8. Capacity distribution from the sloping region (solid) and from the plateau region (shaded) for both the 40/500 (red) and the 50/500 (blue) CNF paper electrodes.

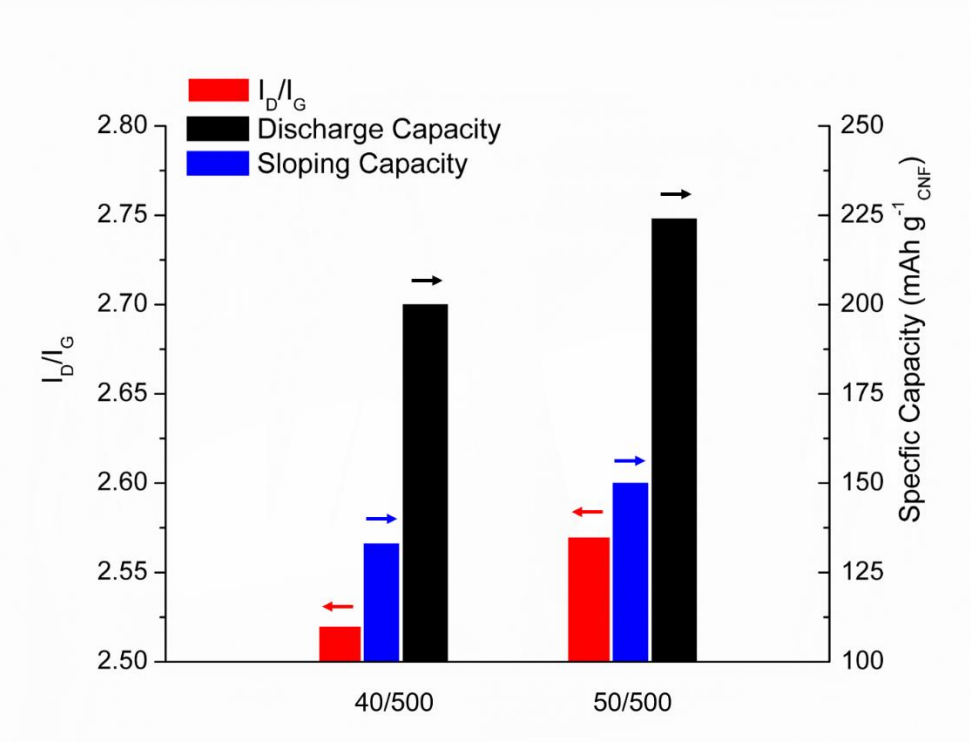

Figure B.9. Sloping and total discharge capacity from galvanostatic cycling at 50 mA g_T^{-1} as a compared to the relative intensity of the D- and G-bands from Raman spectroscopy.

B.3. Conclusions

Defect-mediated charge-storage mechanisms operate at higher potential (*vs.* Na|Na^+) than for Na^+ insertion/clustering reactions, yet the improved capacity and rate performance now demonstrated in a device-ready hard-carbon electrode architecture should more than compensate for the slight loss in voltage (~ 0.3 V) when used in full-cell NIBs. By fabricating electrodes in lightweight, freestanding forms, such as CNF papers, cell-level specific energy can be significantly increased by minimizing weight contributions from passive components (binder, conductive additive, current collector). Carbon nanofoam paper electrodes have also demonstrated near-linear scaling of capacity with the use of multiple layers of carbon-fiber paper[25], which indicates achievable, industrially relevant mass loading per geometric area.

While the electrochemical results presented herein are promising from a practical perspective, further understanding of the role of specific defects in carbon for Na-ion storage will support additional improvements in capacity, power, and cycle life. Because disordered/amorphous carbons are more difficult to characterize than their crystalline counterparts, advanced techniques will be particularly insightful, especially those that are performed *in-operando*, such as total neutron scattering and the associated pair distribution function analysis and soft X-ray–based characterization techniques.[9,50]

B.4. Material and Methods

All materials were used as received. Carbon nanofoam papers were prepared as previously reported.[23,25] Briefly, Lydall carbon paper is first treated in an air plasma (Harrick plasma cleaner; ice chips included in the chamber to also supply water vapor), a process that ensures effective wetting of the paper in subsequent steps. Resorcinol-formaldehyde (RF) precursor sols were prepared by mixing resorcinol, water, formaldehyde, and aqueous sodium carbonate solution for 30 minutes then left to oligimerize for 3 hours at room temperature. To achieve distinct architectures, the weight percent of RF in the aqueous sol was weight 40% (40/500 samples) or 50% (50/500 samples). Both 40/500 and 50/500 CNF architectures had a resorcinol:Na_2CO_3 molar ratio of 500:1. After oligimerization, plasma-treated papers were immersed into the sol and impregnated with the assistance of vacuum. Infiltrated carbon paper is then clipped to clean glass slides and the assembly is wrapped in duct tape to slow solvent evaporation. Duct-taped packages are then sealed into aluminum foil pouches with a small amount of DI water and subsequently heated in a pressure cooker ~90°C for 9.5 hours followed by 80°C for 14.5 hours. Following this polymerization step, the samples are pyrolyzed at 1000°C under flowing argon to yield the final CNF paper.

The electrolyte was 1 M $NaPF_6$ (Sigma Aldrich) in diethylene glycol dimethyl ether (Sigma Aldrich); Whatman glass fiber was used as the separator in all experiments. A voltage range of 2 V to 0.01 V vs. sodium metal (Sigma Aldrich) was used in all experiments. Half-cells were constructed in coin-cell format with polished sodium metal as the counter/reference electrode. Galvanostatic cycling was conducted using an Arbin BT2000 cycler and the capacity was normalized to the amount of carbon nanofoam (mA h g_{CNF}^{-1}) as the carbon fiber paper is not electrochemically active to a large degree (Figure B.4). The areal weight loading of the 50/500 and 40/500 carbon nanofoam papers are ~ 3.65 and ~2.82 mg cm^{-2} CNF, respectively. Current was normalized to the weight of the entire electrode (mA g_T^{-1}). Voltammetric experiments were conducted on a Gamry 600 potentiostat and GITT was performed on a Biologic VMP3 potentiostat. The GITT analysis was performed by first precycling the electrodes at 25 mA g_T^{-1} for 5 cycles and then applying a current of 10 mA g_T^{-1} for 30 min followed by a relaxation period of 2 h. For analysis by scanning electron microscopy, CNF papers were first immersed in liquid nitrogen for 1 minute, freeze-fractured with a new razor blade, then mounted on 45/90^o aluminum SEM stubs with conductive carbon paint. Imaging of the cross section was performed at 20 keV on a Leo Supra 55 SEM. X-ray photoelectron spectroscopy was performed on a Kratos Axis Ultra with a 203 monochromatic aluminum X-ray source.

B.5. References

1. Kundu, D.; Talaie, E.; Duffort, V.; Nazar, L. F. The Emerging Chemistry of Sodium Ion Batteries for Electrochemical Energy Storage. *Angew. Chem. Int. Ed.* **2015**, *54* (11), 3431–3448. https://doi.org/10.1002/anie.201410376.

2. Hwang, J.-Y.; Myung, S.-T.; Sun, Y.-K. Sodium-Ion Batteries: Present and Future. *Chem. Soc. Rev.* **2017**, *46* (12), 3529–3614. https://doi.org/10.1039/C6CS00776G.

3. Vaalma, C.; Buchholz, D.; Weil, M.; Passerini, S. A Cost and Resource Analysis of Sodium-Ion Batteries. *Nat. Rev. Mater.* **2018**, *3* (4), 18013. https://doi.org/10.1038/natrevmats.2018.13.

4. Balogun, M.-S.; Luo, Y.; Qiu, W.; Liu, P.; Tong, Y. A Review of Carbon Materials and Their Composites with Alloy Metals for Sodium Ion Battery Anodes. *Carbon* **2016**, *98*, 162–178. https://doi.org/10.1016/j.carbon.2015.09.091.

5. Moriwake, H.; Kuwabara, A.; Fisher, C. A. J.; Ikuhara, Y. Why Is Sodium-Intercalated Graphite Unstable? *RSC Adv.* **2017**, *7* (58), 36550–36554. https://doi.org/10.1039/C7RA06777A.

6. Stevens, D. A.; Dahn, J. R. High Capacity Anode Materials for Rechargeable Sodium-Ion Batteries. *J. Electrochem. Soc.* **2000**, *147* (4), 1271. https://doi.org/10.1149/1.1393348.

7. Stevens, D. A.; Dahn, J. R. The Mechanisms of Lithium and Sodium Insertion in Carbon Materials. *J. Electrochem. Soc.* **2001**, *148* (8), A803. https://doi.org/10.1149/1.1379565.

8. Anji Reddy, M.; Helen, M.; Groß, A.; Fichtner, M.; Euchner, H. Insight into Sodium Insertion and the Storage Mechanism in Hard Carbon. *ACS Energy Lett.* **2018**, 2851–2857. https://doi.org/10.1021/acsenergylett.8b01761.

9. Bommier, C.; Surta, T. W.; Dolgos, M.; Ji, X. New Mechanistic Insights on Na-Ion Storage in Nongraphitizable Carbon. *Nano Lett.* **2015**, *15* (9), 5888–5892. https://doi.org/10.1021/acs.nanolett.5b01969.

10. Datta, D.; Li, J.; Shenoy, V. B. Defective Graphene as a High-Capacity Anode Material for Na- and Ca-Ion Batteries. *ACS Appl. Mater. Interfaces* **2014**, *6* (3), 1788–1795. https://doi.org/10.1021/am404788e.

11. Legrain, F.; Sottmann, J.; Kotsis, K.; Gorantla, S.; Sartori, S.; Manzhos, S. Amorphous (Glassy) Carbon, a Promising Material for Sodium Ion Battery Anodes: A Combined First-Principles and Experimental Study. *J. Phys. Chem. C* **2015**, *119* (24), 13496–13501. https://doi.org/10.1021/acs.jpcc.5b03407.

12. Cao, B.; Liu, H.; Xu, B.; Lei, Y.; Chen, X.; Song, H. Mesoporous Soft Carbon as an Anode Material for Sodium Ion Batteries with Superior Rate and Cycling Performance. *J. Mater. Chem. A* **2016**, *4* (17), 6472–6478. https://doi.org/10.1039/C6TA00950F.

13. Yao, X.; Ke, Y.; Ren, W.; Wang, X.; Xiong, F.; Yang, W.; Qin, M.; Li, Q.; Mai, L. Defect-Rich Soft Carbon Porous Nanosheets for Fast and High-Capacity Sodium-Ion Storage. *Adv. Energy Mater.* **2018**, 1803260. https://doi.org/10.1002/aenm.201803260.

14. An, H.; Li, Y.; Gao, Y.; Cao, C.; Han, J.; Feng, Y.; Feng, W. Free-Standing Fluorine and Nitrogen Co-Doped Graphene Paper as a High-Performance Electrode for Flexible Sodium-Ion Batteries. *Carbon* **2017**, *116*, 338–346. https://doi.org/10.1016/j.carbon.2017.01.101.

15. Xu, J.; Wang, M.; Wickramaratne, N. P.; Jaroniec, M.; Dou, S.; Dai, L. High-Performance Sodium Ion Batteries Based on a 3D Anode from Nitrogen-Doped Graphene Foams. *Adv. Mater.* **2015**, *27* (12), 2042–2048. https://doi.org/10.1002/adma.201405370.

16. Wang, S.; Xia, L.; Yu, L.; Zhang, L.; Wang, H.; Lou, X. W. D. Free-Standing Nitrogen-Doped Carbon Nanofiber Films: Integrated Electrodes for Sodium-Ion Batteries with Ultralong Cycle Life and Superior Rate Capability. *Adv. Energy Mater.* **2016**, *6* (7), 1502217. https://doi.org/10.1002/aenm.201502217.

17. Cao, Y.; Xiao, L.; Sushko, M. L.; Wang, W.; Schwenzer, B.; Xiao, J.; Nie, Z.; Saraf, L. V.; Yang, Z.; Liu, J. Sodium Ion Insertion in Hollow Carbon Nanowires for Battery Applications. *Nano Lett.* **2012**, *12* (7), 3783–3787. https://doi.org/10.1021/nl3016957.

18. Tang, K.; Fu, L.; White, R. J.; Yu, L.; Titirici, M.-M.; Antonietti, M.; Maier, J. Hollow Carbon Nanospheres with Superior Rate Capability for Sodium-Based Batteries. *Adv. Energy Mater.* **2012**, *2* (7), 873–877. https://doi.org/10.1002/aenm.201100691.

19. Pol, V. G.; Lee, E.; Zhou, D.; Dogan, F.; Calderon-Moreno, J. M.; Johnson, C. S. Spherical Carbon as a New High-Rate Anode for Sodium-Ion Batteries. *Electrochimica Acta* **2014**, *127*, 61–67. https://doi.org/10.1016/j.electacta.2014.01.132.

20. Yang, B.; Chen, J.; Lei, S.; Guo, R.; Li, H.; Shi, S.; Yan, X. Spontaneous Growth of 3D Framework Carbon from Sodium Citrate for High Energy- and Power-Density and Long-Life Sodium-Ion Hybrid Capacitors. *Adv. Energy Mater.* **2018**, *8* (10), 1702409. https://doi.org/10.1002/aenm.201702409.

21. Chen, J.; Yang, B.; Hou, H.; Li, H.; Liu, L.; Zhang, L.; Yan, X. Disordered, Large Interlayer Spacing, and Oxygen-Rich Carbon Nanosheets for Potassium Ion Hybrid Capacitor. *Adv. Energy Mater.* **2019**, 1803894. https://doi.org/10.1002/aenm.201803894.

22. Wang, P.; Yang, B.; Zhang, G.; Zhang, L.; Jiao, H.; Chen, J.; Yan, X. Three-Dimensional Carbon Framework as a Promising Anode Material for High Performance Sodium Ion Storage Devices. *Chem. Eng. J*. **2018**, *353*, 453–459.

23. Lytle, J. C.; Wallace, J. M.; Sassin, M. B.; Barrow, A. J.; Long, J. W.; Dysart, J. L.; Renninger, C. H.; Saunders, M. P.; Brandell, N. L.; Rolison, D. R. The Right Kind of Interior for Multifunctional Electrode Architectures: Carbon Nanofoam Papers with Aperiodic Submicrometre Pore Networks Interconnected in 3D. *Energy Environ. Sci.* **2011**, *4* (5), 1913. https://doi.org/10.1039/c0ee00351d.

24. Sassin, M. B.; Chervin, C. N.; Rolison, D. R.; Long, J. W. Redox Deposition of Nanoscale Metal Oxides on Carbon for Next-Generation Electrochemical Capacitors. *Acc. Chem. Res.* **2013**, *46* (5), 1062–1074. https://doi.org/10.1021/ar2002717.

25. Sassin, M. B.; Hoag, C. P.; Willis, B. T.; Kucko, N. W.; Rolison, D. R.; Long, J. W. Designing High-Performance Electrochemical Energy-Storage Nanoarchitectures to Balance Rate and Capacity. *Nanoscale* **2013**, *5* (4), 1649. https://doi.org/10.1039/c2nr34044e.

26. Xiao, L.; Lu, H.; Fang, Y.; Sushko, M. L.; Cao, Y.; Ai, X.; Yang, H.; Liu, J. Low-Defect and Low-Porosity Hard Carbon with High Coulombic Efficiency and High Capacity for Practical Sodium Ion Battery Anode. *Adv. Energy Mater.* **2018**, *8* (20), 1703238. https://doi.org/10.1002/aenm.201703238.

27. Pekala, R. W.; Alviso, C. T.; Kong, F. M.; Hulsey, S. S. Aerogels Derived from Multifunctional Organic Monomers. *J. Non-Cryst. Solids* **1992**, *145*, 90–98. https://doi.org/10.1016/S0022-3093(05)80436-3.

28. Zhou, D.; Peer, M.; Yang, Z.; Pol, V. G.; Key, F. D.; Jorne, J.; Foley, H. C.; Johnson, C. S. Long Cycle Life Microporous Spherical Carbon Anodes for Sodium-Ion Batteries Derived from Furfuryl Alcohol. *J. Mater. Chem. A* **2016**, *4* (17), 6271–6275. https://doi.org/10.1039/C6TA00242K.

29. Song, J.; Xiao, B.; Lin, Y.; Xu, K.; Li, X. Interphases in Sodium-Ion Batteries. *Adv. Energy Mater.* **2018**, *8* (17), 1703082. https://doi.org/10.1002/aenm.201703082.

30. Seh, Z. W.; Sun, J.; Sun, Y.; Cui, Y. A Highly Reversible Room-Temperature Sodium Metal Anode. *ACS Cent. Sci.* **2015**, *1* (8), 449–455. https://doi.org/10.1021/acscentsci.5b00328.

31. He, Y.; Bai, P.; Gao, S.; Xu, Y. Marriage of an Ether-Based Electrolyte with Hard Carbon Anodes Creates Superior Sodium-Ion Batteries with High Mass Loading. *ACS Appl. Mater. Interfaces* **2018**, *10* (48), 41380–41388. https://doi.org/10.1021/acsami.8b15274.

32. Wang, P.; Zhu, X.; Wang, Q.; Xu, X.; Zhou, X.; Bao, J. Kelp-Derived Hard Carbons as Advanced Anode Materials for Sodium-Ion Batteries. *J. Mater. Chem. A* **2017**, *5* (12), 5761–5769. https://doi.org/10.1039/C7TA00639J.

33. Li, Z.; Jian, Z.; Wang, X.; Rodríguez-Pérez, I. A.; Bommier, C.; Ji, X. Hard Carbon Anodes of Sodium-Ion Batteries: Undervalued Rate Capability. *Chem. Commun.* **2017**, *53* (17), 2610–2613. https://doi.org/10.1039/C7CC00301C.

34. Zheng, Y.; Wang, Y.; Lu, Y.; Hu, Y.-S.; Li, J. A High-Performance Sodium-Ion Battery Enhanced by Macadamia Shell Derived Hard Carbon Anode. *Nano Energy* **2017**, *39*, 489–498. https://doi.org/10.1016/j.nanoen.2017.07.018.

35. Saurel, D.; Orayech, B.; Xiao, B.; Carriazo, D.; Li, X.; Rojo, T. From Charge Storage Mechanism to Performance: A Roadmap toward High Specific Energy Sodium-Ion Batteries through Carbon Anode Optimization. *Adv. Energy Mater.* **2018**, *8* (17), 1703268. https://doi.org/10.1002/aenm.201703268.

36. Irisarri, E.; Ponrouch, A.; Palacin, M. R. Review—Hard Carbon Negative Electrode Materials for Sodium-Ion Batteries. *J. Electrochem. Soc.* **2015**, *162* (14), A2476–A2482. https://doi.org/10.1149/2.0091514jes.

37. Zhu, Y.-E.; Yang, L.; Zhou, X.; Li, F.; Wei, J.; Zhou, Z. Boosting the Rate Capability of Hard Carbon with an Ether-Based Electrolyte for Sodium Ion Batteries. *J. Mater. Chem. A* **2017**, *5* (20), 9528–9532. https://doi.org/10.1039/C7TA02515G.

38. Bommier, C.; Ji, X. Electrolytes, SEI Formation, and Binders: A Review of Nonelectrode Factors for Sodium-Ion Battery Anodes. *Small* **2018**, *14* (16), 1703576. https://doi.org/10.1002/smll.201703576.

39. Bommier, C.; Mitlin, D.; Ji, X. Internal Structure – Na Storage Mechanisms – Electrochemical Performance Relations in Carbons. *Prog. Mater. Sci.* **2018**, *97*, 170–203. https://doi.org/10.1016/j.pmatsci.2018.04.006.

40. Nelson, P. A.; Gallagher, K. G.; Bloom, I.; Dees, D. W. Modeling the Performance and Cost of Lithium-Ion Batteries for Electric-Drive Vehicles. *Argonne Natl. Lab.*

41. Cheng, Q.; Zhang, Y. Multi-Channel Graphite for High-Rate Lithium Ion Battery. *J. Electrochem. Soc.* **2018**, *165* (5), A1104–A1109. https://doi.org/10.1149/2.1171805jes.

42. Wang, H.; Shi, Z.; Jin, J.; Chong, C.; Wang, C. Properties and Sodium Insertion Behavior of Phenolic Resin-Based Hard Carbon Microspheres Obtained by a Hydrothermal Method. *J. Electroanal. Chem.* **2015**, *755*, 87–91. https://doi.org/10.1016/j.jelechem.2015.07.032.

43. Li, Y.; Mu, L.; Hu, Y.-S.; Li, H.; Chen, L.; Huang, X. Pitch-Derived Amorphous Carbon as High Performance Anode for Sodium-Ion Batteries. *Energy Storage Mater.* **2016**, *2*, 139–145. https://doi.org/10.1016/j.ensm.2015.10.003.

44. Zhang, H.; Ming, H.; Zhang, W.; Cao, G.; Yang, Y. Coupled Carbonization Strategy toward Advanced Hard Carbon for High-Energy Sodium-Ion Battery. *ACS Appl. Mater. Interfaces* **2017**, *9* (28), 23766–23774. https://doi.org/10.1021/acsami.7b05687.

45. Hasegawa, G.; Kanamori, K.; Kannari, N.; Ozaki, J.; Nakanishi, K.; Abe, T. Hard Carbon Anodes for Na-Ion Batteries: Toward a Practical Use. *ChemElectroChem* **2015**, *2* (12), 1917–1920. https://doi.org/10.1002/celc.201500412.

46. Zhang, Y.; Li, X.; Dong, P.; Wu, G.; Xiao, J.; Zeng, X.; Zhang, Y.; Sun, X. Honeycomb-like Hard Carbon Derived from Pine Pollen as High-Performance Anode Material for Sodium-Ion Batteries. *ACS Appl. Mater. Interfaces* **2018**, *10* (49), 42796–42803. https://doi.org/10.1021/acsami.8b13160.

47. Wahid, M.; Puthusseri, D.; Gawli, Y.; Sharma, N.; Ogale, S. Hard Carbons for Sodium-Ion Battery Anodes: Synthetic Strategies, Material Properties, and Storage Mechanisms. *ChemSusChem* **2018**, *11* (3), 506–526. https://doi.org/10.1002/cssc.201701664.

48. Lindström, H.; Södergren, S.; Solbrand, A.; Rensmo, H.; Hjelm, J.; Hagfeldt, A.; Lindquist, S.-E. Li^+ Ion Insertion in TiO_2 (Anatase). 2. Voltammetry on Nanoporous Films. *J. Phys. Chem. B* **1997**, *101* (39), 7717–7722. https://doi.org/10.1021/jp970490q.

49. Qiu, S.; Xiao, L.; Sushko, M. L.; Han, K. S.; Shao, Y.; Yan, M.; Liang, X.; Mai, L.; Feng, J.; Cao, Y.; et al. Manipulating Adsorption-Insertion Mechanisms in Nanostructured Carbon Materials for High-Efficiency Sodium Ion Storage. *Adv. Energy Mater.* **2017**, *7* (17), 1700403. https://doi.org/10.1002/aenm.201700403.

50. Wei, Z.; Wang, D.; Yang, X.; Wang, C.; Chen, G.; Du, F. From Crystalline to Amorphous: An Effective Avenue to Engineer High-Performance Electrode Materials for Sodium-Ion Batteries. *Adv. Mater. Interfaces* **2018**, 1800639. https://doi.org/10.1002/admi.201800639.